Australian Government
Geoscience Australia

CSIRO

Circulation modelling in Torres Strait

Frederic Saint-Cast and Scott Condie

Record
2006/18

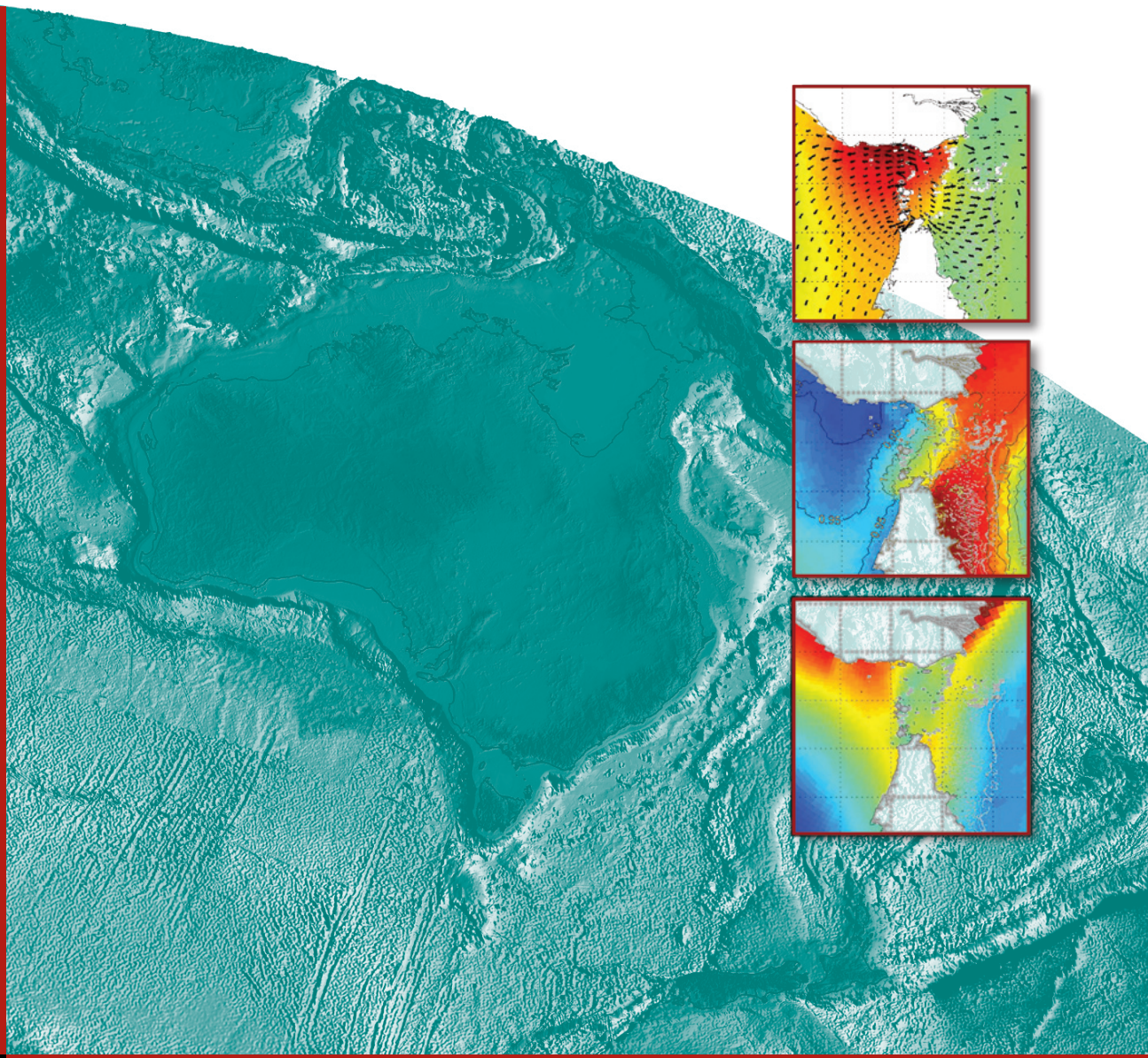

Geoscience Australia Record 2006/18

Circulation modelling in Torres Strait

Frederic Saint-Cast[1] & Scott Condie[2]

[1.] *Geoscience Australia – Petroleum and Marine Division, GPO Box 378, Canberra, ACT 2601*
[2.] *CSIRO - Marine and Atmospheric Research, GPO Box 1538, Hobart, TAS 7001*

Department of Industry, Tourism & Resources

Minister for Industry, Tourism & Resources: Senator The Hon. Ian Macfarlane, MP
Parliamentary Secretary: The Hon. Bob Baldwin, MP
Secretary: Mark Paterson

Geoscience Australia

Chief Executive Officer: Dr Neil Williams

ISSN: 1448-2177
ISBN: 1 920871 97 7

GeoCat No. 64807

Bibliographic reference: Saint-Cast, F. and Condie, S. (2006). *Circulation modelling in Torres Strait*. Geoscience Australia, Record 2006/18, 82pp.

Correspondence for feedback:
Sales Centre
Geoscience Australia
GPO Box 378
Canberra
ACT 2601

Sales@ga.gov.au

Contents

List of Figures

List of Tables

Executive summary

Increasing the knowledge of ocean current patterns in Torres Strait region is of direct interest to indigenous communities and industries such as fisheries and shipping that operate in the region. Ocean circulation in Torres Strait influences nearly all aspects of the ecosystem, including sediment transport and turbidity patterns, primary production in the water column and bottom sediments, and recruitment patterns for organisms with pelagic phases in their life cycles.

This study is the first attempt to describe the water circulation and transport patterns across Torres Strait and adjacent gulfs and seas, on time scales from hours to years. It has also provided a framework for an embedded model describing sediment transport processes (described in Margvelashvili and Saint-Cast, 2006).

The circulation model incorporated realistic atmospheric and oceanographic forcing, including winds, waves, tides, and large-scale regional circulation taken from global model outputs. Simulations covered a hindcast period of eight years, allowing the tidal, seasonal, and interannual flow characteristics to be investigated. Results demonstrated that instantaneous current patterns were strongly dominated by the barotropic tide and its spring-neap cycle. However, longer-term transport through Torres Strait was mainly controlled by seasonal winds, which switch from north-westerly monsoon winds in summer to south-easterly trades in winter.

Model results were shown to be relatively insensitive to internal model parameters. However, model performance was strongly dependent on the quality of the forcing fields. For example, the prediction of low-frequency inner-shelf currents was improved substantially when temperature and salinity forcing based on the average seasonal climatologies was replaced by that from global model outputs. Uncertainties in the tidal component of the forcing also limited model skill, particularly predictions to the west of Cape York which were strongly dependent on the sealevels imposed along the open boundary in Gulf of Carpentaria.

1 Introduction

The Torres Strait research program was directed at three key areas in response to stakeholder and end-user priorities: Harvested Marine Resources, Biophysical Processes, and Marine Systems Management Evaluations and Risks. A major component of the study was to identify and quantify the key biophysical processes operating in the Torres Strait marine ecosystem through targeted observations and the development of integrated modelling. This report describes the spatial and temporal characteristics of the Torres Strait circulation based on results from a hydrodynamic model of the region. The data and observations gained through the marine surveys analysis are described in an accompanying report, while a third report considers the influence of the circulation on sediment transport in the Torres Strait region.

Ocean circulation influences nearly all aspects of the ecosystem, including sediment transport and turbidity patterns, primary production in the water column and bottom sediments, and recruitment patterns for organisms with pelagic phases in their life cycles. One aspect of the ecosystem that is of particular concern is the distribution and health of seagrasses, with recent dieback events in northern Torres Strait potentially impacting species such as dugongs and juvenile rock lobster. Current patterns are therefore of considerable interest to Torres Strait indigenous communities who rely on natural resources for commercial and traditional purpose, as well as to industries such as fisheries and shipping that operate in the region.

This component of the study had three main objectives. First, to describe the oceanic circulation in the Torres Strait region on time scales from hours to years (this report). Second, to provide a transport framework for an embedded sediment transport model (described by Margvelashvili and Saint-Cast 2006). Third, to provide information on processes and relevant model outputs to other tasks and projects in the Torres Strait research program. Chapter 2 provides a brief review of previous studies related to circulation in Torres Strait. In Chapter 3, the hydrodynamic model is described, including its assumptions, inputs and outputs. Chapter 4 focuses on sensitivity of the circulation to model parameters and validation against available field data. Chapter 5 provides examples of current fields and summarises the results in the form of seasonal and interannual anomaly fields. Conclusions of the study are presented in Chapter 6. In addition, a statement addressing each of the Torres strait CRC objectives for this task provided in Appendix 9.1. More details on the external forcing fields (winds, waves and sealevel) are also provided in appendices.

2 Background

Torres Strait is the shallow body of water connecting the Gulf of Carpentaria to the continental shelf of the Great Barrier Reef. Flow through the strait controls the exchange of water between the Arafura Sea and Coral Sea (Figure 1) and is the only alternative pathway to the Indonesian Throughflow for exchange of tropical waters between the Pacific and Indian Oceans.

The Torres Strait is situated in a wet tropical region with mean daily maximum summertime temperatures around 31°C and mean daily minimum wintertime temperatures around 22.5°C. The mean annual rainfall is 1746 mm, most of which falls between December and April (Bureau of Meteorology weather statistics at Thursday Island). With rainfall in the highlands of Papua New Guinea (PNG) of 10 – 13 m annually, the terrestrial runoff into the marine environment is around 15000 $m^3 s^{-1}$ and shows little evidence of seasonal fluctuations (Wolanski et al., 1995). The Fly River emptying into the Gulf of Papua accounts for about half the PNG discharge (7500 $m^3 s^{-1}$) and is characterised by water temperatures around 26°C and salinities around 12 PSU (Alongi et al., 1992).

During summer (December to March), prevailing monsoon winds are typically around 20 km hr^{-1} from the northwest. Over winter (April to November) these swing around to dry southeasterly trades of around 30 km hr^{-1}. Wind wave heights rarely exceed 3.5m and are nearly always less than 1.5m during the monsoon. High energy swells generated in the Coral Sea are blocked by the northern most extension of the Great Barrier Reef. Tropical cyclones are rare in Torres Strait, but in the Gulf of Carpentaria can generate maximum wave heights up to 9m.

Circulation in Torres Strait is influenced by the broader scale circulation in the Gulf of Carpentaria to the west (Wolanski, 1993; Condie et al., 1999, 2002) and the Coral Sea to the east where the Hiri Current follows the shelf-break (Qu and Lindstrom, 2002). Low-frequency currents through the strait are relatively weak at around 0.1 m s^{-1} and reverse direction following the dominant winds (Wolanski et al., 1988). The net flow is westward and has been estimated to be around 1% of the Indonesian Throughflow (Meyers et al., 1995; Wijffels and Meyers, 2004).

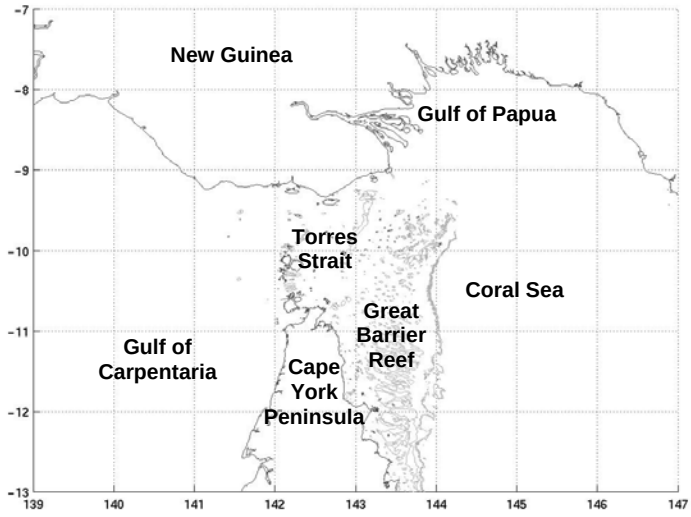

Figure 1: Map of the Torres Strait region.

The impact of El Nino on the Torres Strait circulation includes lower rainfall and river discharge, weaker than normal easterly (trade) winds, and generally fewer cyclones (Bureau of Meteorology). While the western boundary current strengthens along the Papua New Guinea coastline facing the Solomon Sea, a significant modification of the Hiri Current strength seems unlikely since no significant response to the ENSO has been observed in the Coral Sea (Ridgeway et al. 1993).

Daily current patterns in Torres Strait are dominated by strong tidal motions, with a tidal range of up to 6 m (Wolanski et al., 1988). Tidal currents are predominantly in the through-strait direction, except around Reefs and Islands and through the passages in the Strait where island wakes and tidal jets are present (Wolanski et al, 1984a,b). For instance, semidiurnal flow speeds can reach up to 2 m s^{-1} in the Prince of Wales Channel (Clarke, 1989). These strong tidal currents result from the intersection of two separate and dissimilar tidal regimes in the Gulf of Carpentaria and the Coral Sea (Bode and Mason, 1994). Only 30% of the semidiurnal tidal wave is transmitted through Torres Strait, underlining strong energy dissipation by bottom friction and internal mixing.

A number of hydrodynamic models have previously been developed for the Torres Strait region. These range from analytical solutions of one-dimensional wave-guide models (Wolanski et al., 1988); to numerical solutions of two-dimensional, depth-integrated, non-linear equations of momentum and mass conservation (Bode and Mason, 1994); and full three-dimensional numerical solutions of mass, momentum, salinity and temperature equations forced by average seasonal atmospheric and oceanographic conditions (Hemer et al., 2004). While the last of these studies was a significant step towards more realistic simulations, Hemer et al. (2004) acknowledged significant limitations associated with the use of average seasonal forcing and coarse spatial resolution relative to the geographic complexity of the region.

3 Circulation Model description

The model used to compute the circulation in Torres Strait was developed within CSIRO Atmospheric and Marine Research and in its current form is referred to as SHOC (Sparse Hydrodynamic Ocean Code). It is a general-purpose finite difference hydrodynamic model applicable to scales ranging from estuaries to ocean basins. It has found previous applications in systems such as the Derwent and Huon Estuaries in Tasmania, Gippsland Lakes, Port Phillip Bay (Walker, 1999), Bass Strait, the Great Australian Bight and Southeastern Australia (Bruce et al., 2001), the North West Shelf (Condie et al., 1999), and the Gulf of Carpentaria (Condie et al., 1999). The model has also been previously implemented in Torres Strait (Hemer et al., 2004), albeit at coarser scale resolution and with less realistic forcing than has been used in the current model.

Inputs required by the model included forcing due to wind, atmospheric pressure gradients and open boundary conditions such as temperature, salinity and sealevel. Wave forcing can also specified to represent the effects of wave-enhanced bottom friction in shallow water (Grant and Madsen, 1979). Surface heat and freshwater water fluxes can also be applied if reliable estimates are available, although this was not the case in Torres Strait. Standard outputs from SHOC include three-dimensional distributions of velocity, temperature, salinity, density, and mixing coefficients, as well as two-dimensional fields such as sea level and bottom friction.

A comprehensive description of the theory underlying the model is provided in the SHOC Scientific Manual (Herzfeld et al. 2004), and therefore only a very brief technical description will be provided here. SHOC is based on the three dimensional equations of momentum, continuity and conservation of heat and salt, employing the hydrostatic and Boussinesq assumptions. The equations of motion are discretised on a finite difference stencil corresponding to the Arakawa C grid. The model uses a curvilinear orthogonal grid in the horizontal and fixed z-coordinates (horizontal layers) in the vertical. While the model also supports sigma coordinates (bathymetry following) in the vertical, they can not be applied to systems that include both shallow coastal waters (4 m in Torres Strait) and deep ocean waters (3400 m in the Coral Sea) and adequately resolve the vertical structure in the latter.

The model allows for wetting and drying of surface cells, and so is capable of handling sealevel changes associated with large tidal ranges. The model has a free surface and uses mode splitting to separate the two-dimensional mode from the three-dimensional mode. This allows fast moving gravity waves to be solved on a short time-step and slower moving internal waves on a longer time-step, thereby greatly enhancing the computational efficiency. Explicit time-stepping is used throughout except for the vertical diffusion scheme which is implicit so as to guarantee unconditional stability in regions of high vertical resolution.

3.1 Model implementation for Torres Strait

For the application of SHOC to the Torres Strait region, a second-order centred scheme (100 s time-step) was adopted for advection of momentum so as to minimise numerical diffusion. Advection of tracers, such as temperature and salinity, was calculated using the Van Leer (1979) higher-order upwind scheme. Laplacian diffusion was employed in the horizontal

(geopotential surfaces) using Smagorinsky (1963) mixing coefficients that effectively minimise diffusion while maintaining model stability through their dependence on grid size. The Mellor-Yamada level 2.0 scheme was mostly used to parameterise vertical diffusion. Bottom friction was represented by a quadratic law with a calibrated bottom roughness of 0.005 m and a minimum drag coefficient of 0.0005.

After testing a variety of grids, the model was finally implemented on a curvilinear grid designed to maximise the horizontal resolution within the strait, while ensuring that open boundaries in the Gulf of Carpentaria and Coral Sea were far removed from the strait (Figure 2). The domain extended west into the central Gulf of Carpentaria and east into the Gulf of Papua and beyond the shelf-break and into the Coral Sea. The domain boundaries intersected the Australian coastline on both sides of Cape York Peninsula around the latitude of the Archer River (13.3°S) and the New Guinea coastline at Port Moresby and west of Merauke. This grid provided a resolution of approximately 4 km in Torres Strait, expanding up to 20 km along the open boundaries. The vertical resolution followed a logarithmic distribution, with z-layer height expanding from 1 m near the surface to a maximum of 900 m at its maximum depth of 3400 m.

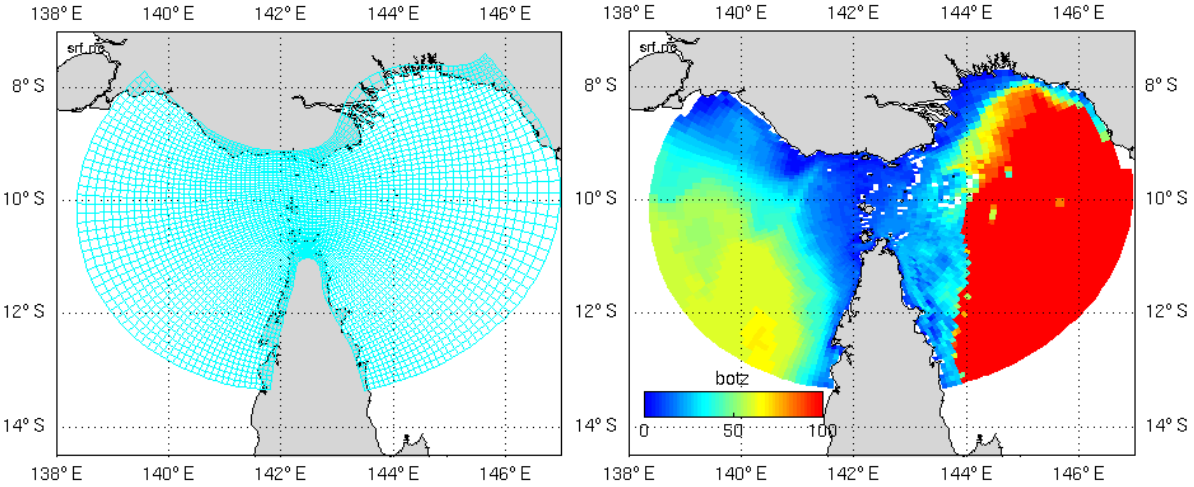

Figure 2: Torres Strait model grid (left) and model bathymetry in metres (right). The bathymetry was derived by averaging the Geosciences Australia product (Daniell, 2005) within each grid cell.

The bathymetry was prescribed by spatially averaging a 15 second (0.4 km) product provided by Geosciences Australia (Daniell, 2005) onto the model grid (Figure 2). The minimum water depth was set at 4 m to minimise the wetting and drying of coastal cells, which is a particularly computationally intensive operation. This represented a significant improvement on the minimum depth of 7m used by Hemer et al. (2004). Coastlines related to significant land masses were specified as solid boundaries with zero cross-flow. Large reef platforms exposed at low tide were also considered as major flow obstacles and therefore treated as solid boundaries. These included Awamaza Reef, Warrior Reefs, Dungeness Reef, Gariar Reef, Kai Reef, Beka Reef, Long Reef, Kagar Reef, Johnson Islet and a number of other smaller reefs.

Two wind products were used to specify the surface stress forcing in the model. For periods prior to September 2002, wind stress fields were taken from the ECMWF ERA-40 re-analysis. These were 6 hourly and had a horizontal resolution of 2.5 degrees. From September 2002, ECMWF forecast wind stresses were used. These were also 6 hourly but had a horizontal resolution of 0.5 degrees (Kallberg et al., 2004). In both cases, fields were linearly interpolated onto the model time-step and model grid (Figure 3 and Figure 4). The interpolated product generally showed good agreement with locally measured winds at sub-diurnal frequencies (Figure 5) although smaller scale processes such as daily sea-breezes were less well resolved (Figure 6). While tropical cyclone events would also be under-resolved (particularly prior to September 2002), their impact in the Torres Strait is infrequent compared to neighbouring areas (Figure 7).

Temperature and salinity fields along the open boundaries of the Torres Strait model were interpolated from a global circulation model known as the Ocean Forecast Australia Model (OFAM, Schiller et al. 2005). Average seasonal temperature and salinity from the CSIRO Atlas of Regional Seas (CARS; Ridgeway et al. 2002) were also trialled, but found to introduce significant errors and numerical instabilities in the Torres Strait model. Neumann conditions (i.e. nil normal gradients) were also implemented along the open boundaries for temperature, salinity and other tracers.

In the absence of reliable surface fluxes, interior temperatures and salinities were modified by relaxing them towards OFAM values with a 10 day relaxation timescale. The relaxation timescale had a significant impact on shelf temperatures and salinities. In particular, shorter relaxation times tended to smear gradients developing through advection of heat or salt. A 10 day relaxation time was chosen to constrain the temperature and salinity fields close to the OFAM fields, while allowing a flexible model response over shorter timescales.

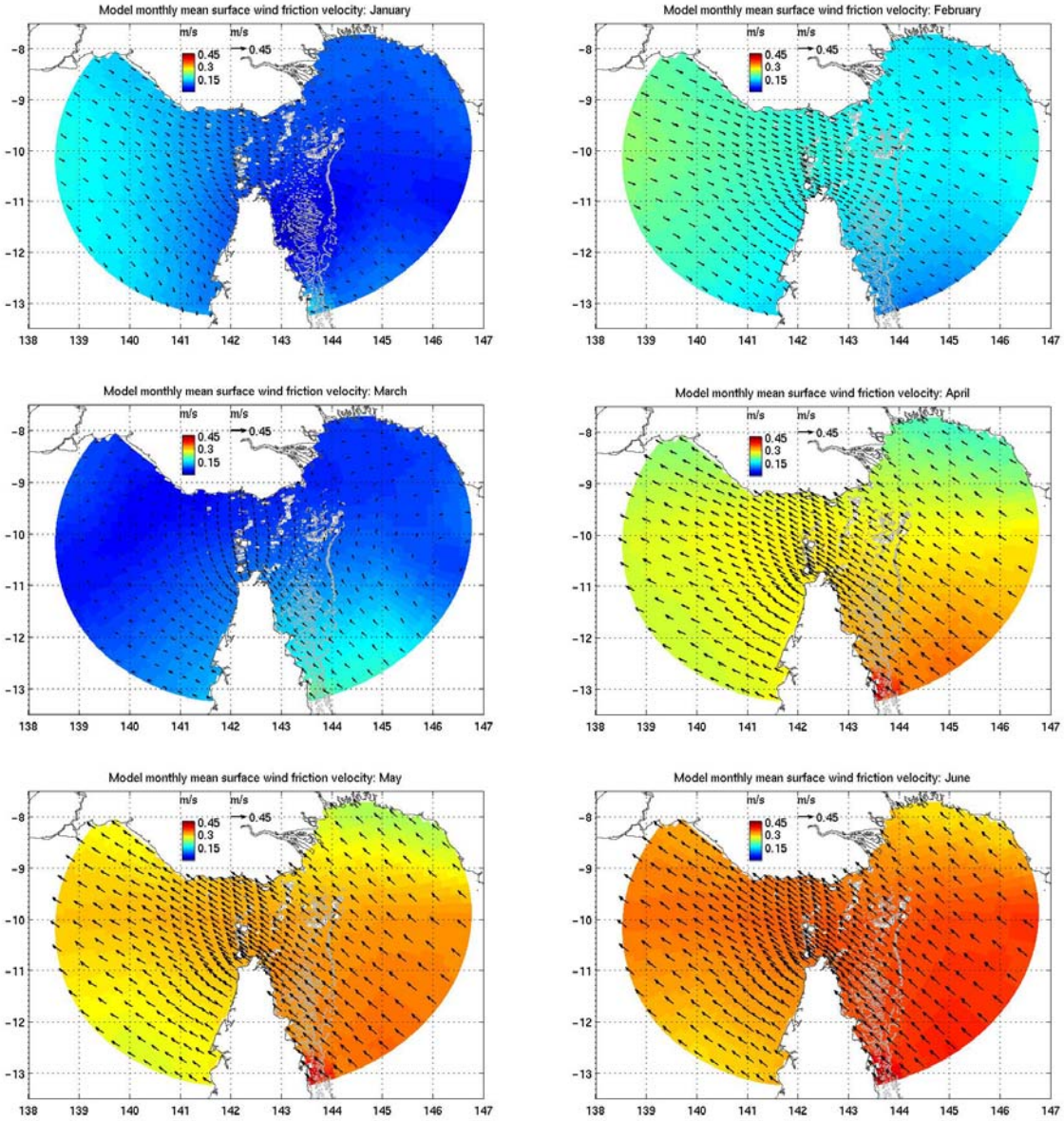

Figure 3: Monthly mean surface wind friction velocity (January to June). These fields were calculated by vector averaging the 6 hourly outputs of the ECMWF dataset across the years 1997 to 2005. They show the prevailing cycle of southeasterly trade winds over winter, switching to northwesterlies over summer as the trades are displaced to the south by equatorial westerlies. Surface wind stress is given by the product of air density (1.2 kg m^{-3}) and the square of surface wind friction velocity.

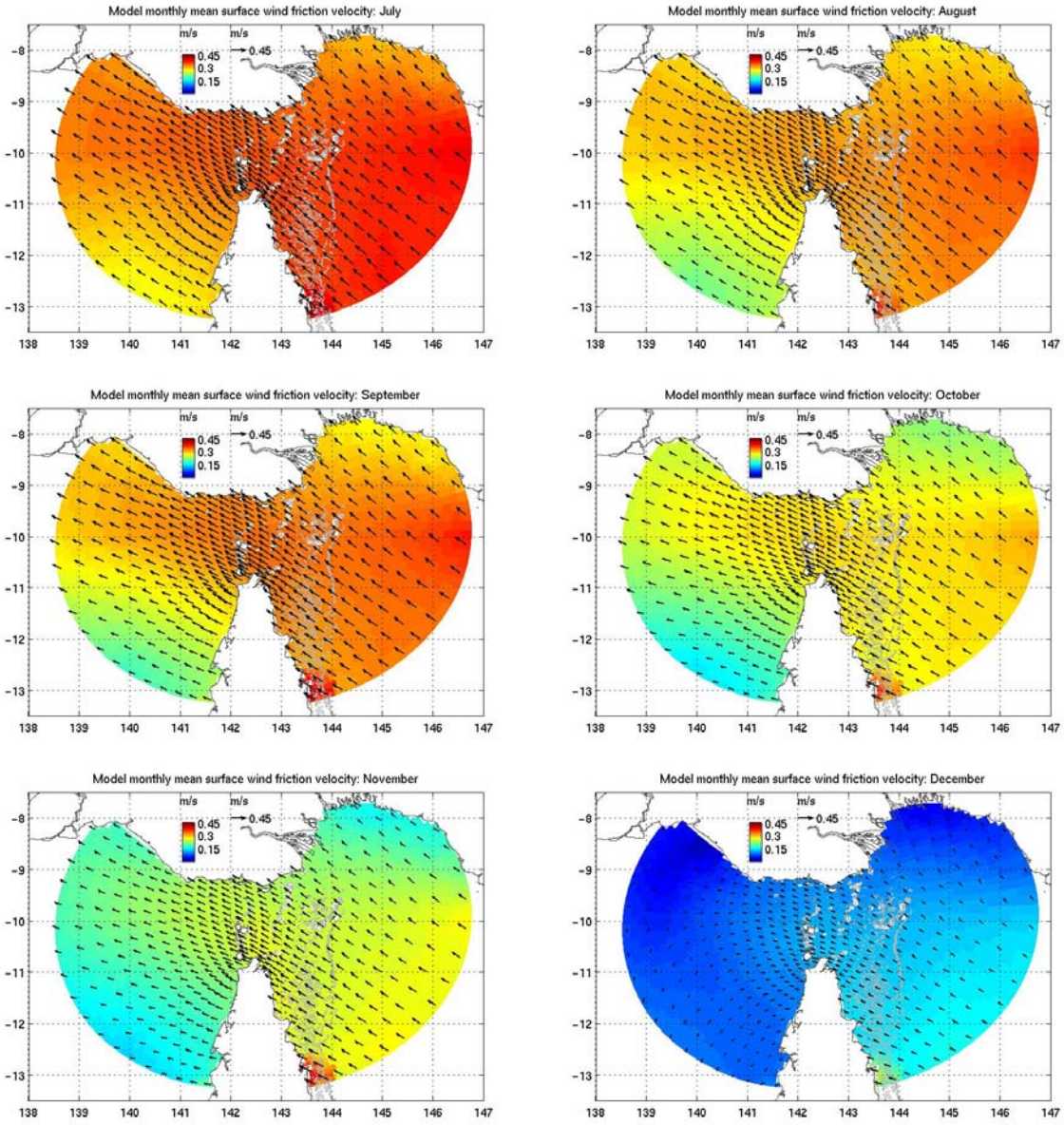

Figure 4: Monthly mean surface wind friction velocity. (July to December). These fields were calculated by vector averaging the 6 hourly outputs of the ECMWF dataset across the years 1997 to 2005. They show the prevailing cycle of southeasterly trade winds over winter, switching to northwesterlies over summer as the trades are displaced to the south by equatorial westerlies. Surface wind stress is given by the product of air density (1.2 kg m^{-3}) and the square of surface wind friction velocity.

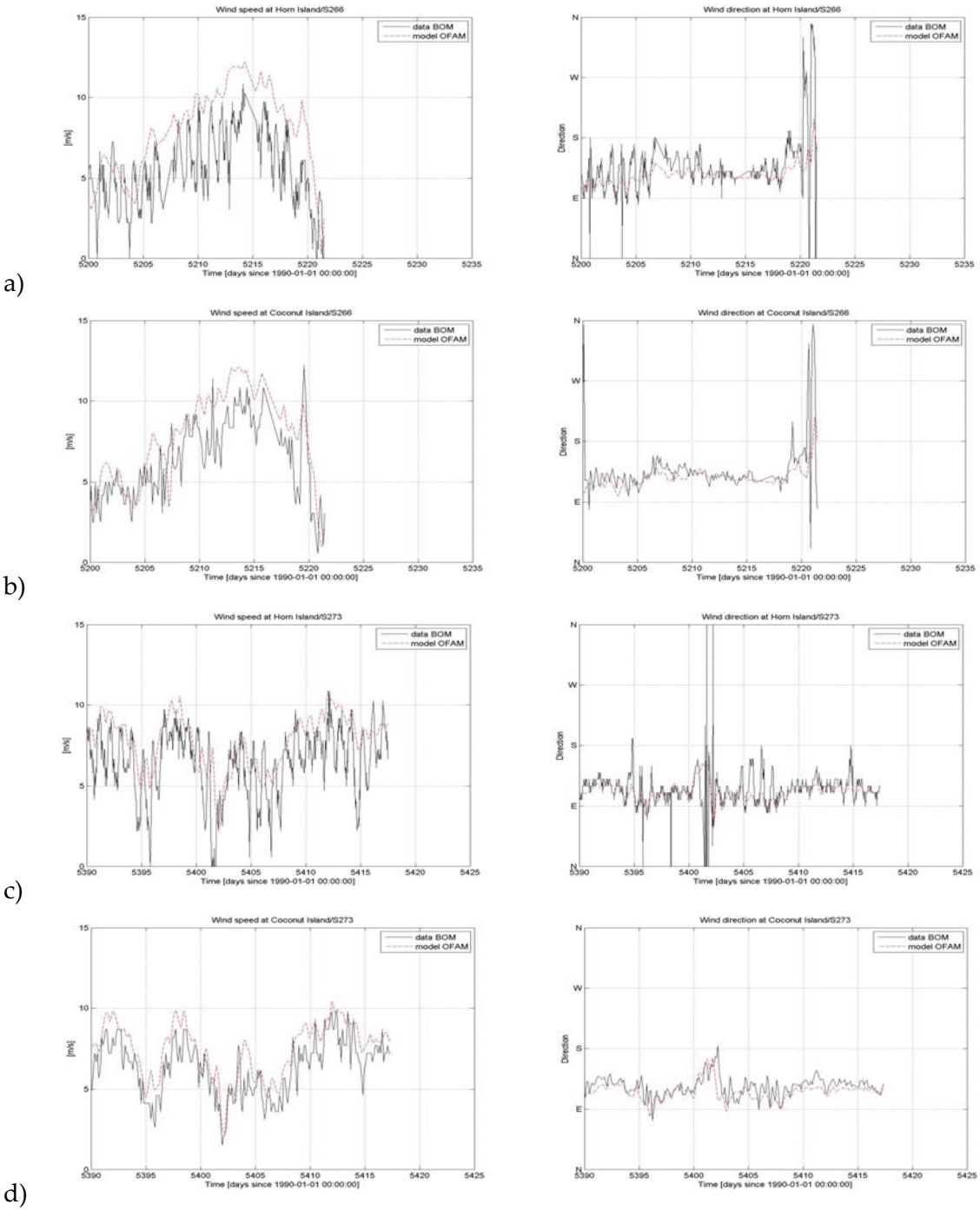

Figure 5: Time-series of wind speed (left) and direction (right) comparing the interpolated OFAM winds (from ECMWF) and locally observed winds (Bureau of Meteorology) for surveys S266 (a, b) and S273 (c, d) at Horn Island [10.48S; 142.29E] and Coconut Island [10.05S; 143.07E]. Modelled winds are in good agreement with maximum daily winds speed. Sub diurnal frequencies including sea breezes are not captured by the global wind model. The main wind cardinal direction is respected.

	December - February	March - April	June - August	September - November
9:00 am				
3:00 pm	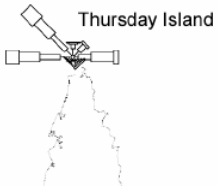		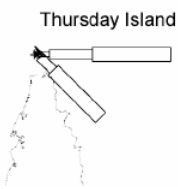	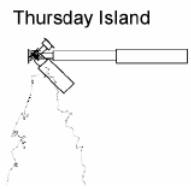
	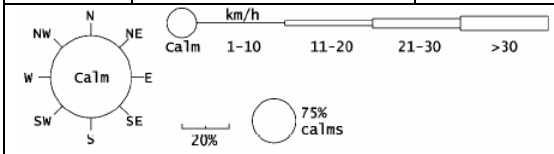			

Figure 6: Wind roses at Thursday Island prepared using data collected over the period 1961 to 1990. Site has a minimum of 75% of possible observations in this period. The wind rose has been compiled using data measured at a height of more than 3m above ground level and typically 10m above sea level (Bureau of Meteorology, 1999). Sea-breezes are responsible for minor shifts in wind direction and increasing occurrence of strong wind (>30km/h).

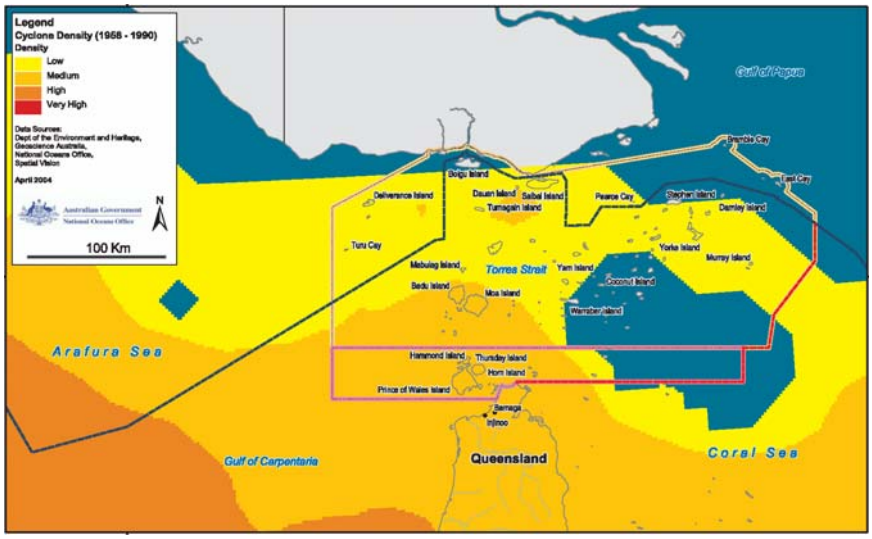

Figure 7: Cyclone density in the Torres Strait, after National Ocean Office.

Subtidal frequency sealevels on the open boundaries were also taken from OFAM output, with the addition of a tidal component calculated from tidal constituents derived from CRS4.0 Global Tide model (Eanes and Bettadpur, 1999). An alternative strategy using temperature, salinity, and sealevel outputs from a high resolution regional model of the Arafura Sea (Condie et al. 1999) was trialled for the western model boundary, but did not improve the quality of the results. The tangential current along the model boundaries and the gradient of normal current were set to zero. In addition, the horizontal viscosity was

greatly increased in eight so-called sponge cells just inside of open boundaries, so as to damp high frequency noise in the model and maintain the numerical stability of the solution.

A fresh water riverine discharge of 1500 $m^3 s^{-1}$ was imposed along the five grid cells defining the Fly River, while 937.5 $m^3 s^{-1}$ was imposed along the eight grid cells defining the rivers Bamu, Turama and Kikori. In the north of Torres Strait, a discharge of 450 $m^3 s^{-1}$ was imposed along the three grid cells defining the Boigu River. All discharges were assumed to have a temperature of 26°C and a salinity of 12 PSU. While these fresh water discharges were only approximate, it represented the first time that local rivers had been modelled in Torres Strait.

Surface wave forcing was included in the Torres Strait model so as to improve bottom friction estimates, which was particularly significant for the embedded sediment transport model (Margvelashvili and Saint-Cast 2006). Wave characteristics in Torres Strait were modelled using the WAve Model (WAM) data supplied by the Bureau of Meteorology. WAM solves equations for the directional wave spectrum on a regular grid based on local wind input, wave dissipation, nonlinear wave-wave interactions and propagation of waves from non local sources (swell). It was run with a 12 hour assimilation period using satellite derived wave height data to provide outputs of significant wave height, period and direction on a 6 hourly time-step and a spatial resolution of 1 degree. Wave statistics computed on the hydrodynamic model grid are summarised in Figure 8, Figure 9 and Figure 10. The interpolated product generally showed good agreement with local wave measurements for sub-diurnal frequencies (Figure 11 and Figure 12). However, smaller scale variability, such as the daily wind-waves induced by sea-breezes were more poorly resolved.

Near-bottom wave characteristics such as orbital velocity, direction and frequency were calculated following Dyer's (1986) wave model. Grant and Madsen's (1979) bottom boundary layer model was then applied within the hydrodynamic model to enhance bottom shear stresses in regions where waves pass over shallow water (Figure 13). Comparisons between the interpolated WAM data and locally observed near bed orbital velocity derived after Dyer (1986) from wave data presented before again reflects good agreement with for sub-diurnal frequencies, but poor resolution of higher frequency events influenced by processes such as the sea-breeze (Figure 14).

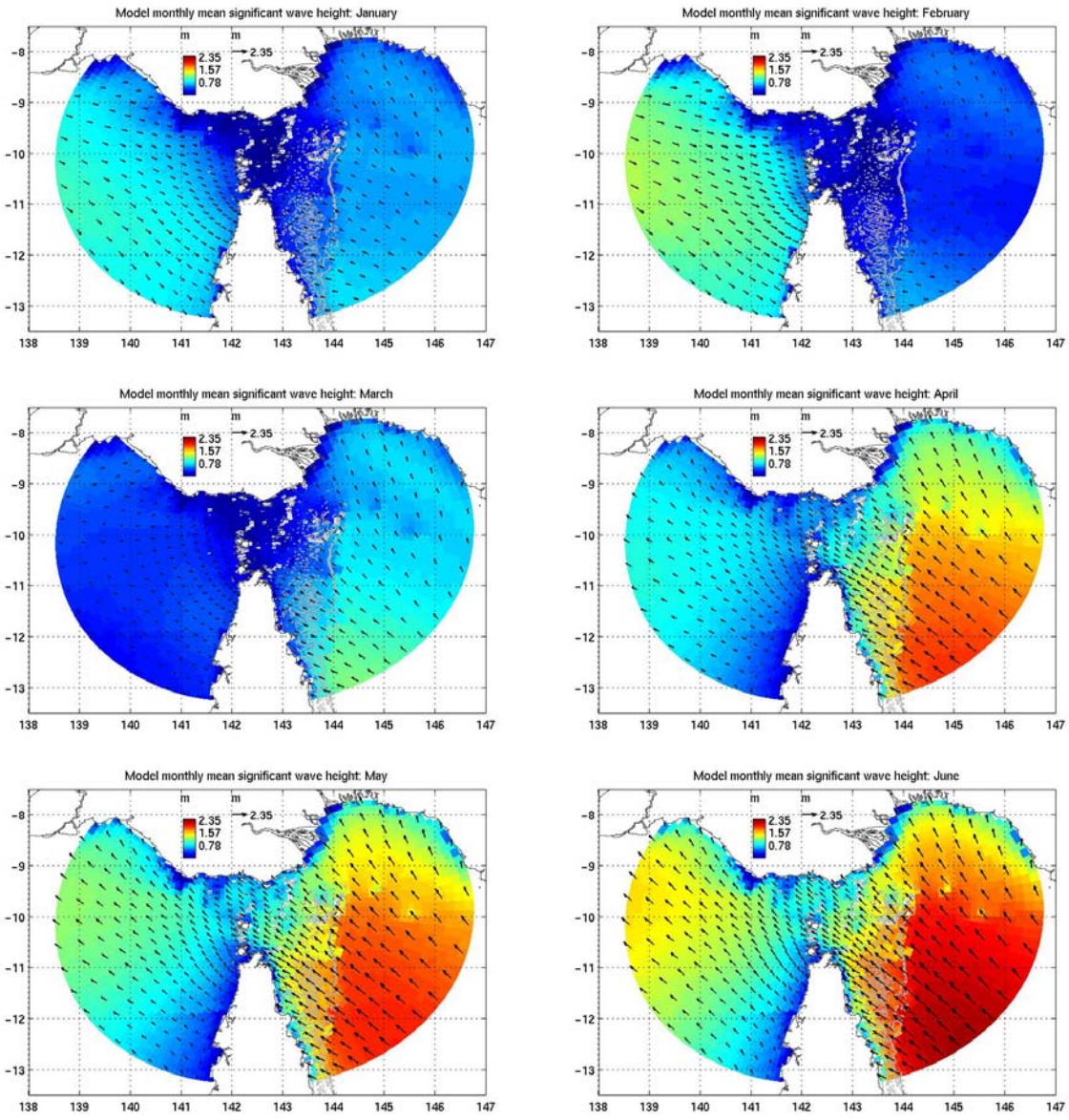

Figure 8: Monthly mean significant wave height and direction (January to June). These fields were calculated by vector averaging the 6 hourly outputs of the BOM-WAM dataset across the years 1997 to 2005. They show that wave direction followed wind direction. Wave heights peaked during the Trades and were significantly higher in the Coral Sea than in the Gulf of Carpentaria.

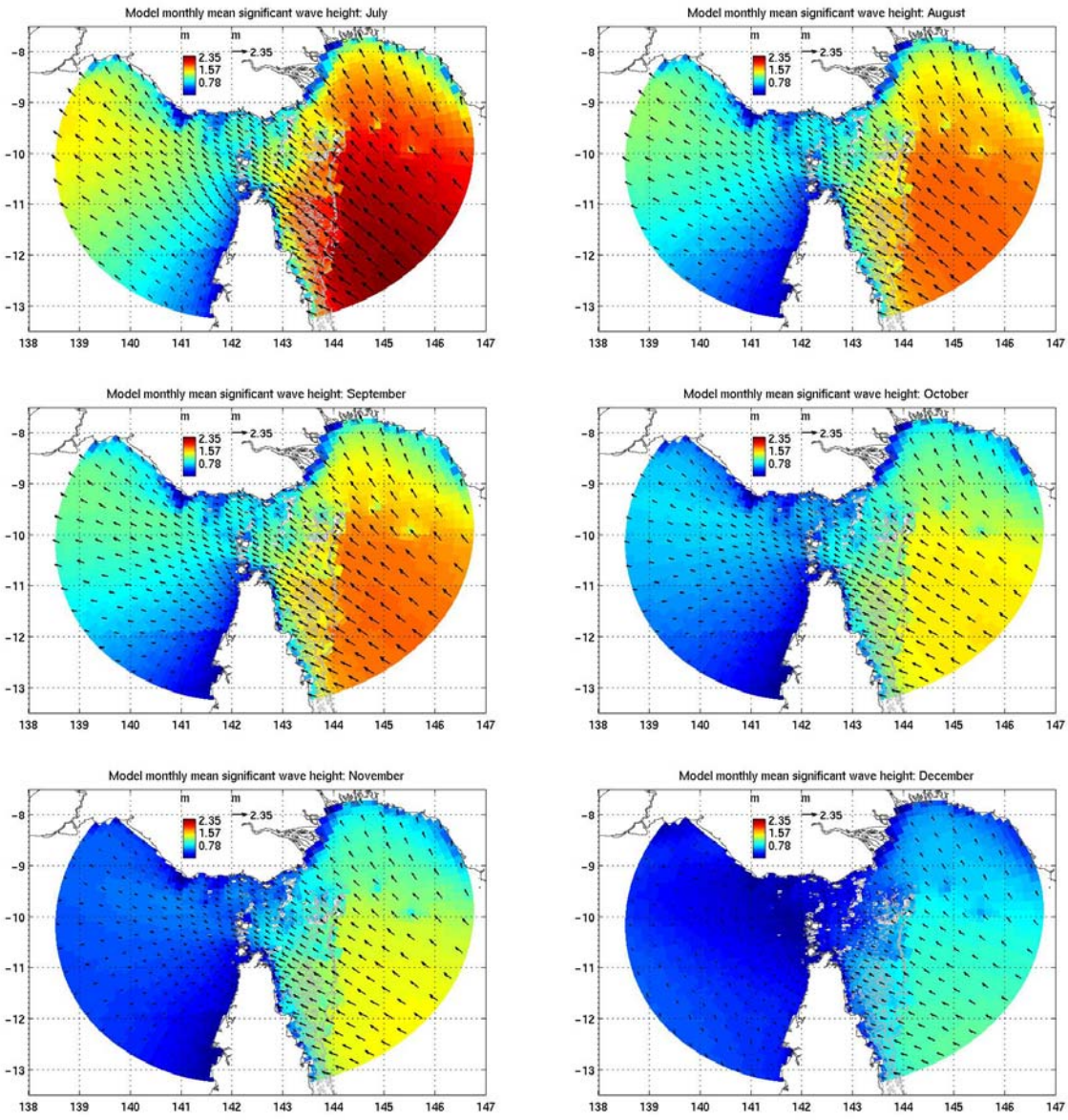

Figure 9: Monthly mean significant wave height and direction (July to December). These fields were calculated by vector averaging the 6 hourly outputs of the BOM-WAM dataset across the years 1997 to 2005. They show that wave direction followed wind direction. Wave heights peaked during the Trades and were significantly higher in the Coral Sea than in the Gulf of Carpentaria.

a)

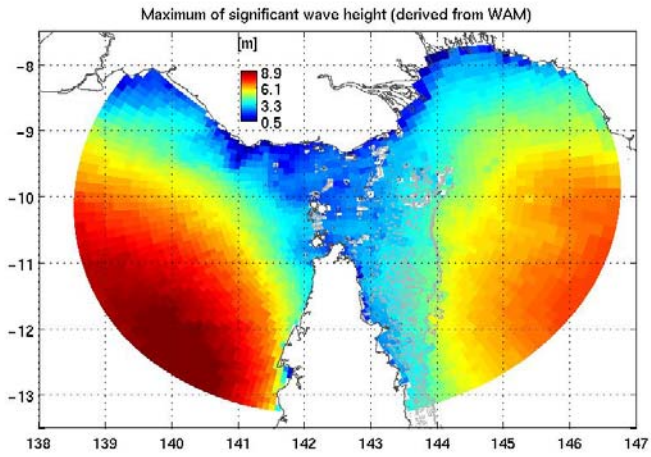

b)

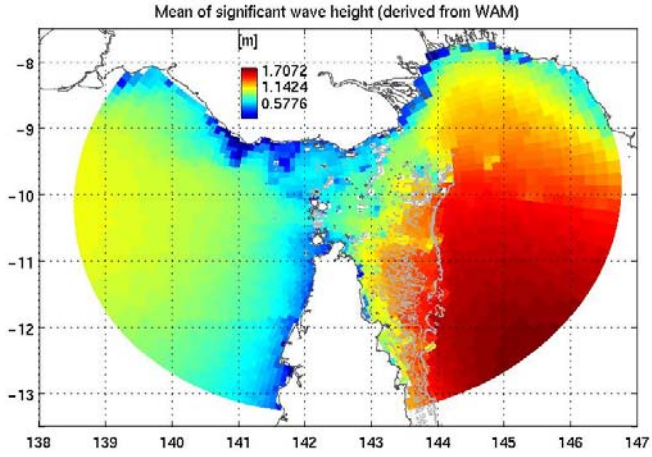

c)

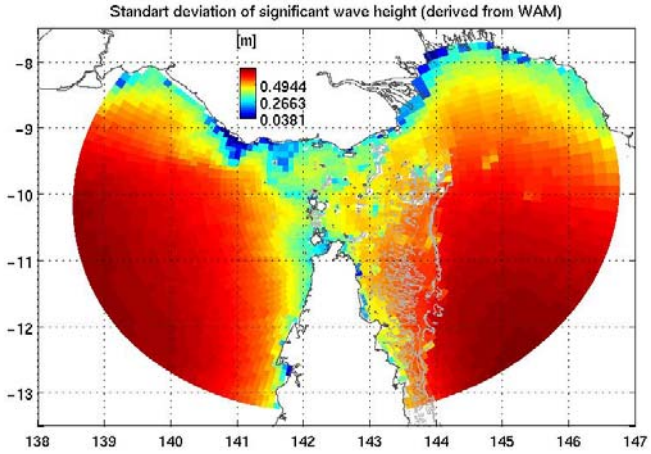

Figure 10: Significant wave height statistics on the hydrodynamic model grid: a) maximum; b) mean; and c) standard deviation. These statistics were derived from WAM outputs covering the period 01/03/1997 to 28/02/2002. Maximum wave heights of up to 9 m in the Gulf of Carpentaria were in response to a tropical depression that developed northeast of Darwin in late December 1997. In other areas of open water maximum wave heights were more typically around 7m, while in the shallow waters of Torres Strait and neighbouring coastal areas they did not exceeded 3m. Mean wave heights in northwest Torres Strait and Gulf of Papua were less than 0.6 m, increasing to around 1.0 m in the southeastern part of the Strait and Gulf of Carpentaria, and 1.5 m in the Coral Sea. While variability (as measured by the standard deviation) followed similar patterns to the mean, its magnitude in the Gulf of Carpentaria was similar to that in the Coral Sea.

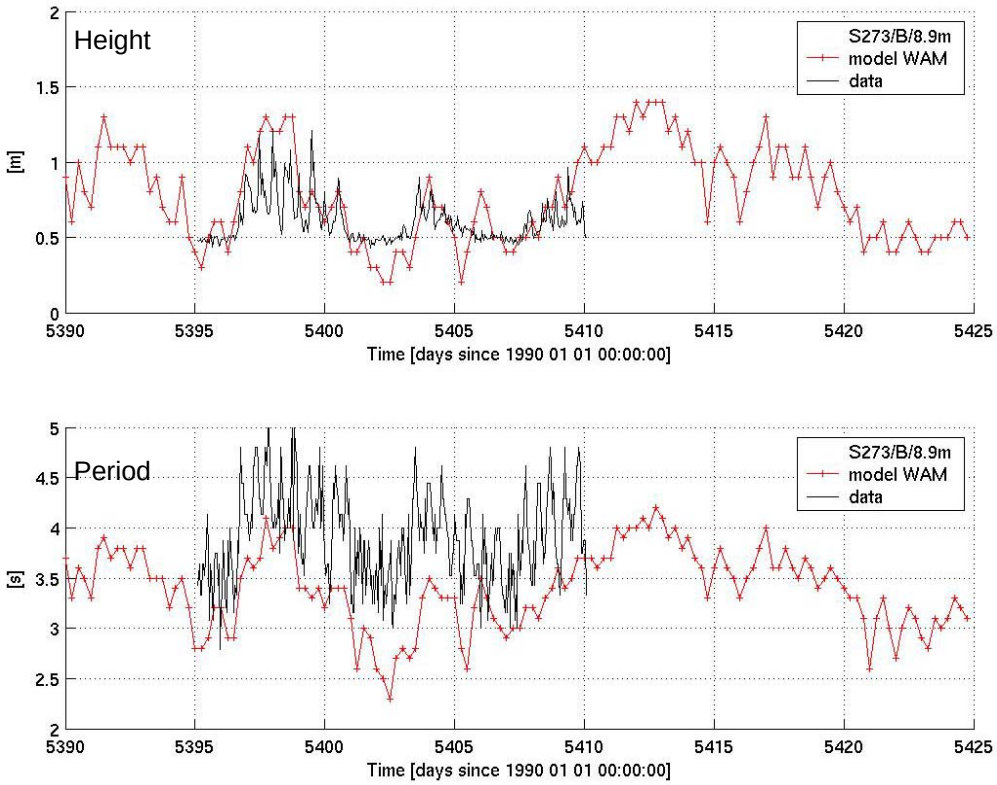

Figure 11: Time-series comparisons between the interpolated WAM data and locally observed waves characteristics, including significant wave height and period for survey 273. The direction of waves has not been measured on the field.

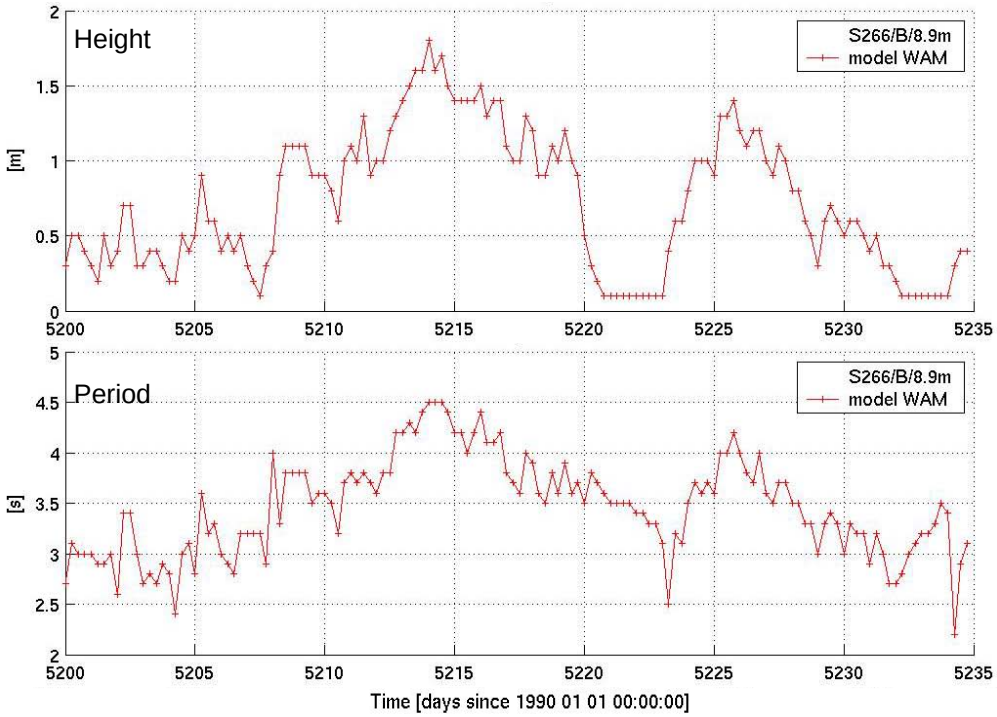

Figure 12: Waves characteristics over survey S266 period derived form WAM. No field data was available from survey S266 due to malfunction of the wave data recorder.

a)

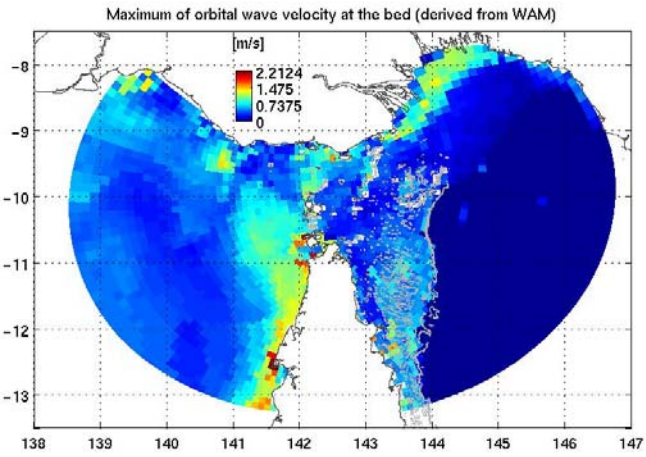

b)

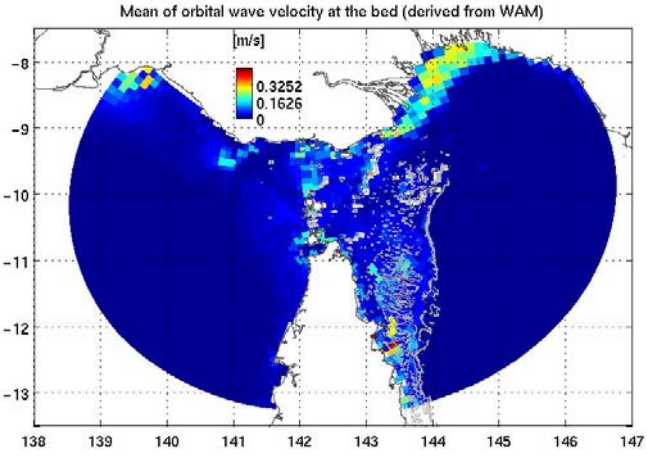

c)

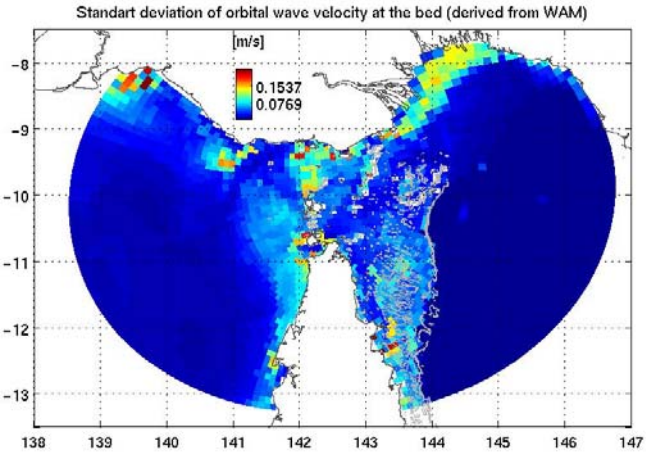

Figure 13: Wave orbital velocity statistics at the seabed: a) maximum; b) mean; and c) standard deviation. Statistics were derived from WAM outputs covering the period 01/03/1997 to 28/02/2002.

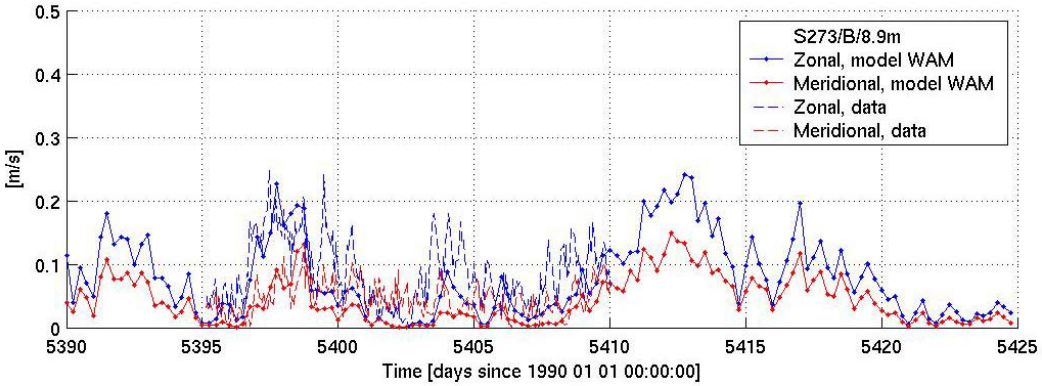

Figure 14: Time-series comparisons between the interpolated WAM data and locally observed near bed orbital velocity derived after Dyer (1986) from wave data presented before. No field data were available for survey S266 due to malfunctioning wave data recorder.

3.2 Model runs and outputs

The Torres Strait model was used to simulate the circulation for a total of eight years, extending from March 1997 to December 2004. This particular period was chosen for three main reasons: first, to utilise the most recent atmospheric and oceanographic fields in forcing the Torres Strait model (Section 3.1); second, to validate model results over a broad range of historical and recent field data and time series, including tides, winds, waves, salinity and temperature (Section 4); and third, to generate a sufficiently long model output time series to adequately analyse seasonal and inter-annual variability in the circulation of Torres Strait (Section 5).

Since the model had the potential to generate unmanageably large quantities of output, fields were saved selectively so as to resolve the most significant processes at appropriate temporal and spatial scales. The final selection included saving two-dimensional fields hourly and three-dimensional fields every 15 days as summarized in Table 1. While the results will not be described in detail until Section 5, sample outputs of sealevel and surface currents are shown here from the global OFAM model and the regional Torres Strait model (Figure 15).

Table 1: Gridded outputs saved from the circulation model.

Quantity	Temporal Resolution	
	Hourly	15 daily
Sealevel	X	
3-D temperature		X
Surface temperature	X	
3-D salinity		X
Surface salinity	X	
3-D currents		X
Surface currents	X	
Depth averaged currents	X	
Bottom stress	X	
3-D vertical viscosity		X
3-D vertical diffusivity		X

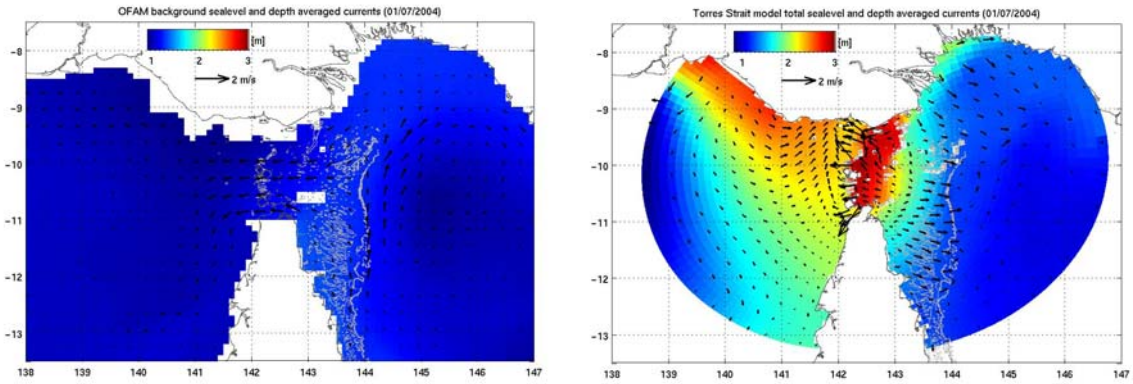

Figure 15: Sample outputs from OFAM showing background sealevel and depth averaged currents vectors (subsampled), and from the Torres Strait model showing total sealevel (including tide) and depth averaged current vectors (subsampled) on 1 July 2004.

4 Model validation

The model included a relatively large number of input parameters and an understanding of their influence on the model response provided one measure of uncertainty. However, there were additional uncertainties associated with both the model structure (i.e. parameterizations of sub-grid scale processes) and model forcing (i.e. winds and lateral boundary conditions), which could only be quantified through comparisons with field observations within the Torres Strait region. The main observations used for this purpose were (i) sealevel measurements routinely collected at coastal stations using tide gauges, (ii) temperature and salinity profiles collected during scientific voyages in the Coral Sea, and (iii) current meter time-series collected by moored instruments during dedicated field work in Torres Strait.

4.1 Sensitivity analysis

Sensitivity analyses undertaken for previous implementations of the SHOC model suggest that model results are largely insensitive to the tuneable model parameters and available model structure options, provided parameter values are within a physically feasible range and do not violate model stability (Condie et al. 1999, 2002; Hemer et al. 2004). In the following, a range of parameters affecting the quality of the Torres Strait model results are discussed and the parameter set that was finally adopted is presented. The most significant internal parameters were the vertical mixing coefficients, the seabed roughness length and bottom drag coefficient. However, modifications to the tidal forcing were probably more significant in gaining agreement with observations.

4.1.1 Diffusivities

The profile of temperature and salinity in the upper water column was strongly affected by the parameterization of the vertical mixing. Vertical diffusion rates of temperature and salinity in stratified waters were not realistically represented by the Csanady (1982) vertical mixing model. The Mellor and Yamada (1982) level 2 scheme was therefore adopted to account for the stratification, as suggested by Condie et al. (2003). This scheme was dependent on background viscosity and diffusivity coefficients, which were set to $V_z = 0.0005$ m^2/s and $K_z = 0.00025$ m^2/s respectively as suggested by Bowden and Hamilton (1975). Reducing these values by up to a factor of 5 had little influence on temperature or salinity profiles, while further reductions lead to model instabilities. The Mellor and Yamada scheme also required specification of a surface length scale, which was set to $z_s = 0.3m$. Results were again insensitive to this parameter. The comparison of modelled temperature and salinity profiles with observations is presented in subsection 4.3.

4.1.2 Bottom boundary layer characteristics

The model was run using the two bathymetry products described by Daniell (2004) and Daniell (2005). While the latter was known to be a more accurate product, comparisons provided an indication of the sensitivity of the model to errors in the bathymetry (Table 2 and Figure 13). While reducing the number of vertical cells of the z-coordinate grid had only a small impact on the circulation, coarse grid cells introduced significant stepping of the bathymetry that impacted bedload transport in the sediment transport model (Margvelashvili and Saint-Cast 2006).

The bed friction parameterization (Appendix 9.2) had only limited impact on sea level predictions (Table 3). However, it allowed fine-tuning of the current strength. A number of scenarios were tested considering two uniform bed roughness heights (z_0) and two minimum bottom drag coefficients ($C_{D,min}$). The strongest correlations with observed currents were achieved by setting z_0=0.005m and $C_{D,min}$=0.0005 (Table 4).

Table 2: Summary of the tidal sea level calibration tests comparing model outputs with Admiralty Table estimates. Linear regression coefficients (s) and correlation coefficients (r2) are estimated for the year 1998 and designated as good if |s-1|<0.2 and |r2-1|<0.2, poor if |s-1|>0.4 and |r2-1|>0.4, and average otherwise.

Test	Bathymetry according to Daniell [year]	Bed roughness height [m]	Minimum bottom drag coefficient	Gulf tidal correction factor	Number of ports in Admiralty database where model correlation is [good, average, poor]
E	2004	0.0005	0.003	1	15, 18, 18
H	2004	0.0005	0.003	10 / 7	31, 08, 12
L	2005	0.0005	0.003	10 / 7	28, 15, 08
M	2005	0.0005	0.003	10 / 6	27, 16, 08
N	2005	0.0005	0.0005	10 / 6	32,10, 09 Good agreement with S266, S273 and NTC
O	2005	0.005	0.0005	10 / 6	31,11,09 Very good agreement with S266, S273 and NTC

4.1.3 Boundary conditions

Tidal sealevels in Torres Strait were strongly influenced by the quality of the tidal signals applied along open boundaries. While outputs from the global tidal model produced satisfactory results on the eastern side of the strait, there was much poorer agreement on the western side. This was to be not surprising given that global tidal models generally perform poorly in shallow water and the Gulf of Carpentaria is less than 70 m deep. Using tidal sealevels from a regional-scale model of the Arafura Sea (Condie el al. 2002) did not produce any significant improvement. However, when tidal amplitudes from the global model were scaled by an optimal correction factor of 10/6 in the Gulf of Carpentaria, the number of ports showing good quality correlation with observed coastal ports sealevel doubled (Table 2).

Table 3: Calibration of modelled sealevel against field data time series for two model runs. s is the linear regression coefficient and r2 is the correlation coefficient. The 10-fold increase of the roughness height improved significantly the sea level accuracy of the model. Model run N over-estimates the sealevel data by 10%. Model run O agrees very well with data.

	Model test	**N (z_0=0.0005m)**		**O (z_0=0.005m)**	
Instruments name	**Water depth [m]**	**s**	**r2**	**s**	**r2**
S266/cm2	9.15	1.09	0.74	1.02	0.85
S266/cm3	7.78	1.13	0.82	0.96	0.76
S273/cm7	4.83	1.33	0.90	1.15	0.89
S273/cm6	10.78	1.06	0.87	0.94	0.89
NTC/Booby Isl.		1.05	0.93	0.95	0.92
NTC/Goods Isl.		1.13	0.92	1.03	0.92
NTC/Turtle Head		0.99	0.93	0.92	0.92
NTC/Ince Pt.		1.11	0.79	1.07	0.81
average		1.11	0.86	1.00	0.87

Table 4: Calibration of modelled current against field data time series measured at 1.6m above the bed by ADCPs. S is the linear regression coefficient and r2 is the correlation coefficient. Values are quoted for the east component and north component (in brackets). The first line corresponds to bottom currents estimated from the depth averaged current, while the second line corresponds to bottom currents estimated from the current 2 cells above the bottom cell (see Appendix 9.2 for details of these calculations). Bottom currents from test O are in relatively good agreement with field data. However, a 10-fold increase of the roughness height improved significantly the bottom current accuracy of the model.

	Model test	**N (z0=0.0005m)**		**O (z0=0.005m)**	
station name	**Water depth [m]**	**s**	**r2**	**s**	**R2**
S266/cm2	9.15	1.59 (0.50)	0.75 (0.10)	1.12 (0.31)	0.69 (0.06)
		1.79 (0.47)	0.77 (0.08)	1.30 (0.29)	0.71 (0.05)
S266/cm3	7.78	1.26 (0.43)	0.71 (0.26)	0.87 (0.37)	0.65 (0.32)
		1.39 (0.77)	0.74 (0.77)	0.82 (0.62)	0.69 (0.73)
S273/cm7	4.83	1.17 (1.15)	0.64 (0.44)	0.85 (1.00)	0.63 (0.50)
		1.21 (1.49)	0.64 (0.62)	0.87 (1.24)	0.63 (0.65)
S273/cm6	10.78	1.56 (0.42)	0.87 (0.07)	1.12 (0.29)	0.84 (0.05)
		1.81 (0.41)	0.88 (0.06)	1.35 (0.28)	0.87 (0.04)
Average		1.39 (0.62)	0.75 (0.21)	0.99 (0.49)	0.70 (0.23)
		1.55 (0.78)	0.75 (0.38)	1.08 (0.60)	0.72 (0.36)

4.2 Comparison with observed sea level

Modelled sealevels were compared with measured and predicted sealevel time series from a range of coastal stations (Figure 16). Long term records of sealevel were available from the National Tidal Centre (NTC) at Torres Strait standard ports, including Ince Point, Turtle Head, Good Island and Booby Island (Figure 17 and Figure 18). Short sealevel time series

were also available from Torres Strait marine surveys S266 (Heap et al. 2005) and S277 (Daniell et al. 2006). Tidal predictions at a number of other standard ports (i.e. Weipa, Thursday Island, Twin Island and Port Moresby) and secondary ports were derived from the Admiralty tidal harmonics and a tide calculator (Flater, 1999). Modelled tide levels were compared against predicted time series, while the sub-tidal frequency component was compared with the long term tide gages record.

4.2.1 Tides

The tidal component clearly dominated the sealevel signal. There was generally good agreement in the phase and amplitude at all the stations (Figure 19 and Figure 20) and in many instances the model reproduced the observed tides as well as the Admiralty Tables (Figure 21). While reproduction of the tidal signal tended to deteriorate down the west coast of Cape York Peninsula, correlations were 'good' at the vast majority of stations (Table 5 and Figure 16).

4.2.2 Sub-tidal frequency sea level

The low-frequency component of the sealevel signal was extracted by low-pass filtering the sealevel timeseries at 40-hours and 90-days (Figure 23 and Figure 24). These two timescales were chosen to reveal variability associated with the continental shelf wave response to synoptic weather systems and variability associated with the monsoon and trades season respectively. The model captured very well the amplitude and phase of the seasonal sea surface oscillations, as well as the rapid attenuation between Booby Island and Ince Point of these through-strait oscillations (Figure 25). The discrepancies in mean sealevel at Ince Point may be associated with the 1 grid cell width confinement of the flow through the Prince of Wales Channel. Comparisons improved as the coastal sealevel signal propagated to the west in more open waters.

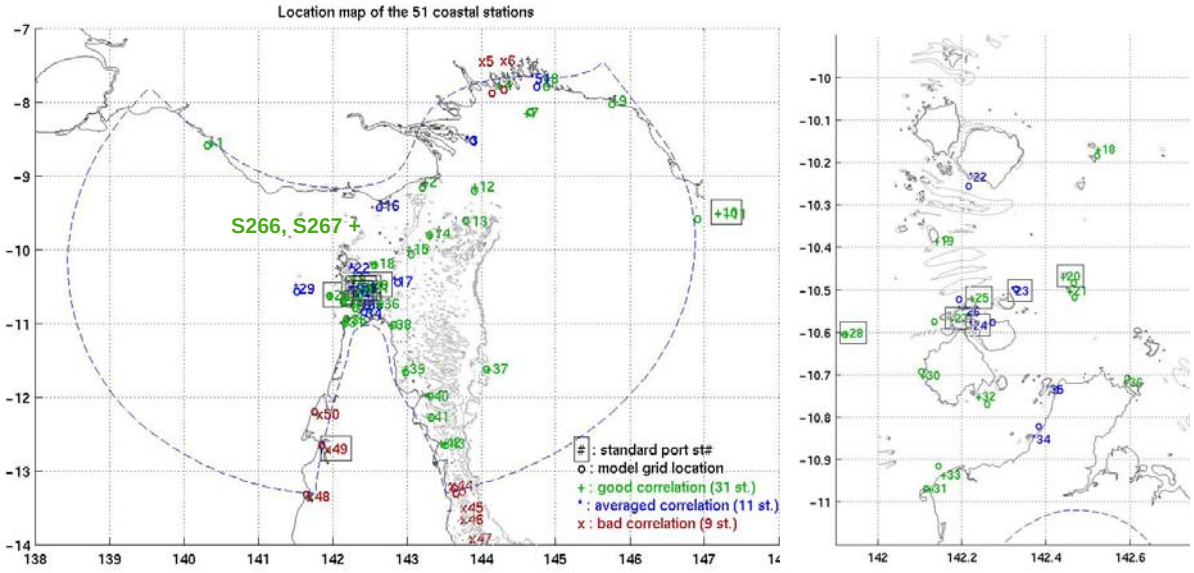

Figure 16: Location of tidal stations, including Admiralty coastal ports and recent survey moorings, used to validate model sealevel estimates. The quality of correlation with observed sealevel is represented by: (+) good quality corresponds to |s-1|<0.2 and |r2-1|<0.2, (x) poor quality correspond to |s-1|>0.4 & |r2-1|>0.4 and (*) averaged quality otherwise

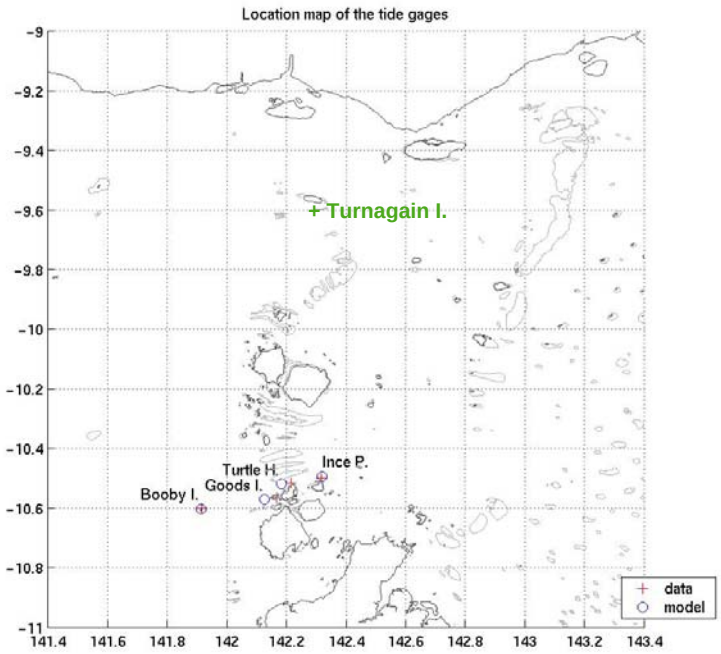

Figure 17: Location map of the four standard port tide gages in Torres Strait, where long term sealevel time series were available. Only short term sealevel time series were available at Turnagain Island.

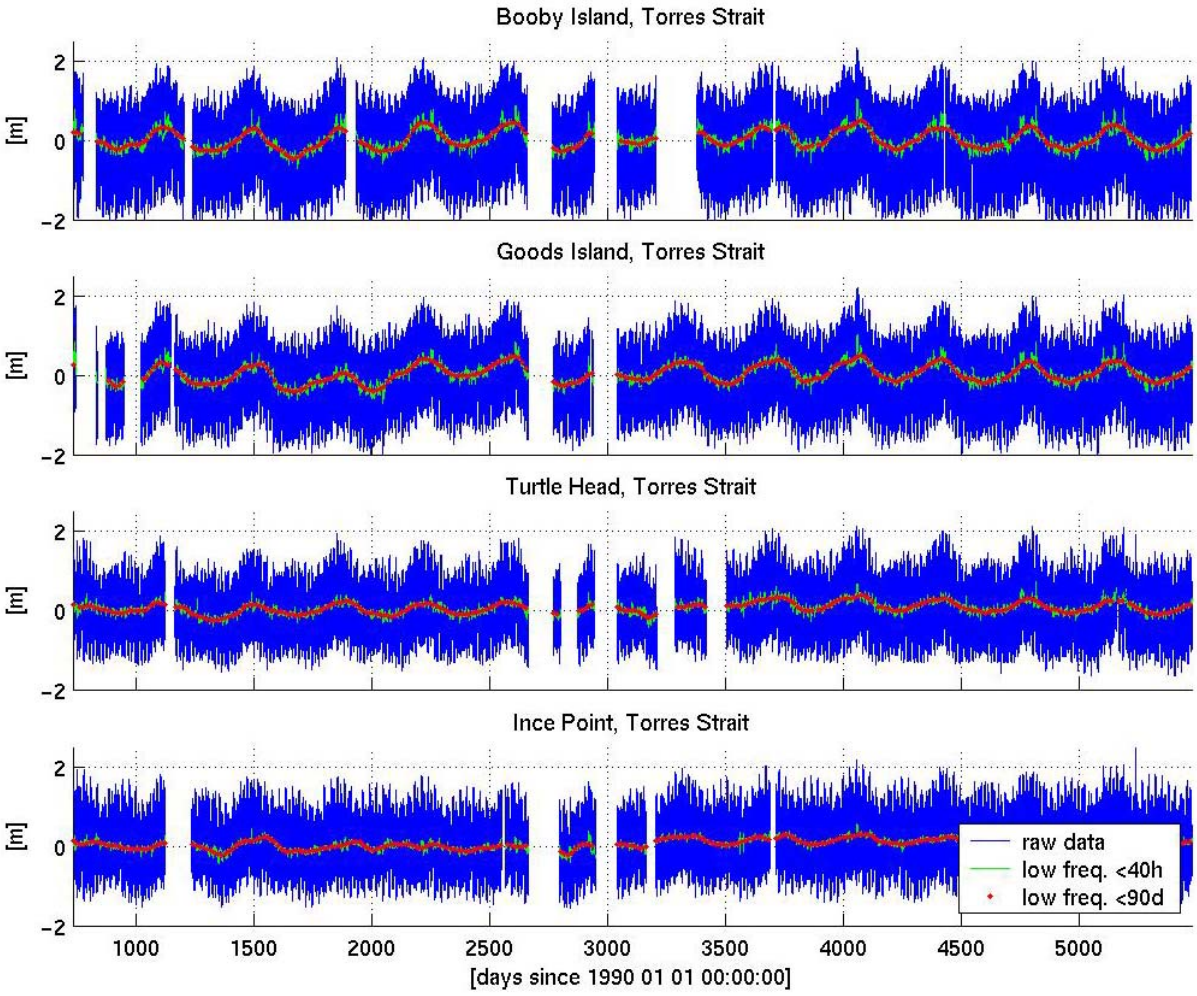

Figure 18: Four standard ports tide gage time series from 1992 to 2005. Raw data (blue), low pass filtered data at a cut off period of 40h (green) and 90d (red).

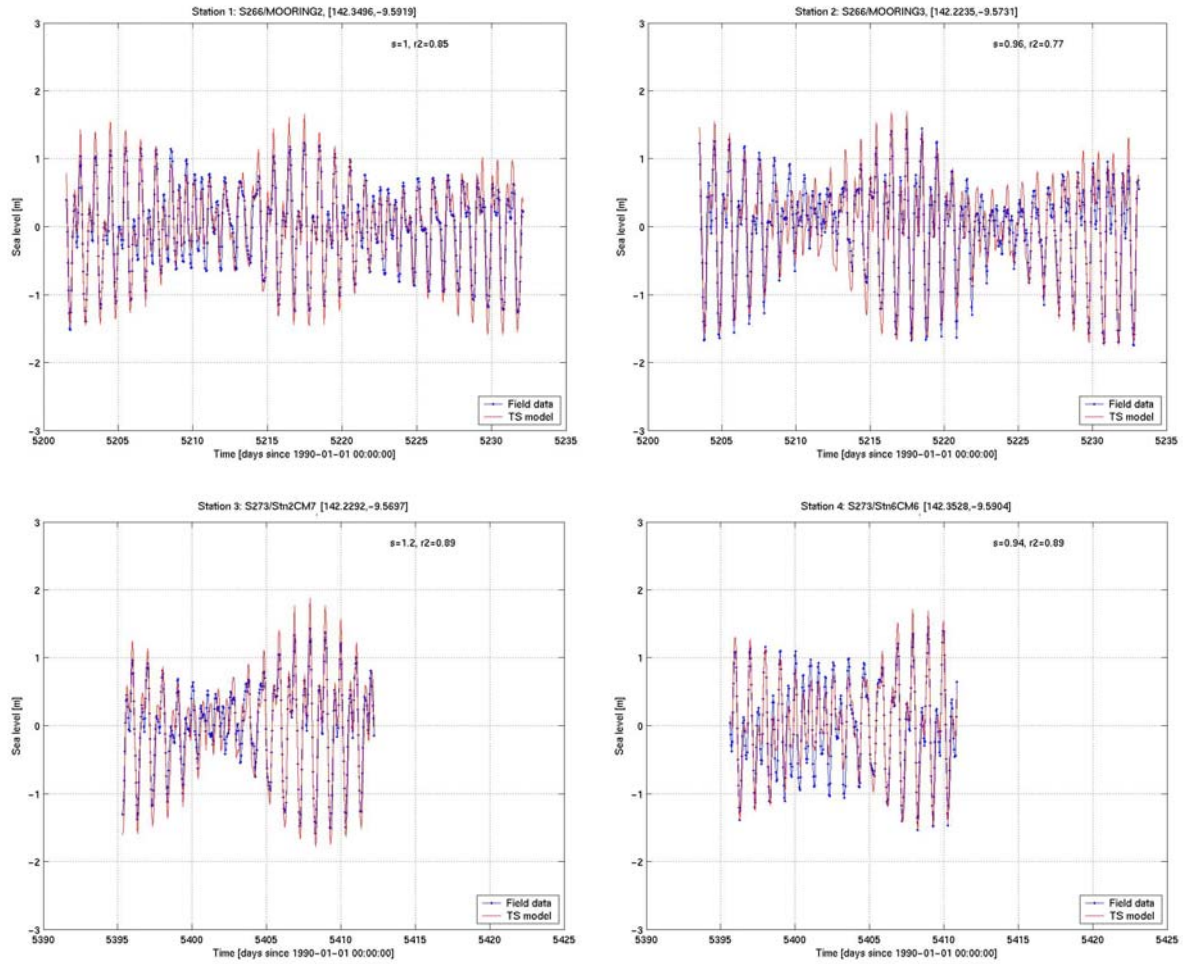

Figure 19: Comparison between modelled and observed sea level at Turnagain Island from surveys S266 and S273.

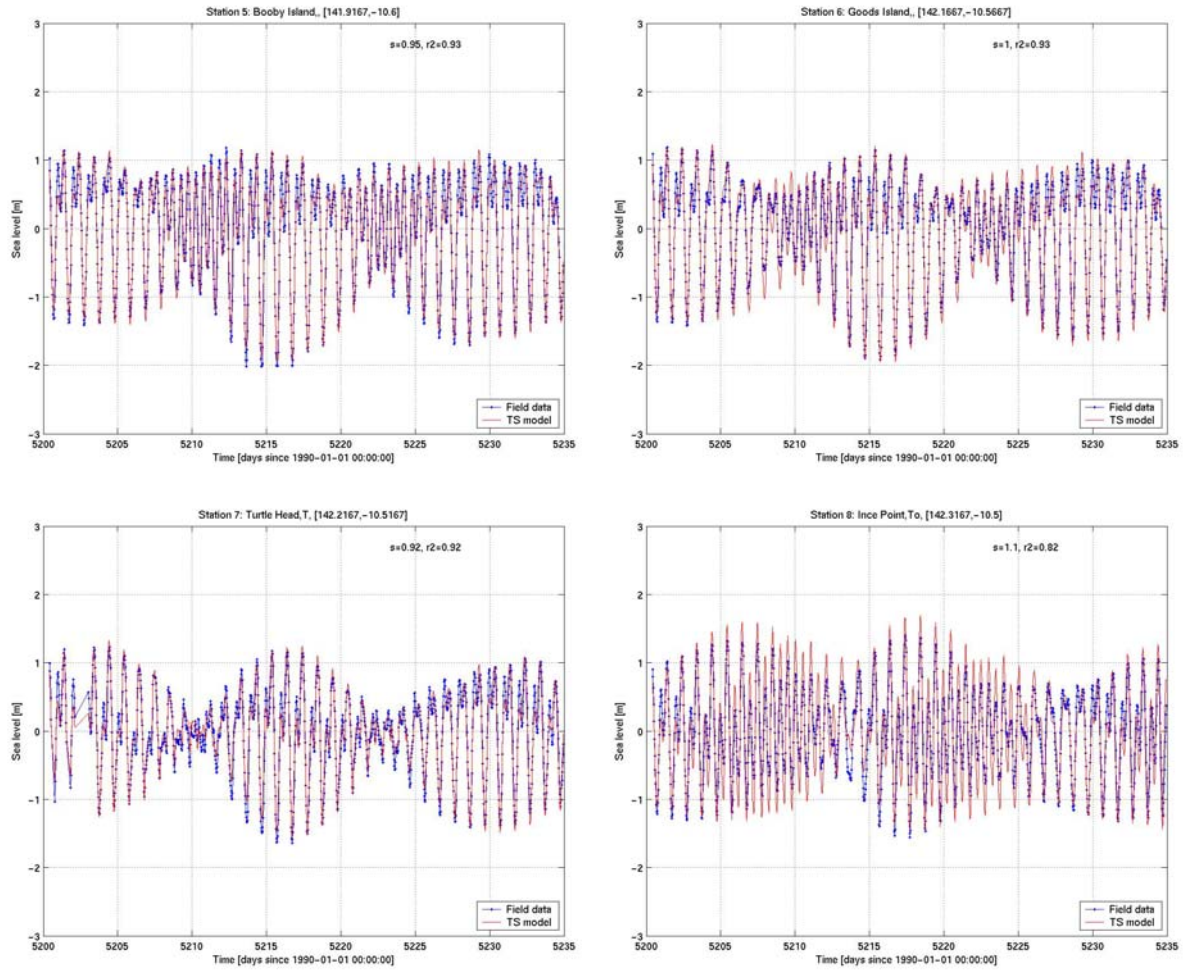

Figure 20: Comparison between modelled and observed sea level at NTC tide gages.

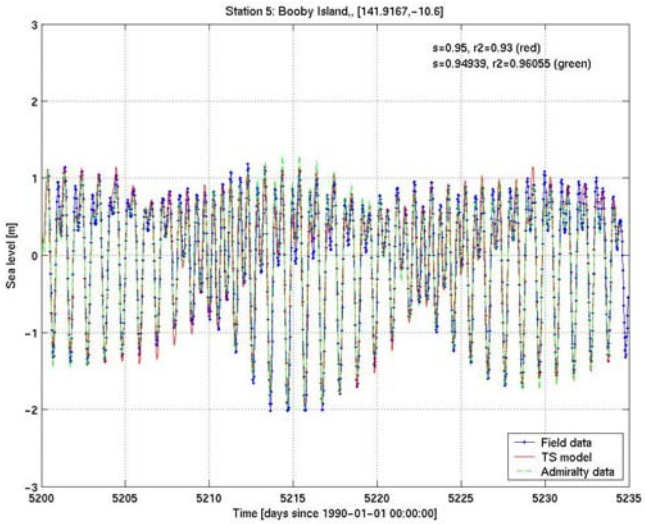

Figure 21: Sea level comparison at Booby Island. Model output from test O and reconstructed sea level from the Admiralty harmonic database are both in very good agreement with field data from the NTC tide gage.

Table 5: Linear regression slope (s) and correlation coefficient (r2) values for modelled vs. predicted tide for year 1998 (station #1-51) and observed tide (S266, S273 and NTC). The quality of the correlation is rated "good" if |1-s| and |1-r2| are lower than 0.2, "poor" if |1-s| or |1-r2| is greater than 0.4, and "average" otherwise.

Station	name	location	s	r2	Quality	Comment
S266/cm2	Turagain Island	Torres Strait	1.02	0.85	Good	Comparison model vs. time series
S266/cm3	Turagain Island	Torres Strait	0.96	0.76	Average	Comparison model vs. time series
S273/cm7	Turagain Island	Torres Strait	1.15	0.89	Good	Comparison model vs. time series
S273/cm6	Turagain Island	Torres Strait	0.94	0.89	Good	Comparison model vs. time series
NTC	Booby Isl.	Torres Strait	0.95	0.92	Good	Comparison model vs. time series
NTC	Goods Isl.	Torres Strait	1.03	0.92	Good	Comparison model vs. time series
NTC	Turtle Head	Torres Strait	0.92	0.92	Good	Comparison model vs. time series
NTC	Ince Pt.	Torres Strait	1.07	0.81	Good	Comparison model vs. time series
1	Merauke	Indonesia	0.97	0.90	Good	
2	Daru	P. N. G.	0.94	0.97	Good	Coarse mesh, very shallow
3	Umuda Island	P. N. G.	0.97	0.77	Average	
4	Goaribari Island	P. N. G.	0.95	0.85	Good	Coarse mesh, very shallow
7	Kumul Tkr Mrg	P. N. G.	0.96	0.91	Good	
8	Port Romilly	P. N. G.	0.89	0.87	Good	
9	Kerema	P. N. G.	0.98	0.94	Good	
10*	Port Moresby	P. N. G.	0.94	0.97	Good	Standard port
11	Bootless Inlet	P. N. G.	1.01	0.91	Good	
12	Bramble Cay	Coral Sea	1.14	0.86	Good	
13	Darnley Island	Coral Sea	0.99	0.81	Good	
14	Rennel Island	Coral Sea	1.05	0.81	Good	
15	Dungeness Reef	Coral Sea	1.08	0.95	Good	
16	Saibai Island	Torres Strait	0.87	0.78	Average	Coarse mesh
17	Kirkcaldie Reef	Torres Strait	1.24	0.93	Average	
18	Suarji Island	Torres Strait	1.04	0.92	Good	
19	Hawkesbury Island	Torres Strait	0.98	0.89	Good	
20*	Twin Island	Torres Strait	1.10	0.88	Good	Standard port
21	East Strait Island	Torres Strait	1.07	0.85	Good	
22	Moa Island	Torres Strait	0.99	0.72	Average	
23*	Ince Point	Torres Strait	1.09	0.75	Average	Standard port
24*	Thursday Island	Torres Strait	1.01	0.72	Average	Standard port
25*	Turtle Head	Torres Strait	1.00	0.89	Good	Standard port
26	Round Island	Torres Strait	0.92	0.79	Good	
27*	Goods Island	Torres Strait	1.08	0.86	Good	Standard port
28*	Booby Island	Torres Strait	1.01	0.85	Good	Standard port
29	Proudfoot Shoal	Torres Strait	1.04	0.72	Average	
30	Bampfield Head	Endeavour St.	0.92	0.81	Good	
31	Crab Island	Endeavour St.	1.08	0.83	Good	
32	Tarilag Island	Endeavour St.	0.96	0.84	Good	
33	Herald Camp	Endeavour St.	0.95	0.90	Good	
34	Red Island	Endeavour St.	0.96	0.76	Good	
35	Possession Island	Endeavour St.	1.14	0.71	Average	
36	Albany Island	Endeavour St.	1.08	0.93	Good	
37	Raine Island	Endeavour St.	0.97	0.91	Good	
38	Tern Island	Australia	1.04	0.90	Good	
39	Hannibal Island	Australia	1.03	0.93	Good	
40	Cape Grenville	Australia	0.99	0.88	Good	
41	Piper Island	Australia	0.96	0.95	Good	
42	Port. Roads	Australia	0.88	0.89	Good	
43	Restoration Island	Australia	0.94	0.94	Good	
48	Archer River	Australia	0.77	0.50	Poor	
49*	Weipa	Australia	0.78	0.54	Poor	Standard port
50	Pennefather R.	Australia	0.94	0.53	Poor	
51	Uramu Island	P. N. G.	0.78	0.78	Average	
	All stations		0.99	0.84	Good	Mean values across all stations

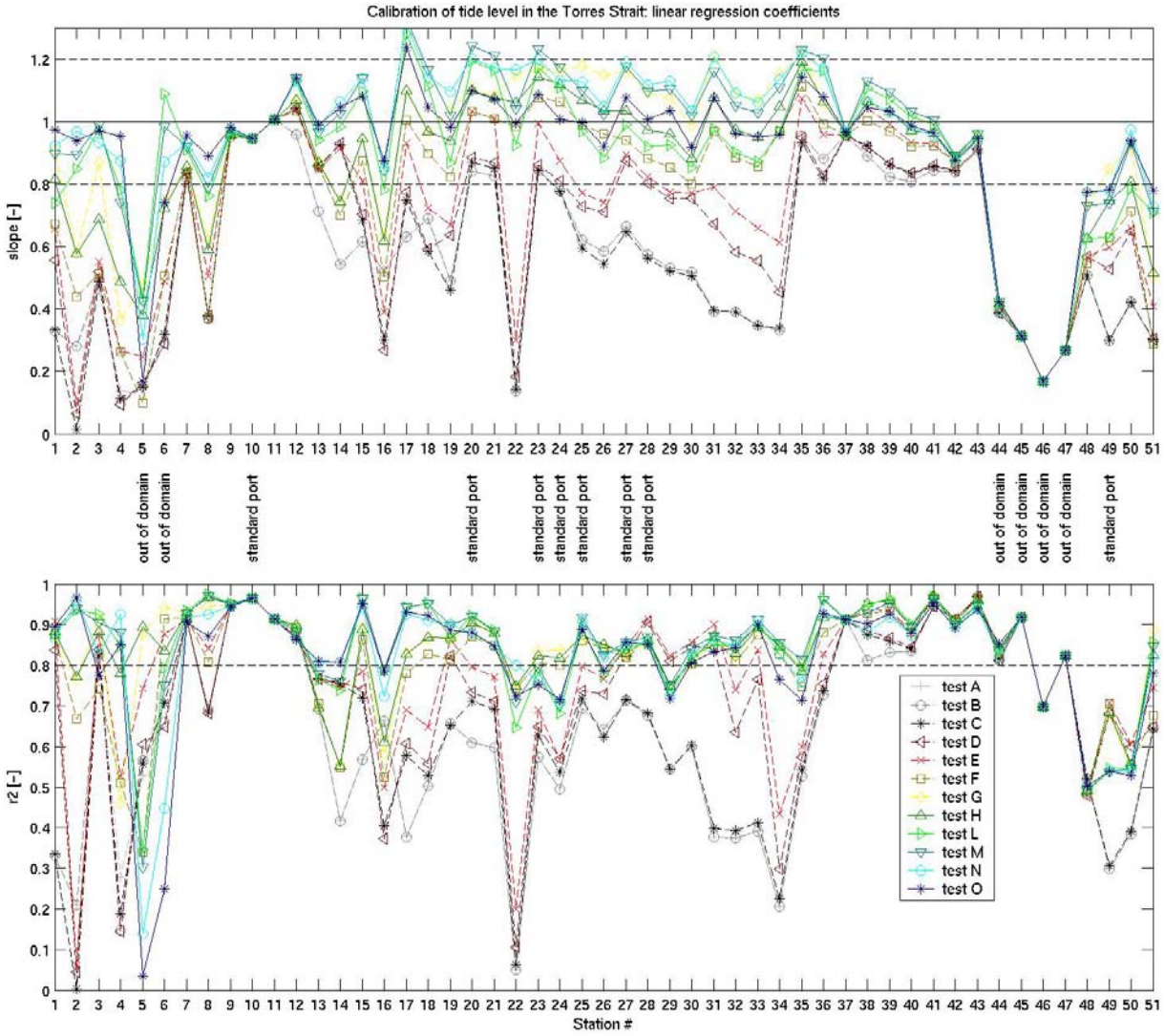

Figure 22: Summary of linear regression coefficients comparing model outputs with Admiralty Table estimates at 51 stations. Linear regression coefficients (s) and correlation coefficients (r2) are estimated for the year 1998 and designated as good if |s-1|<0.2 and |r2-1|<0.2, poor if |s-1|>0.4 and |r2-1|>0.4, and average otherwise.

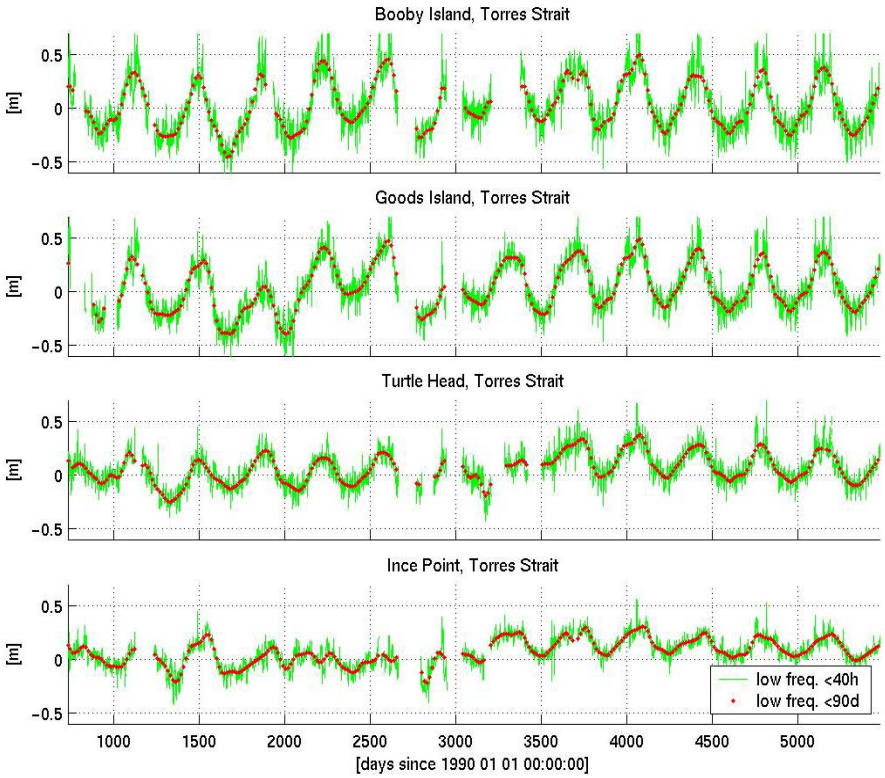

Figure 23: Low pass filtered tide gage data using a cut off period of 40 hours (green) and 90 days (red).

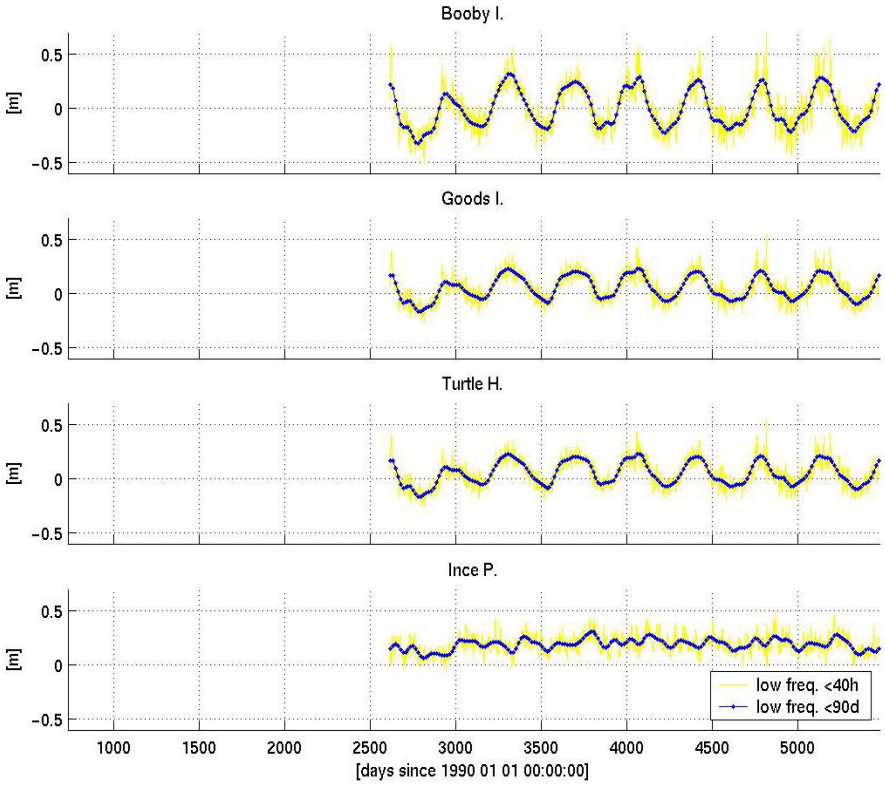

Figure 24: Low pass filtered model sea level time series using a cut off period of 40 hours (yellow) and 90 days (blue).

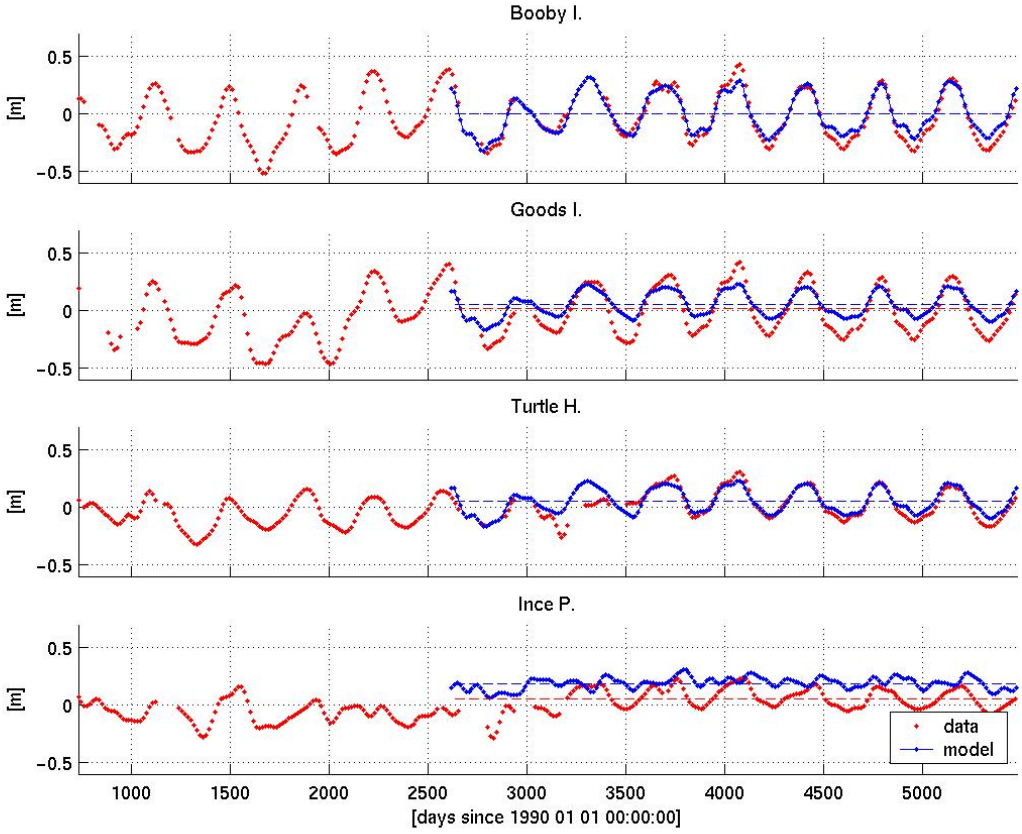

Figure 25: Comparisons of low pass filtered sealevel (90-day cut off period) at four standard ports in the Torres Strait. The dash line represents the mean sea level over an 8-year period between 1997 and 2005. Modelled sea levels are related to a common reference level, here the mean sea level at Booby Island. Observed sea levels are related to their local long term mean value.

4.3 Comparison with observed temperature and salinity

A number of temperature and salinity profiles were available from past research voyages within the Torres Strait model grid region. These were compared with outputs from the model. Since the model relied on the temperature and salinity fields from the global OFAM model for both lateral boundary conditions and interior relaxation, the comparisons are as much a test of the OFAM outputs as of the nested Torres Strait model. Thirty-five stations were selected from the oceanographic database (Ridgway et al., 2002) within the period March 1997 to March 2002, all of which were east of Torres Strait (Figure 26). A detailed comparison of temperature and salinity profiles at six stations in the deep waters of the Coral Sea (Figure 27) and six stations on the continental shelf in the Gulf of Papua (Figure 28). The regional Torres Strait model was generally in good agreement with the data, with a better representation of the mix layer depth than the global model. The correlation resulting from the linear regression between the data and both the Torres Strait model and OFAM model for all the stations are summarized on Table 6.

Comparisons between individual profiles of observed and modelled temperature and salinity suggested that many of the significant features were captured by the models, such as the vertical temperature gradients within the thermocline and the depth of the subsurface salinity maxima (Figure 27 and Figure 28). The magnitude of the salinity maxima was more

accurately reproduced by OFAM than the Torres Strait model (Figure 27), suggesting that vertical mixing at these depths may have been excessive. In most instances, the depth of the surface mixed layer was also adequately represented, although in some cases it was overestimated by up to a factor of two (Figure 25).

More comprehensive comparisons of the temperature and salinity fields were provided by plotting model outputs against observations (Figure 29 and Figure 30). These plots reveal little systematic bias in OFAM temperatures, while the Torres Strait model had a tendency to overestimate temperature below 20°C. There was significant scatter in the OFAM salinity comparison, where very low salinities were also underestimated. Nesting of the Torres Strait model tended to improve these comparisons, presumably at least in part due to improved representation of the Fly River plume.

Differences between the model and observations might be attributed to the relatively coarse resolution of the OFAM output fields, toward which the Torres Strait model was relaxed. The comparison between measured and modeled temperature and salinity profiles described previously suggest that vertical diffusion rates may have been overestimated by the global model and the regional model. However, these inaccuracies are expected to be most significant in the deep waters of the Coral Sea, rather than the well-mixed waters of Torres Strait.

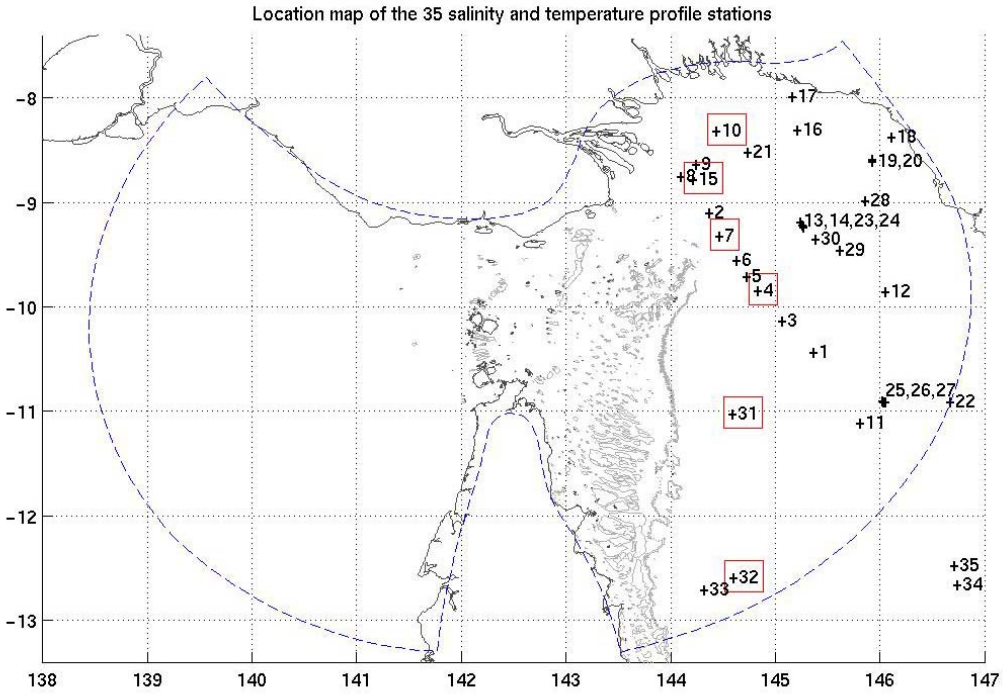

Figure 26: Location map of 35 stations where temperature and salinity profiles have been calibrated against oceanographic data available within the period 1997-2002. Temperature and salinity profiles at boxed stations are shown in Figure 27 and Figure 28.

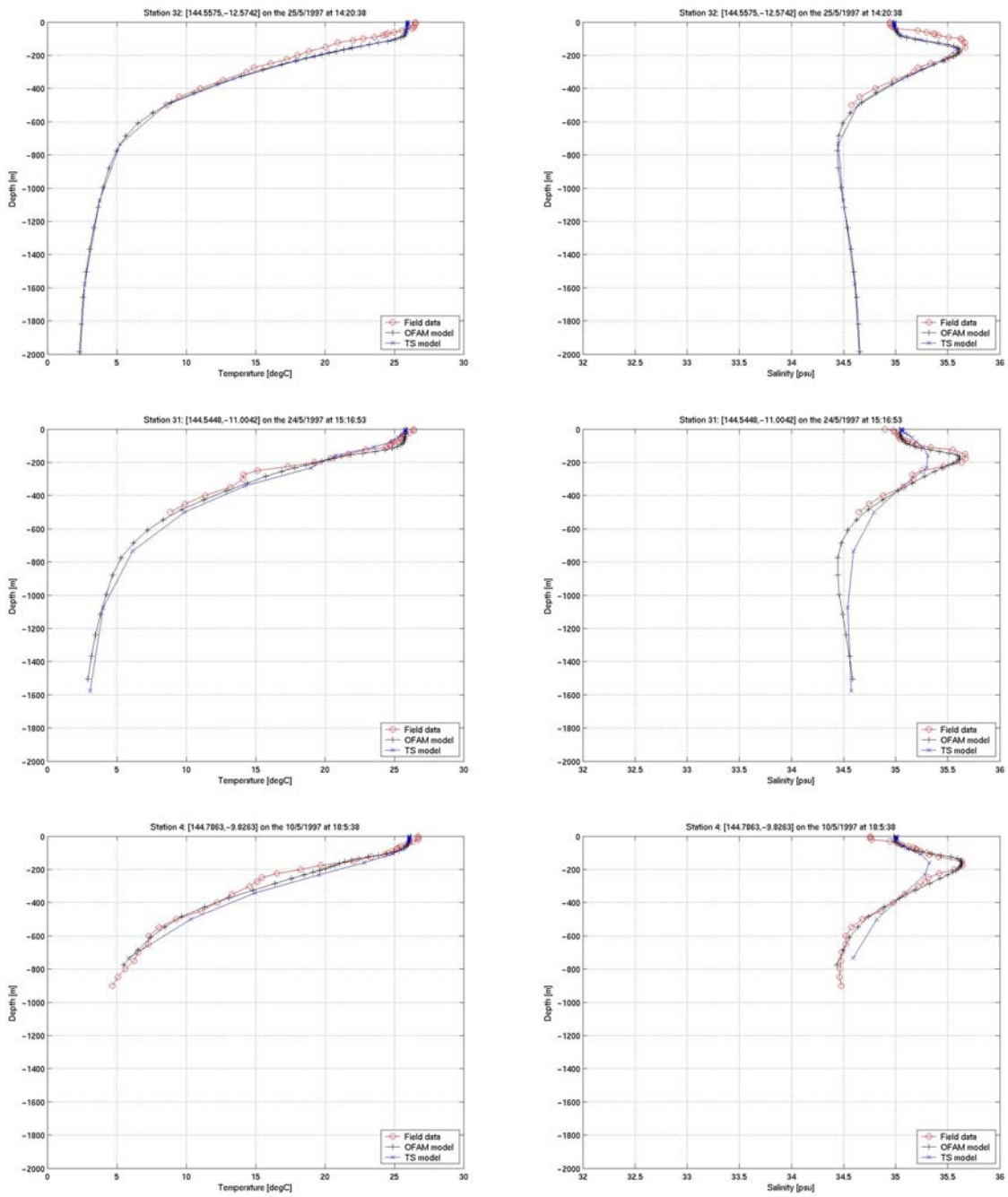

Figure 27: Examples of observed verses modelled temperature (left) and salinity (right) profiles taken in deep water to the east of the northern Great Barrier Reef during May 1997. OFAM global model (+) and Torres Strait regional model (*) outputs are compared with field data (o).

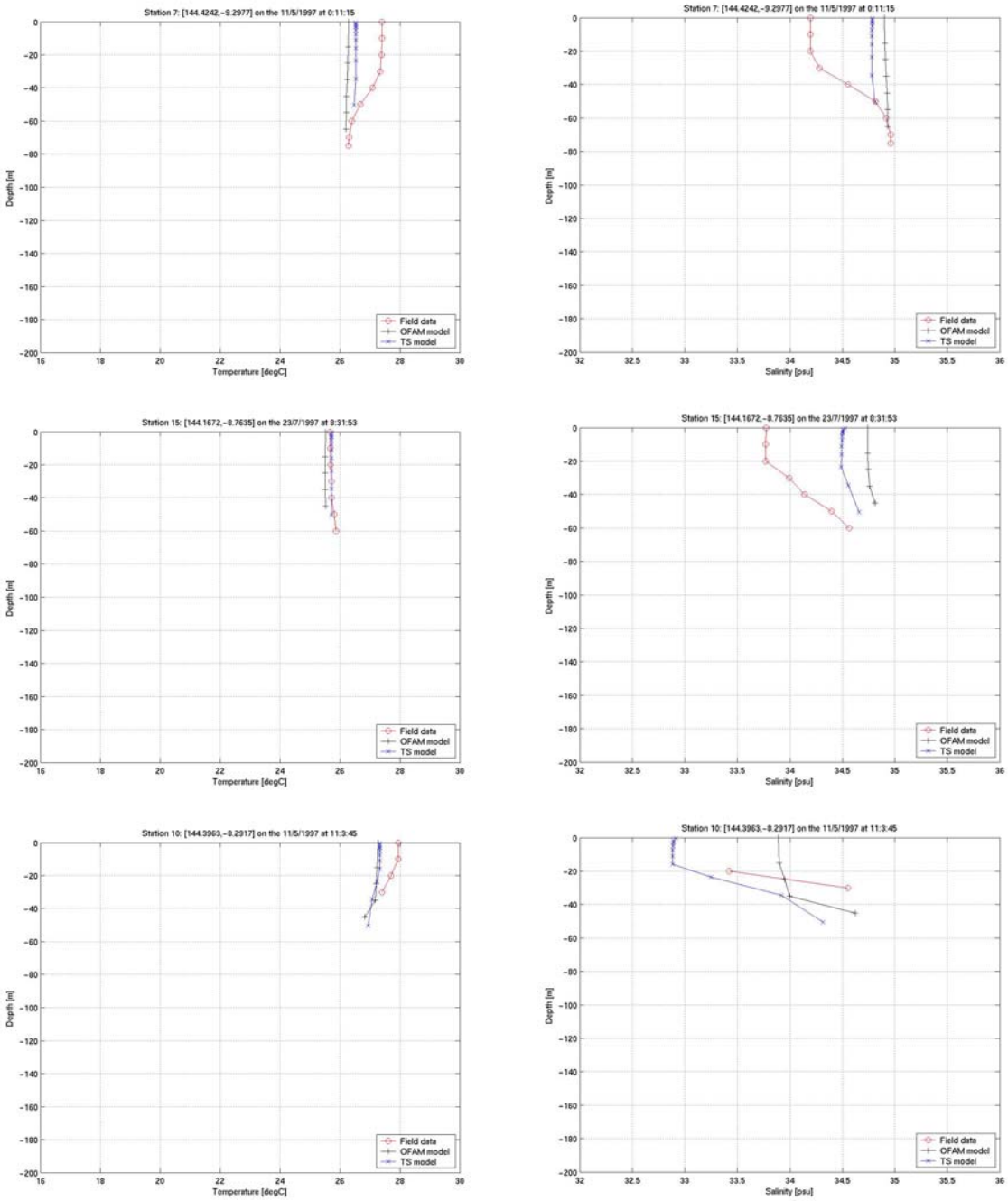

Figure 28: Examples of observed verses modelled temperature (left) and salinity (right) profiles taken on the shelf in the Gulf of Papua during May 1997. OFAM global model (+) and Torres Strait regional model (*) outputs are compared with field data (o).

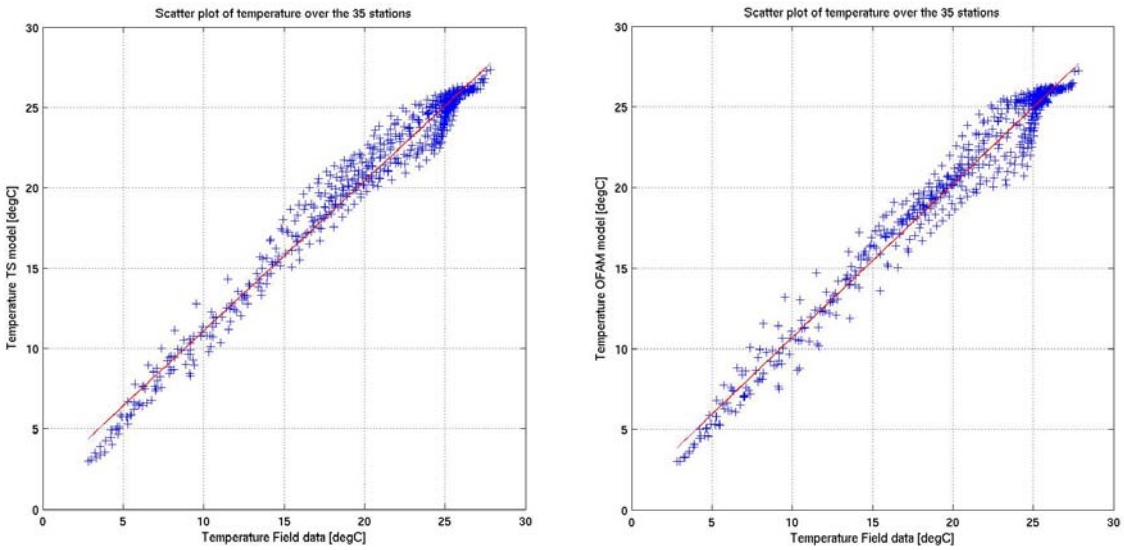

Figure 29: Scatter plot of Torres Strait model temperatures (left) and OFAM model temperatures (right) verses observed temperatures at the 35 stations. The linear regression slope (s) and correlation coefficient (r2) are: s=0.96 and r2=0.97 for the Torres Strait model and s=0.95 and r2=0.97 for the OFAM model.

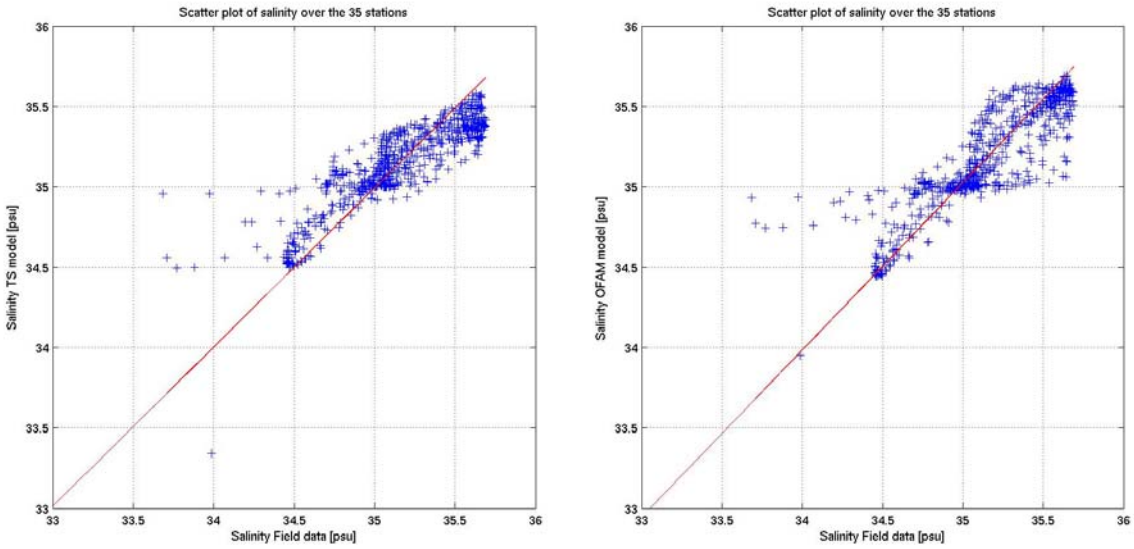

Figure 30: Scatter plot of Torres Strait model salinity (left) and OFAM model salinity (right) verses observed salinity at the 35 stations. The linear regression slope (s) and correlation coefficient (r2) are: s=0.99 and r2=0.98 for the Torres Strait model and s=1.04 and r2=0.98 for the OFAM model.

Table 6: Linear regression slope (s), offset (c) and correlation coefficient (r2) for modelled vs. observed (CARS data) temperature and salinity profiles. Temperature and salinity profiles displayed in Figure 27 and Figure 28 are marked by (*). (**) Stations offering less than three measurements along the profile were discarded. (+) Linear regression characteristics are based on all the data available.

	Modelled temperature						Modelled Salinity					
	TS model			OFAM model			TS model			OFAM model		
Station**	s	c	r2	s	c	r2	s	c	r2	s	c	r2
1	0.90	1.71	0.99	0.90	1.40	0.97	0.62	13.42	0.90	0.79	7.24	0.86
2	0.52	12.59	0.99	0.59	10.16	0.95	0.08	31.86	0.80	0.10	31.41	0.67
3	0.96	0.61	1.00	0.93	0.72	0.99	0.75	8.75	0.94	0.99	0.30	0.93
4*	0.93	2.41	0.97	0.97	1.08	0.98	0.57	15.04	0.95	0.99	0.42	0.97
5	0.47	13.59	0.96	0.66	8.57	0.95	0.36	22.63	0.83	0.67	11.78	0.77
6	0.18	21.27	0.98	0.18	21.36	0.95	0.07	32.40	0.94	0.12	30.74	0.96
7*	0.27	19.25	0.89	0.10	23.63	0.87	0.13	30.45	0.91	0.04	33.52	0.90
11	0.97	1.14	1.00	0.99	1.05	1.00	0.75	8.65	0.93	0.87	4.55	0.92
12	0.95	1.33	0.99	0.97	1.19	0.99	0.87	4.52	0.95	0.94	2.16	0.95
13	0.89	1.58	0.99	0.92	1.15	0.98	0.69	11.05	0.71	0.96	1.51	0.87
14	2.32	-34.17	0.97	2.41	-36.06	0.93	0.64	12.85	0.96	0.97	1.21	0.83
15*	-0.31	33.65	0.77	0.14	22.03	0.77	0.09	31.79	0.93	0.13	30.33	0.89
16	-2.04	78.24	0.69	-1.18	55.72	0.88	0.05	33.21	0.83	0.03	33.86	0.91
19	0.87	2.46	0.97	0.91	1.92	0.97	0.67	11.51	0.87	0.97	1.32	0.92
20	1.67	-17.27	0.91	0.49	12.90	0.71	0.44	19.65	0.87	0.34	23.07	0.63
21	0.94	1.18	0.61	0.15	21.57	0.78	1.06	-1.92	0.87	1.93	-32.38	0.94
22	0.84	4.31	0.99	0.93	2.19	0.94	0.80	6.97	0.97	0.90	3.48	0.87
23	0.93	1.04	0.99	0.97	0.54	0.99	0.76	8.31	0.82	1.01	-0.35	0.92
24	2.51	-38.66	0.90	2.07	-27.15	0.82	0.95	2.06	0.74	1.25	-8.45	0.60
25	0.92	2.58	0.99	0.93	2.60	0.98	0.62	13.41	0.88	0.67	11.55	0.76
26	0.96	1.30	0.99	1.02	0.03	0.98	0.66	11.90	0.94	0.92	2.72	0.90
27	0.87	3.68	0.99	0.89	3.46	0.90	0.56	15.42	0.93	0.69	10.70	0.70
28	0.94	0.93	0.99	0.97	0.53	0.99	0.81	6.59	0.89	1.04	-1.29	0.95
29	0.78	5.31	0.91	0.85	2.73	0.89	0.53	16.69	0.74	0.78	7.98	0.61
30	0.85	3.81	0.93	0.86	2.96	0.97	0.55	15.98	0.81	0.85	5.53	0.84
31*	0.85	3.50	0.98	0.96	1.37	0.99	0.40	20.97	0.84	0.82	6.31	0.93
32*	0.99	1.57	0.96	1.01	1.12	0.96	0.69	10.91	0.72	0.74	9.03	0.69
33	1.00	0.92	0.99	1.01	0.58	0.99	0.75	8.65	0.94	0.82	6.45	0.93
34	1.00	0.84	0.96	1.08	-1.32	0.97	0.79	7.25	0.89	1.02	-0.60	0.86
35	1.00	0.42	0.98	1.12	-2.63	0.98	0.75	8.90	0.96	1.00	0.08	0.88
Averaged	0.83	4.37	0.94	0.83	4.51	0.93	0.58	14.66	0.88	0.78	7.81	0.85
All+	0.93	1.71	0.98	0.95	1.18	0.97	0.99	0.43	0.98	1.04	-1.42	0.98

4.4 Comparison with observed currents

There have been few current meter data collected in Torres Strait over a number of decades, in response to the needs of shipping and mining industries, as well as marine conservation planning. These were compared with outputs from the Torres Strait model. The period of the comparisons was limited to 1997-2004, when both current meter data and model outputs were available. Comparisons have focused on Acoustic Doppler Current Profiler (ADCP) data collected around Turnagain Island during the Torres Strait marine surveys S266 and S277 (Heap et al. 2005; Daniell et al. 2006). Qualitative comparisons have also been made with low-frequency currents derived from long term observations by Wolanski (1988). Complementary Recording Current Meter (RCM) observations collected in 1988, 1989, 1990 and 1993 were not used, as they may contain significant errors due to biofouling (Harris,

1993) and would have required extending the model beyond the available forcing fields period.

4.4.1 Tidal currents

The principal component of the tidal current (i.e. eastward) was in very good agreement with data (Figure 31 and Figure 32). With an average regression coefficient of s=0.99 and correlation coefficient of r2=0.70, the model explained more than 75% of the variability (Table 4). The secondary component (i.e. northward) was significantly weaker and correlations were lower, with an average regression coefficient of s=0.49 and correlation coefficient of r2=0.23. The current magnitude was reasonably modelled with an average regression coefficient of s=0.64 and correlation coefficient of r2=0.27 (Figure 31, Figure 32 and Table 4). At Stations 1 and 4, current magnitudes tended to be overestimated due to a stronger than observed eastward contribution, while at Station 2 they tended to be underestimated due to a weaker than observed northward component.

Discrepancies in tidal currents may be attributed to both the model set up and fieldwork set up. Current meters were deployed relatively close to Turnagain Island on a massive sandwave rising up to 6m from a maximum water depth 10m depth. The island constituted a significant flow obstacle and may trigger eddies in its wake. Compared to these features the model was relatively coarse and not able to capture the detailed boundary layer circulation around the island. Similarly, the model resolution was not designed to represent the local effect of sandwaves, which are known to channel tidal currents.

4.4.2 Sub-tidal frequency currents

Unfortunately no long-term current meter records were available within the period that the model was run. However, the seasonal trends evident in data collected in prior years (Figure 33, Wolanski et al., 1988), such as persistent eastward currents of around 0.1 m s^{-1} over a 60-day period during the monsoon, appear to be well represented by the model (details will be discussed in Section 5.4).

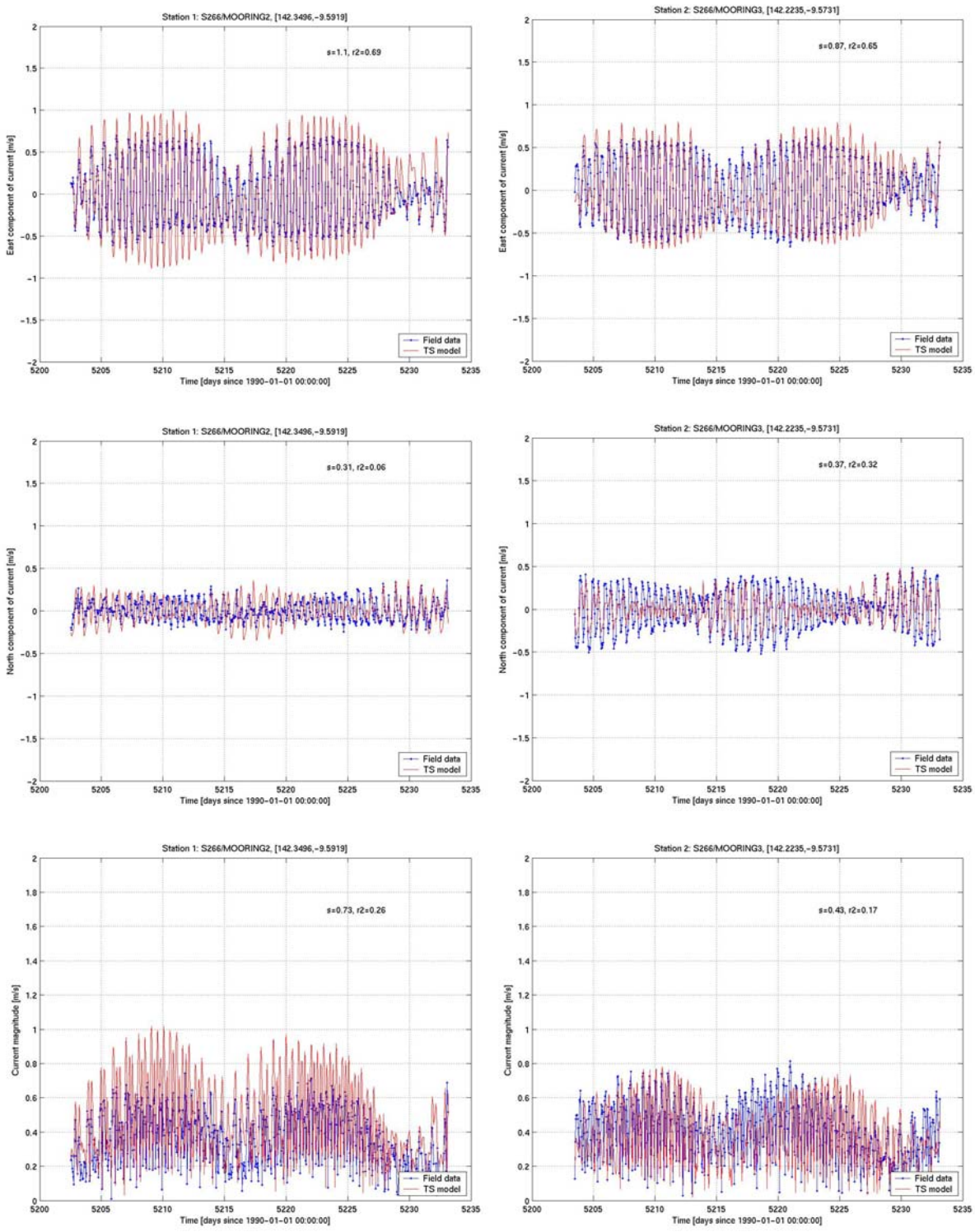

Figure 31: Comparison between modelled and observed currents at 1.6 m above the bed at station S266/cm2 (right), S266/cm3 (left): east component (top), north component (middle) and magnitude (bottom).

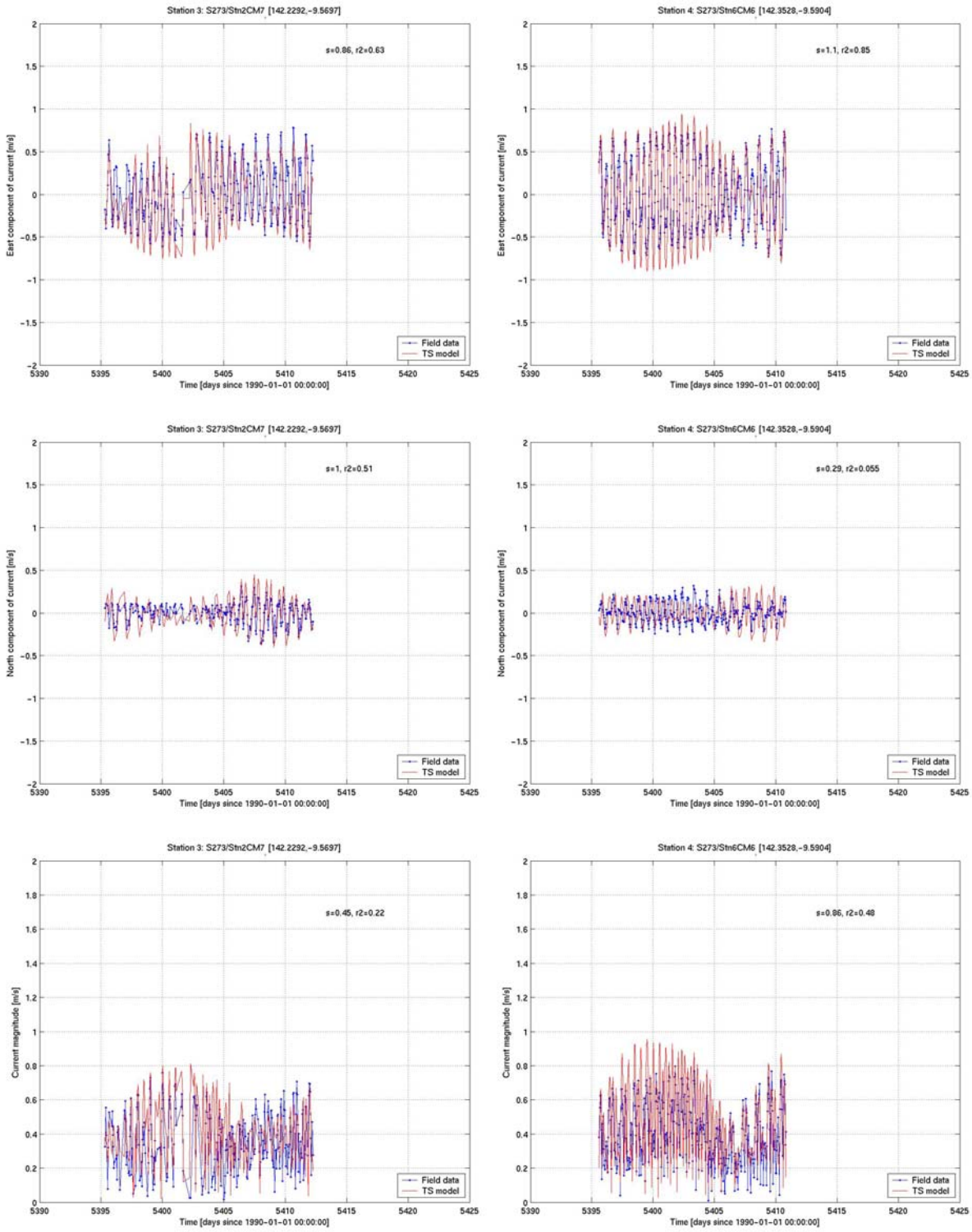

Figure 32: Comparison between modelled and observed currents at 1.6 m above the bed at station S273/cm7 (right) and S273/cm6 (left): east component (top), north component (middle) and magnitude (bottom).

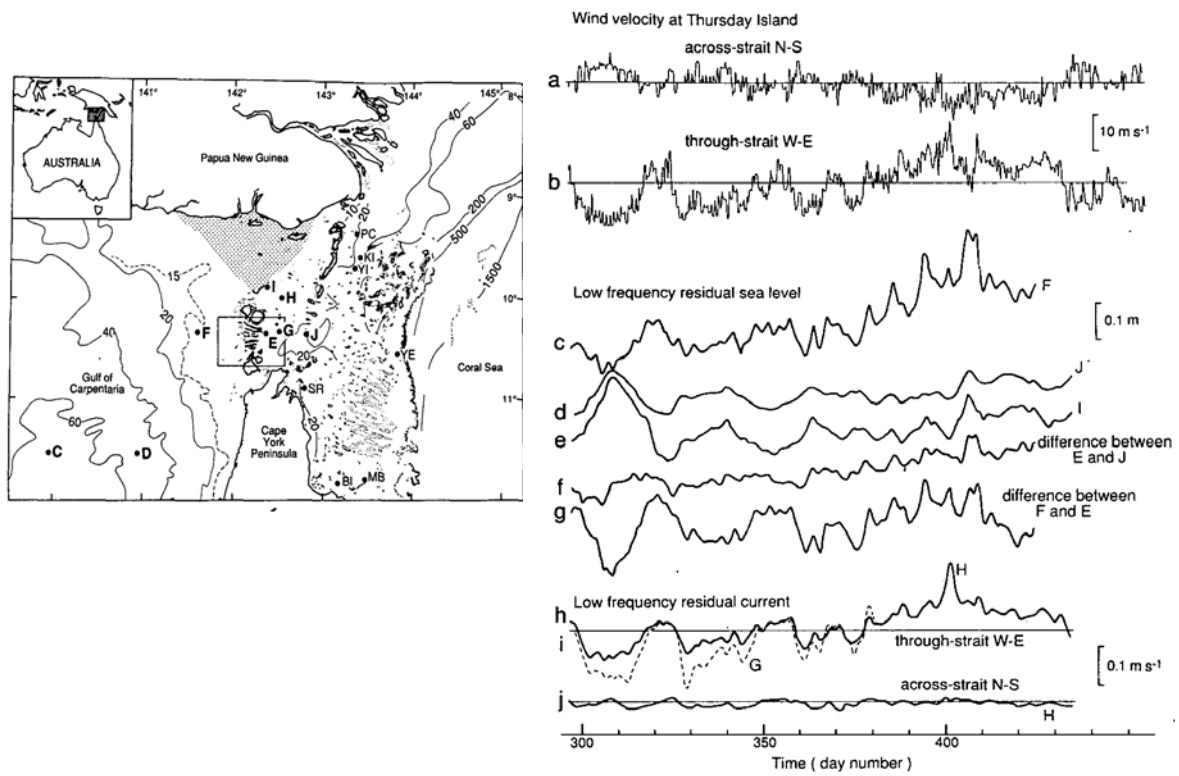

Figure 33: Time series plots of (a) northward and (b) eastward wind speed at Thursday Island; (c-g) quantities derived from low frequency sealevel data; (h-i) low-frequency eastward currents at sites H and G; and (j) low-frequency northward currents at site H. Time is expressed in day number from 01/01/1986, so that the plot shows October 1986 to March 1987 (reproduced from Wolanski et al. 1988, figure 6).

5 Description of the circulation fields

Description of the model circulation fields will begin with the highly non-linear diurnal and semi-diurnal tide, which usually dominates the instantaneous flow patterns in Torres Strait. However, transport and dispersion over longer timescales of days to months were largely determined by seasonal patterns, which are described here in terms of monthly averaged fields. The flow in Torres Strait also varied on interannual timescales and is considered here in terms of monthly mean anomalies derived from simulation outputs covering the period 1997-2005.

5.1 Tides

5.1.1 Sea level

The interaction of diurnal and semi-diurnal tides contributes to the complexity and strength of currents in Torres Strait. The amplitude and phase of the tide change rapidly through the strait. This change occurs in the shallow and constricted centerline of the strait, which stretches between the northernmost tip of Cape York and the southernmost tip of Papua New Guinea. A set of sealevel time series taken every 0.5 degree along a 10°S were compared (Figure 34). Results show that signals from adjacent sites were strongly correlated on both the western (Figure 35) and eastern (Figure 36) side of the strait. However, adjacent sites either side of the shallowest part of the strait (KM60 and KM120) showed low correlation (Figure 37).

The weak correlation of tidal signals through Torres Strait indicates that the tidal dynamics result from the intersection of two separate and dissimilar tidal regimes propagating in from the Coral and Arafura Seas. Tides in the Gulf of Carpentaria were strongly diurnal with a comparable contribution from tidal constituents O1 and K1, while Coral Sea tides were semidiurnal, being dominated by the M2 and S2 constituents. A significant transfer of energy between tidal wave frequencies occurred in the strait (Figure 38 and Table 7), with only about 20% of the tidal wave transmitted through Torres Strait (Table 8). This result refines the estimation of 30% by Wolanski et al. (1988) based on a simplified waveguide model.

The tidal range varied significantly throughout the Torres Strait region, ranging from 1.5m to nearly 6m in the Gulf of Carpentaria and from 3m to nearly 7m in the Coral Sea and Gulf of Papua (Figure 39a). While the tidal range tended to increase as the water depth decreased, a threshold seemed to be reached within Torres Strait at around 4m. This threshold clearly appears in the tidal range profile along 10°S between 142°E and 143°E (Figure 39b) and corresponds to where the out-of-phase tidal signals from the west and east meet.

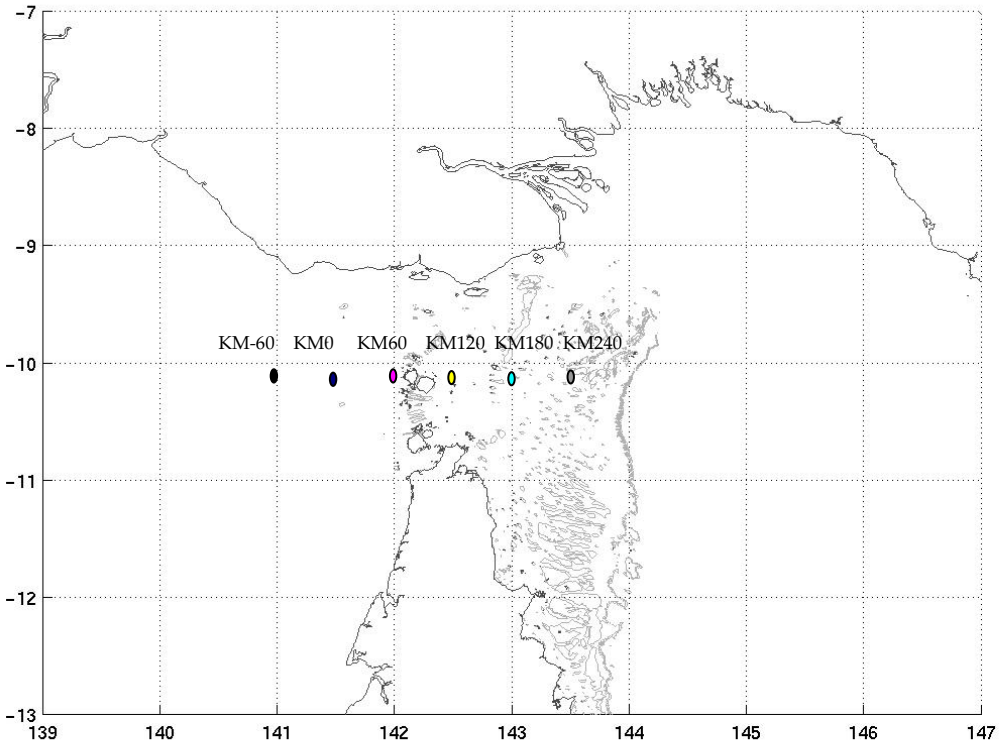

Figure 34: Location of six virtual stations along the Torres Strait.

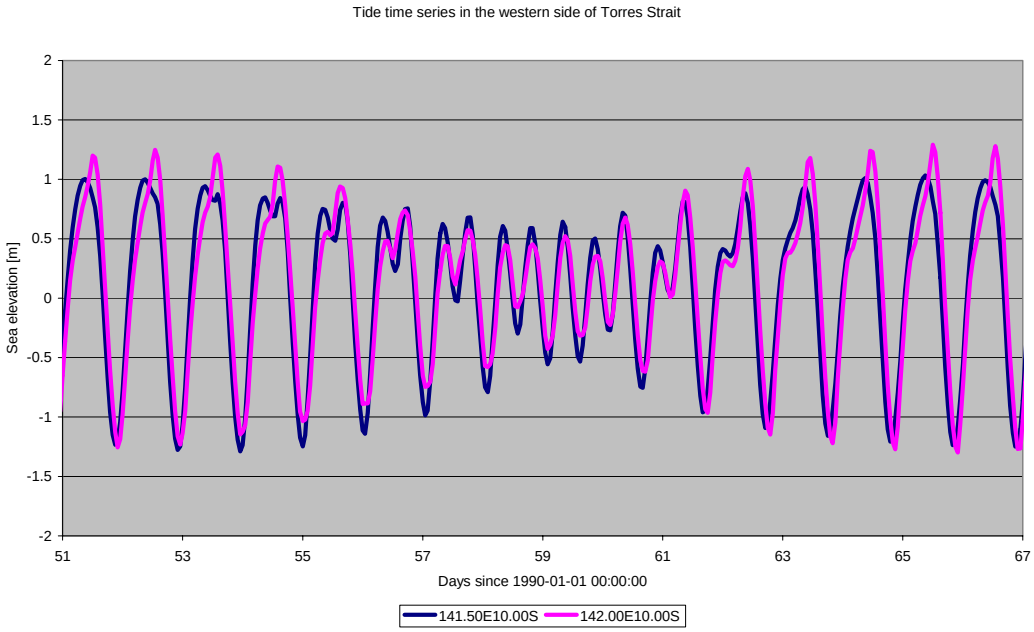

Figure 35: Strongly correlated (r2=0.86, s=0.90) tidal signals on the western side of the Torres Strait between 141.50E 10S and 142.00E 10S.

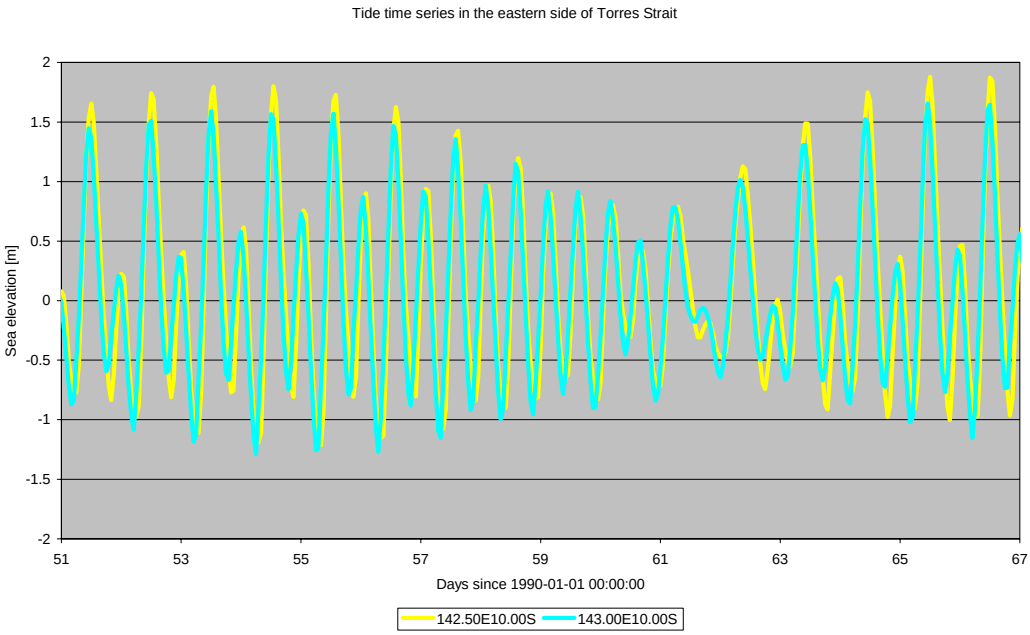

Figure 36: Well-correlated (r2=0.82, s=0.83) tidal signals on the eastern side of the Torres Strait between the two locations: 142.50E 10S and 143.00E 10S.

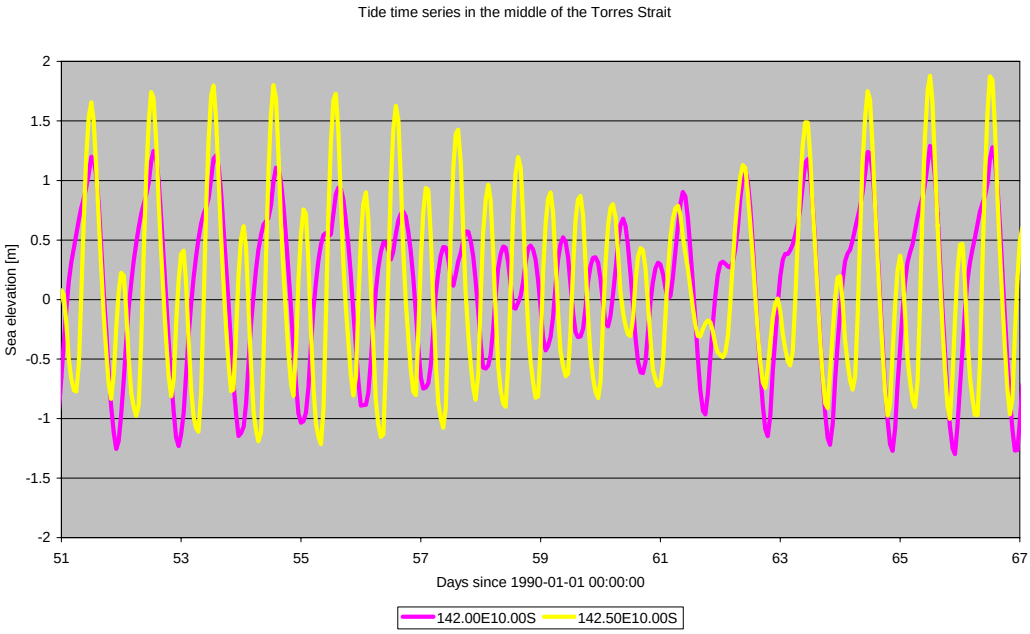

Figure 37: Poorly correlated (r2=0.13, s=0.42) tidal signals on the middle of the Torres Strait between the two locations: 142.00E 10S and 142.50E 10S.

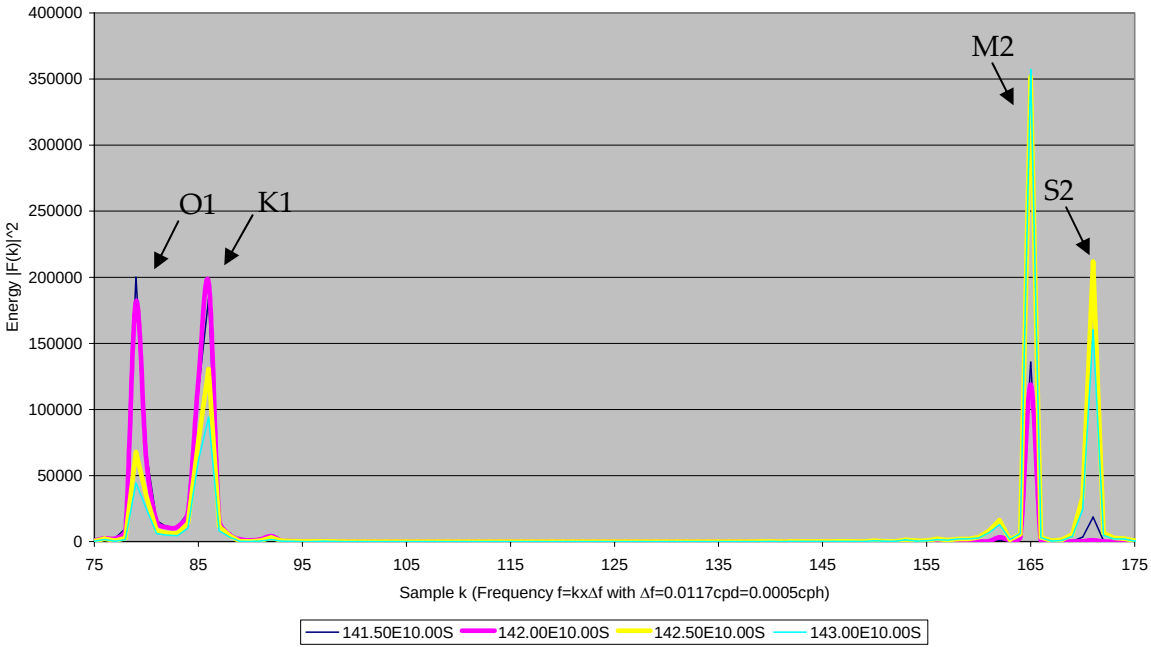

Figure 38: Power spectral density of sea level along the Torres Strait; 90% of the tidal energy is within this range of frequencies.

Table 7: Tidal harmonic constituents

Description of tidal component	Name	Frequency [10-5 Hz]	Period [h]
Principal lunar diurnal	O1	1.07	25.82
Luni-solar diurnal	K1	1.16	23.93
Principal lunar semi-diurnal	M2	2.23	12.42
Principal solar semi-diurnal	S2	2.31	12.00

Table 8: Characteristics of sea level at six virtual stations along the Torres Strait

Name of the virtual station	KM-60	KM0	KM60	KM120	KM180	KM240
Location on model grid (I,j)	(19, 22)	(20,28)	(21,34)	(22,40)	(23,46)	(23,51)
Latitude 10.00S ; Longitude (E)	141.00	141.50	142.00	142.50	143.00	143.50
Water depth [m]	31.83	14.04	7.73	10.79	14.68	24.58
Ratio of constituent O1+K1+M2+S2 and local tide energy	0.71	0.89	0.88	0.88	0.90	0.81
Ratio of constituent O1 and local tide energy	0.29	0.33	0.31	0.10	0.08	0.04
Ratio of constituent K1 and local tide energy	0.31	0.37	0.41	0.20	0.19	0.14
Ratio of constituent M2 and local tide energy	0.09	0.17	0.15	0.34	0.42	0.42
Ratio of constituent S2 and local tide energy	0.03	0.03	0.00	0.24	0.22	0.20
Ratio of local tide energy and its average over the six stations	0.95	0.95	0.91	1.20	0.99	0.99

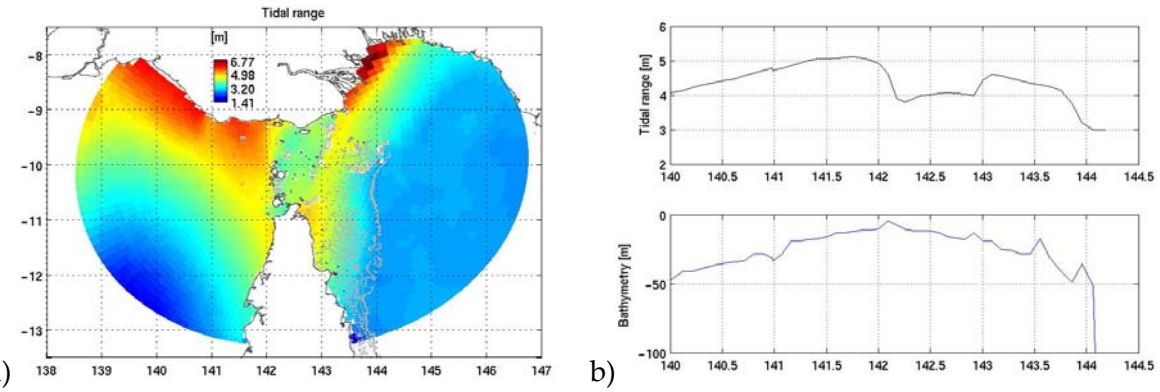

Figure 39: (a) Model tidal range and (b) tidal range profile (top) and corresponding bathymetry (bottom) along 10°S.

5.1.2 Currents

The model currents were mainly orientated east-west through Torres Strait (Figure 40 & Figure 41). However, near the major channels, currents were constrained parallel to surrounding reefs and islands and were significantly reduced near large reefs, such as Warrior Reefs. East of Torres Strait in the Gulf of Papua and Great Barrier Reef, currents were mainly orientated in the cross-shelf direction, re-orientating towards the strait on approaching Cape York. To the east, in the Gulf of Carpentaria, currents followed the tidal signal in a clockwise rotation. This pattern was similar during both spring tides (Figure 40) and neap tides (Figure 41).

Depth averaged currents strength usually peaked where the flow was increasingly influenced by the local bathymetry and coastline geometry. Currents tended to accelerate around reefs and islands and in narrow passages and also in shallow water. In particular, peak speeds were in the range of 1.5 - 3.0 m s^{-1} around Cape York, in the Endeavour Strait and Adolphus Channel, in the channels to the south and to the north of Badu and Mona Islands, and in the passage through Warrior Reef. More moderate currents in the range of 0.5 - 1.5 m s^{-1} occurred in the northwest and southeast of Torres Strait, where currents strength gradually increased as water depth decreased. Weaker currents in the range 0 - 0.5 m s^{-1} were found in the wake of large flow obstacles such as Warrior Reef and Auwamaza Reef in the northeast of Torres Strait and the larger southwestern islands such as Badu, Moa, Horn and Prince of Wales (Figure 42).

In shallow water, including the Great Barrier Reef, Torres Strait and the Gulf of Carpentaria, the maximum surface layer flow is oriented to the west following the Trade winds direction. Maximum surface currents displayed the same pattern as the maximum depth averaged currents described above, but with currents speeds around 30% greater. In the Coral Sea and Gulf of Papua, the maximum surface layer flow indicated the presence of a large clockwise ocean circulation corresponding to the so-called Hiri Current and Gyre (Figure 42).

The shear in the water column generated by the tidal motions over shallow bathymetry resulted in strong vertical mixing. This mixing extended over the entire water column in Torres Strait and in the Gulf of Carpentaria all year round. In the Gulf of Papua, the offshore

extent of well mixed waters varied significantly with the season, withdrawing inside the 30 m isobath during the monsoon (not shown).

The dissipation of current energy near the seabed was significant in waters less than 30 m deep, with bottom stresses varying both temporally and spatially in response to tidal currents strength and wave height and period. Combined wave-current bottom friction was particularly high along the coast of Papua New Guinea and in North West Torres Strait (Figure 43). Maximum friction velocities due to combined wave-current were in the range 0.1 - 0.3 m s^{-1}, usually peaking to the west of major islands and reefs. The bottom stresses induced by the combination of waves and currents were an order of magnitude larger than those induced by currents alone. These distributions have important implications for resuspension and transport of sediments (Margvelashvili and Saint-Cast 2006) and possibly the distribution of benthic species.

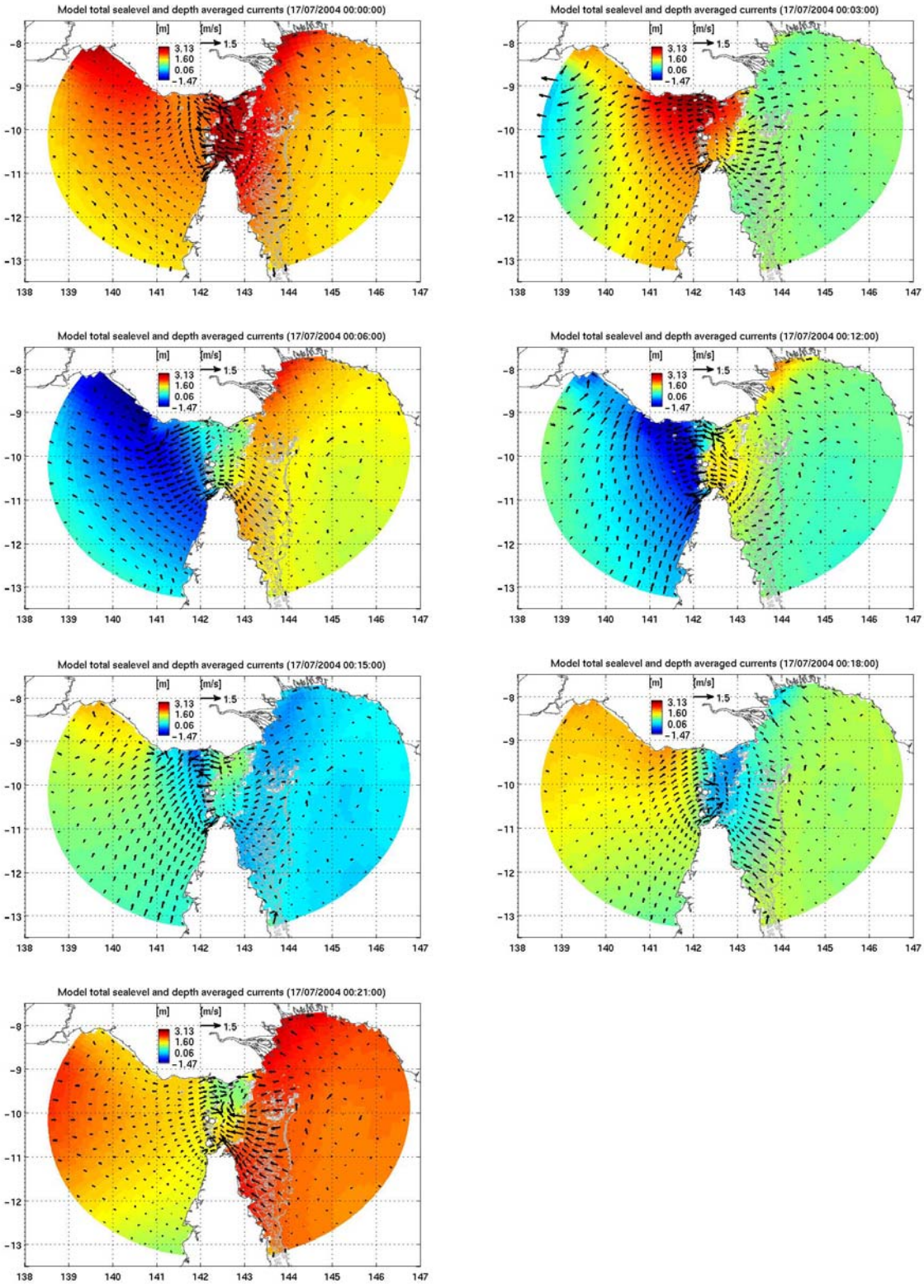

Figure 40: Depth averaged current vectors overlain on sealevel close to neap tide at three hour intervals.

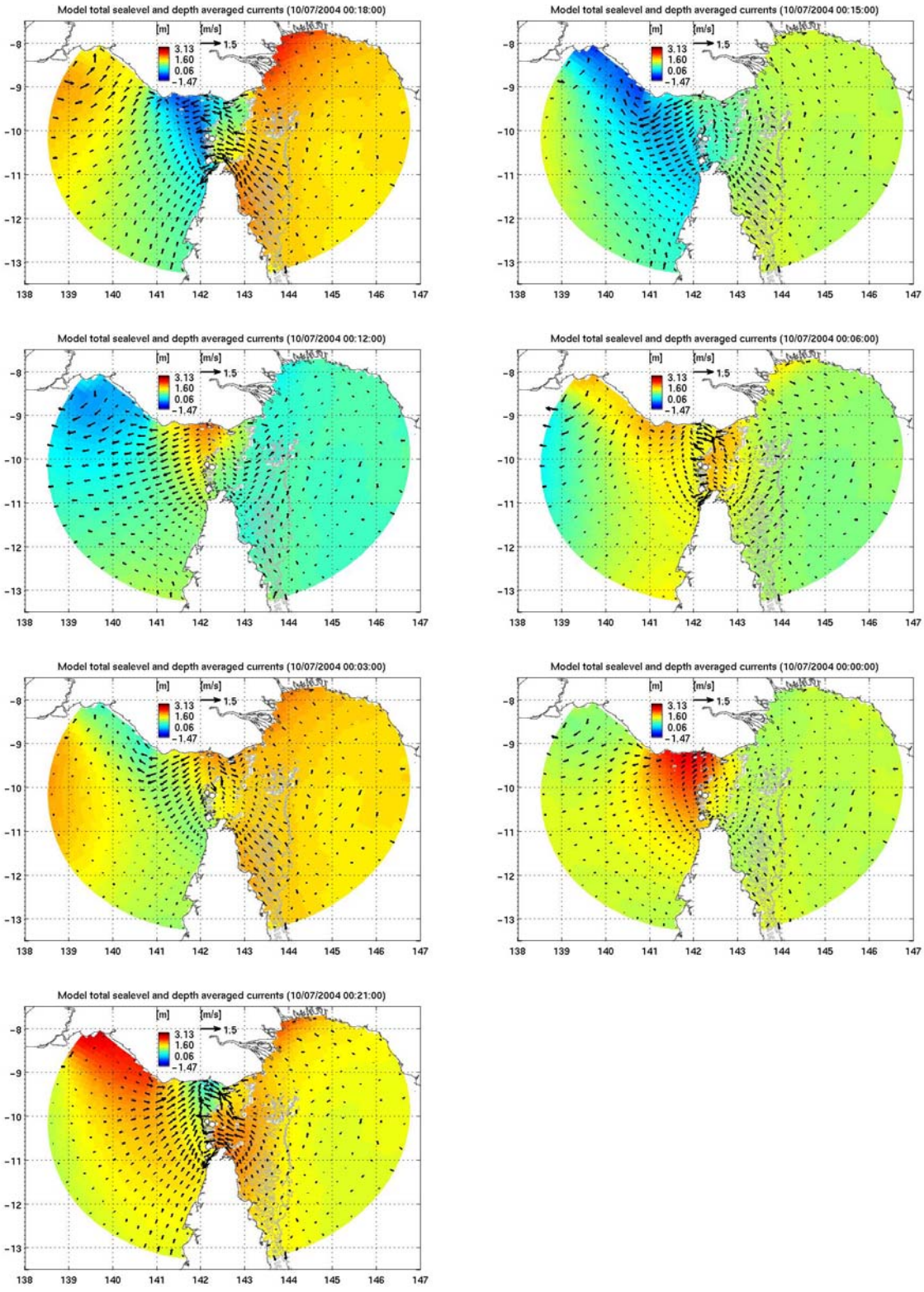

Figure 41: Depth averaged current vectors overlain on sealevel close to neap tide at three hour intervals.

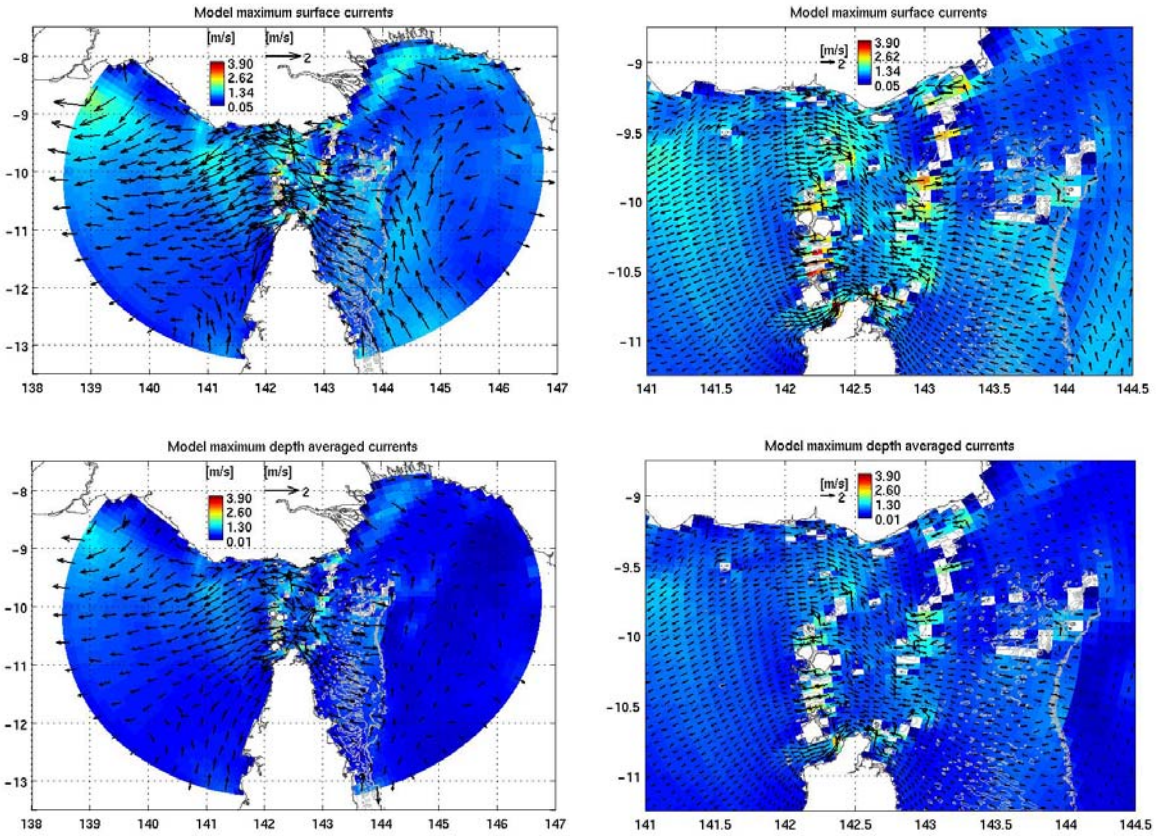

Figure 42: Maximum surface current (0.5m depth) (top) and maximum depth averaged current (bottom) as indicated by the 99th percentile. Current vectors are overlain on current magnitude. While maximum currents tended to occur when winds were aligned with the spring-tidal currents, the dominance of the tidal component ensured that there was little seasonal variation in these statistics.

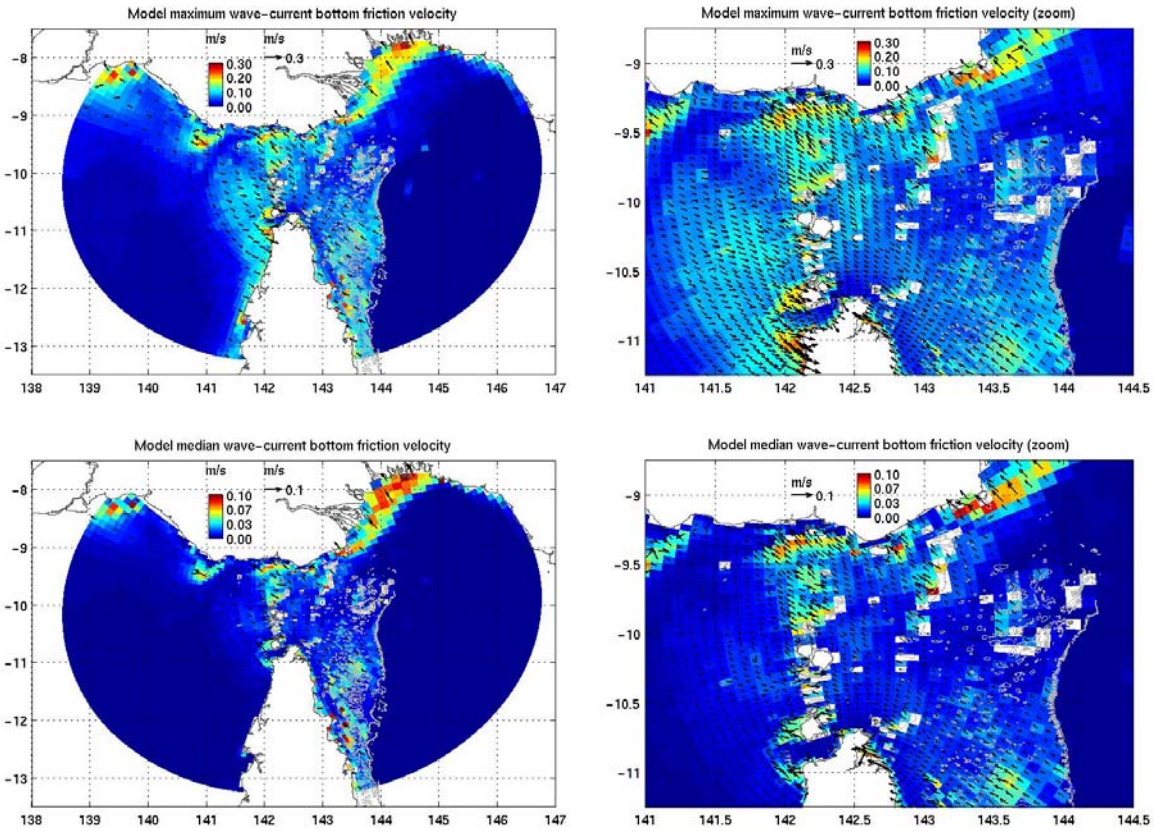

Figure 43: Maximum (top) and mean (bottom) bottom friction velocity induced by combined waves and currents as indicated by the 99th and 50th percentile respectively. Bottom waves-current friction velocity is given by the square root of the wave-current bottom stress and water density (1021 kg/m^3) ratio. Bottom friction velocity vectors are overlain on the magnitude.

5.2 Seasonal Patterns

Mean flows determine long-term transport patterns, but in Torres Strait they tend to be masked by the large tidal currents. Monthly mean currents have therefore been computed by averaging hourly output fields over 8 years for each month of the year. Similarly, monthly bottom friction velocities have been derived, including the influence of combined waves and currents.

In general terms, the mean circulation in Torres Strait showed a significant westward drift developing over the trade winds season, which then weakened and reversed over the monsoon season (Figure 48 and Figure 49). This flow was strongly connected to the Great Barrier Reef waters, but showed little connectivity with the coastal circulation in the Gulf of Papua. During the Trades, the coastal circulation in the Gulf of Papua was very weak, but strengthened and re-orientated towards the southeast along the coast of Papua New Guinea during the monsoon. Bottom friction was significantly enhanced by waves in shallow Torres Strait over the trades (Figure 54 and Figure 55).

5.2.1 Surface currents

Monthly mean surface currents were predominantly driven by the prevailing winds, although the large scale ocean circulation also contributed to the surface flow in deep water. During the Trade season, a strong northward current developed seaward of the Great Barrier

Reef with surface currents in the range of 0.5 - 0.9 m s^{-1} (Figure 44 and Figure 45). This flow faded away during the Monsoon season, with surface currents falling below 0.3 m s^{-1}. However, the Monsoon drives a significant eastward current in the Gulf of Papua peaking at around 0.6 m s^{-1}. Despite the spatial separation and seasonal lag in the development of these two currents off the Great Barrier Reef and Gulf of Papua, they both contribute to the mean clockwise current pattern in this region usually referred to as the Hiri Current or Gyre.

Within Torres Strait, the seasonal surface flow was predominantly to the west and northwest during the trades. Surface speeds were generally in the range 0.2 -0.3 m s^{-1}, but could exceed 0.6 m s^{-1} through narrow channels and fall almost to zero in the wake of large islands and reefs such as Warrior Reef. During the monsoon, surface currents were predominantly towards the east and southeast, with speeds typically less than half those produced under the Trade winds (Figure 46 and Figure 47).

5.2.2 Depth-averaged currents

The depth-averaged current strength was about 30% weaker than the surface current (Figure 48 and Figure 49). During the trades, a northwestward flow through the Great Barrier Reef fed a westward mean flow around 0.1 - 0.3 m s^{-1} through Torres Strait (Figure 50 and Figure 51). These trends gradually reversed as the monsoon developed, although the flow was again much weaker than under Trade wind conditions. These circulation patterns showed significant exchange between the Torres Strait and the northern Great Barrier Reef, but very little direct connectivity with the Gulf of Papua.

5.2.3 Bottom friction induced by waves and currents

Like the currents, monthly mean wave-current bottom friction velocities during the Trades were typically double those in the Monsoon, implying a four fold difference in bottom stress (Figure 52 and Figure 53). A notable exception to these trends was the coastal region from southwestern Torres Strait along the west coast of Cape York, where bottom friction velocities were higher during the Monsoon than the Trades (Figure 54 and Figure 55). This can be attributed the longer fetch and therefore larger waves experienced in this region under Monsoon conditions (rather than local currents which are actually weaker during the Monsoon). The highest bottom stresses in the region occurred in the Gulf of Papua, parts of the Great Barrier Reef, and northwestern Torres Strait, where bottom friction velocities exceeded 0.1 m s^{-1}.

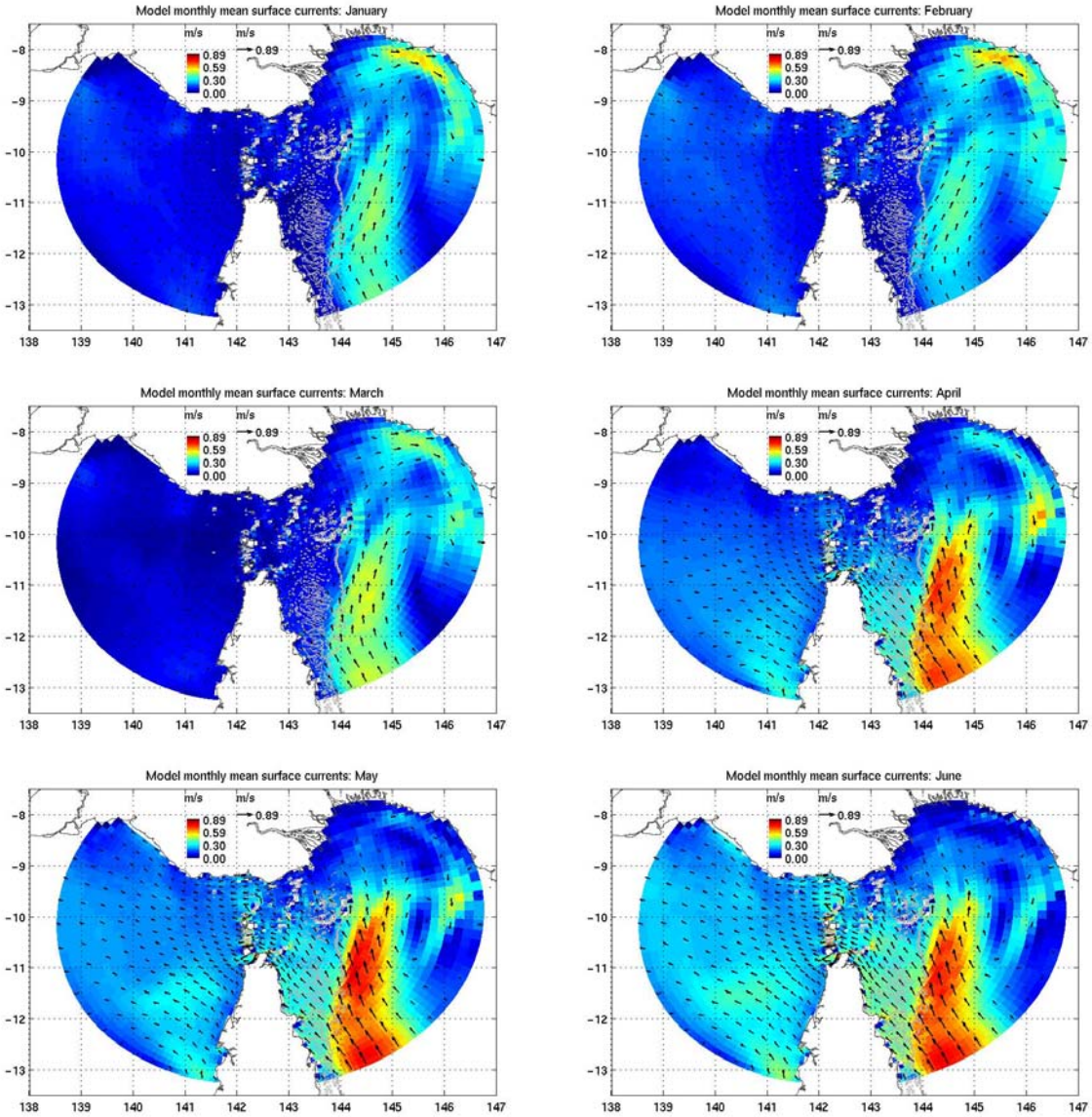

Figure 44: Monthly mean surface currents based on eight years of model runs covering the period 1997-2004 (January to June).

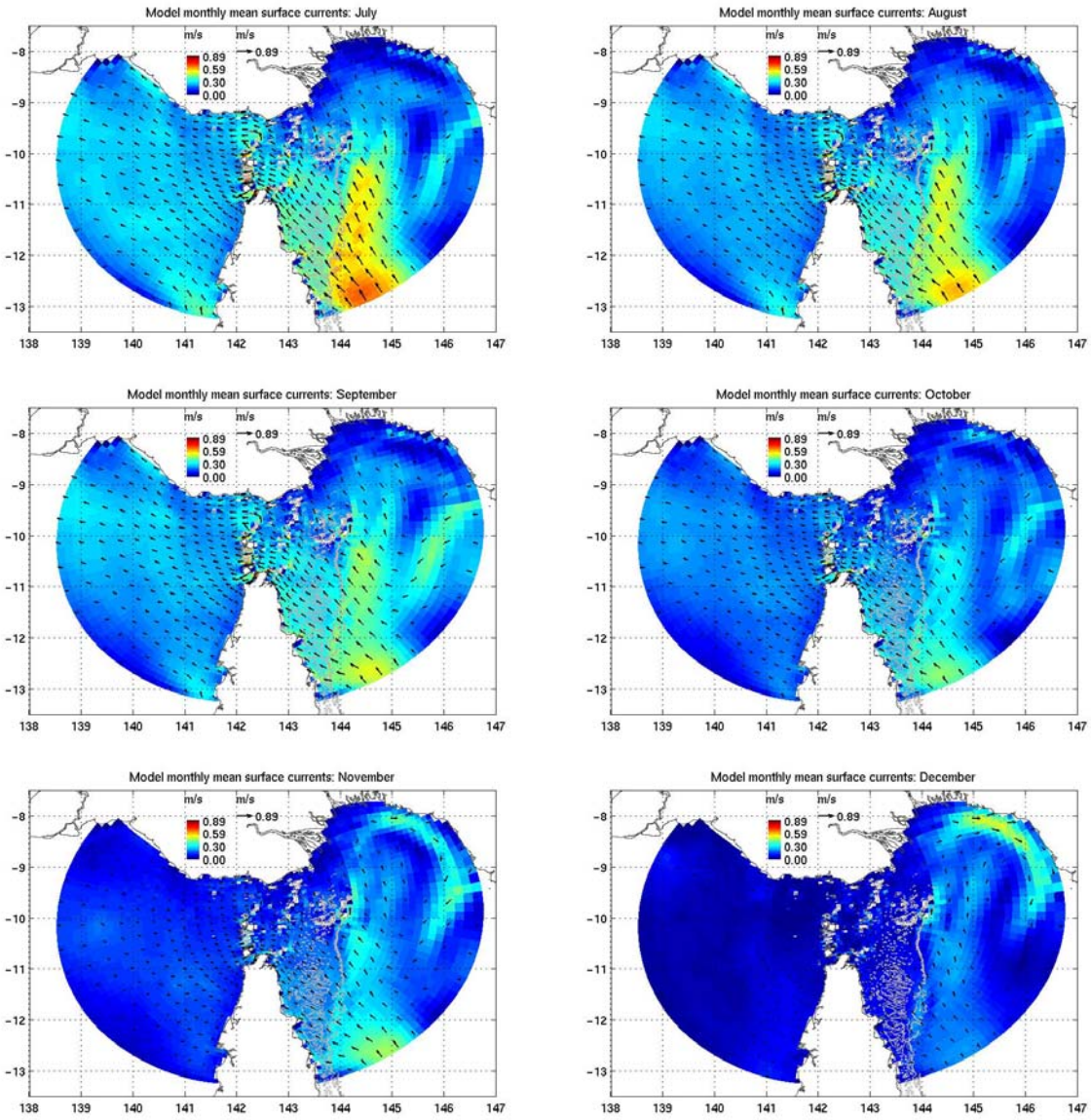

Figure 45: Monthly mean surface currents based on eight years of model runs covering the period 1997-2004 (July to December).

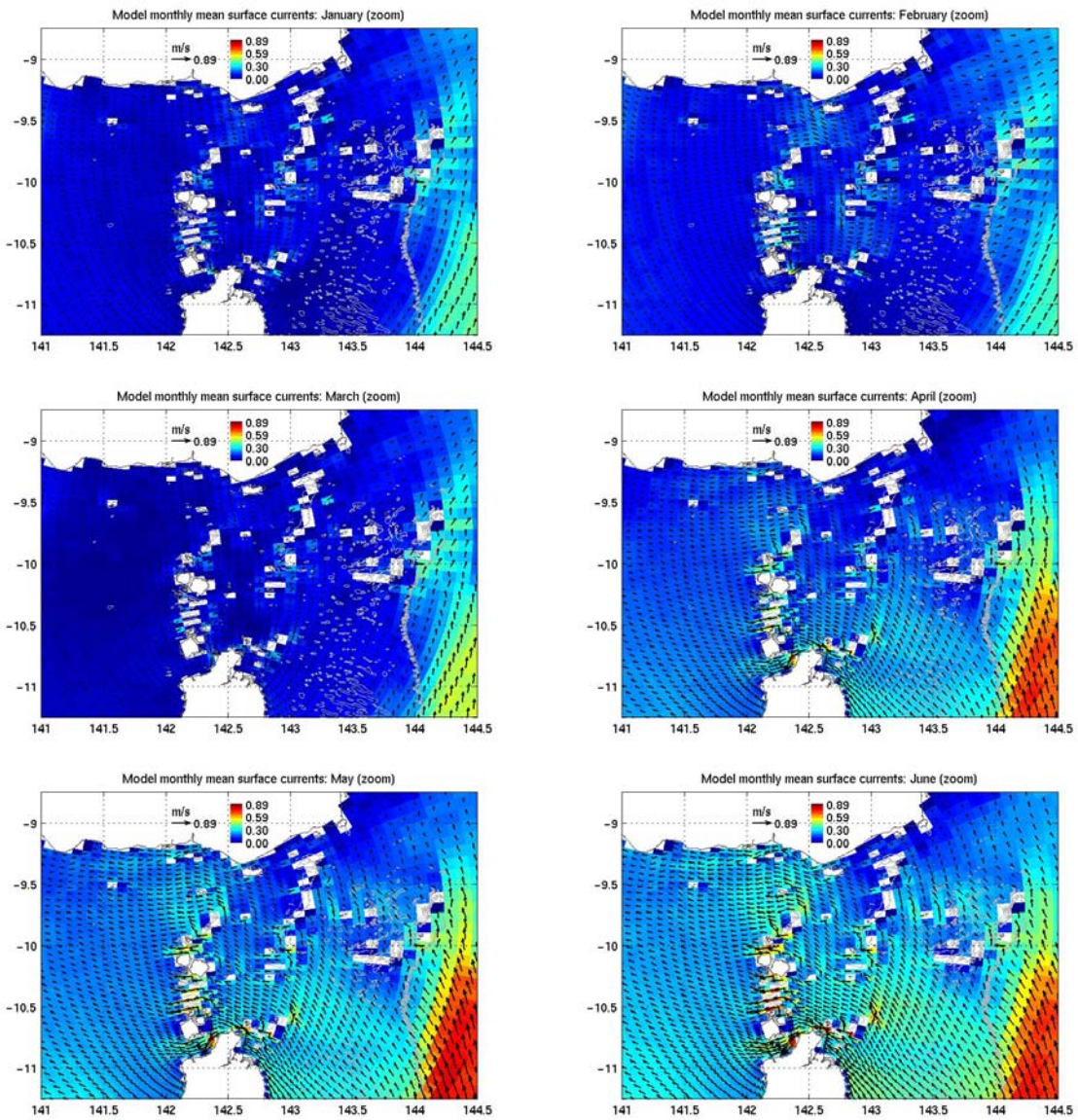

Figure 46: Monthly mean surface currents based on eight years of model runs covering the period 1997-2004 (Torres Strait enlargement, January to June).

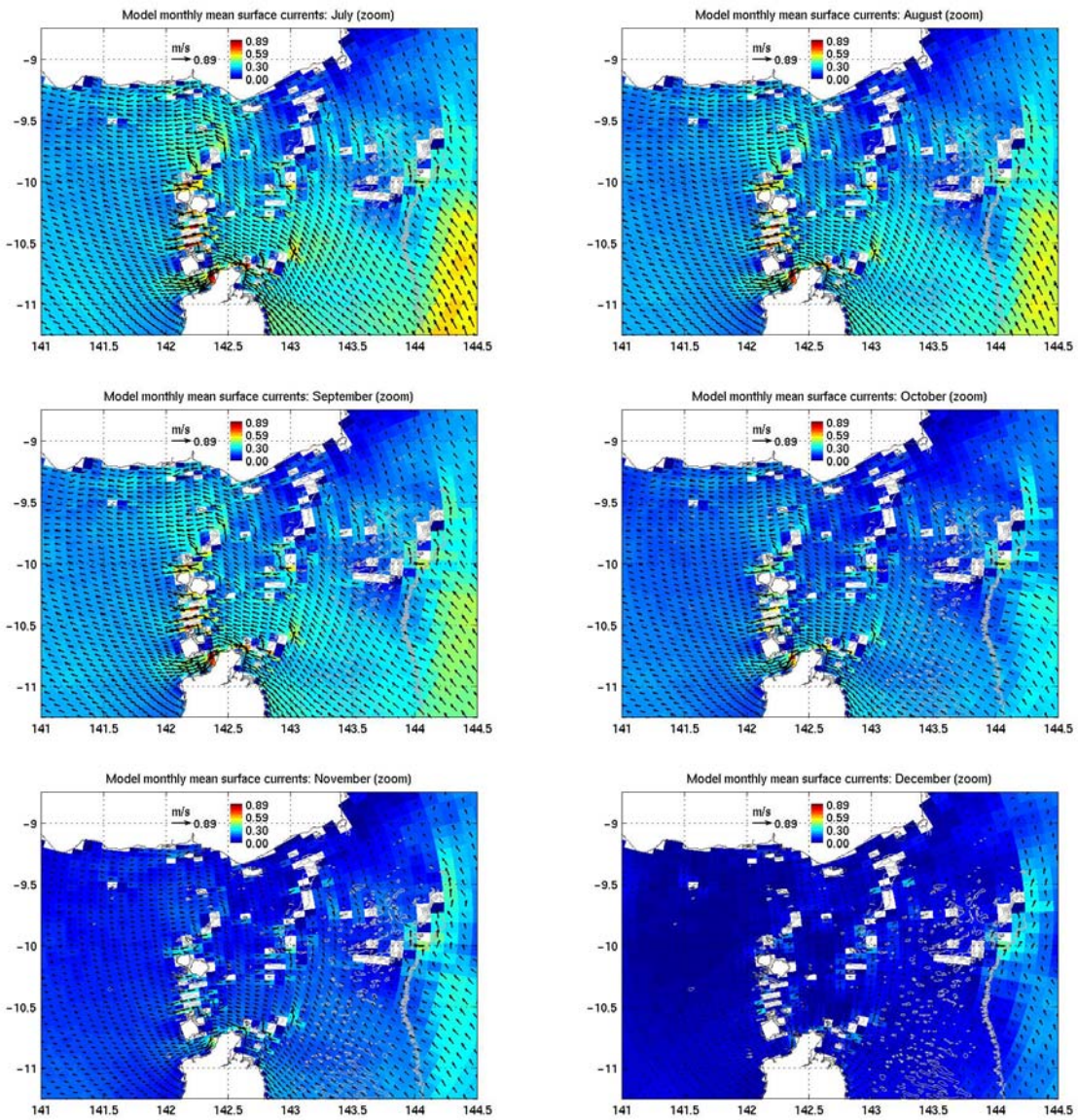

Figure 47: Monthly mean surface currents based on eight years of model runs covering the period 1997-2004 (Torres Strait enlargement, July to December).

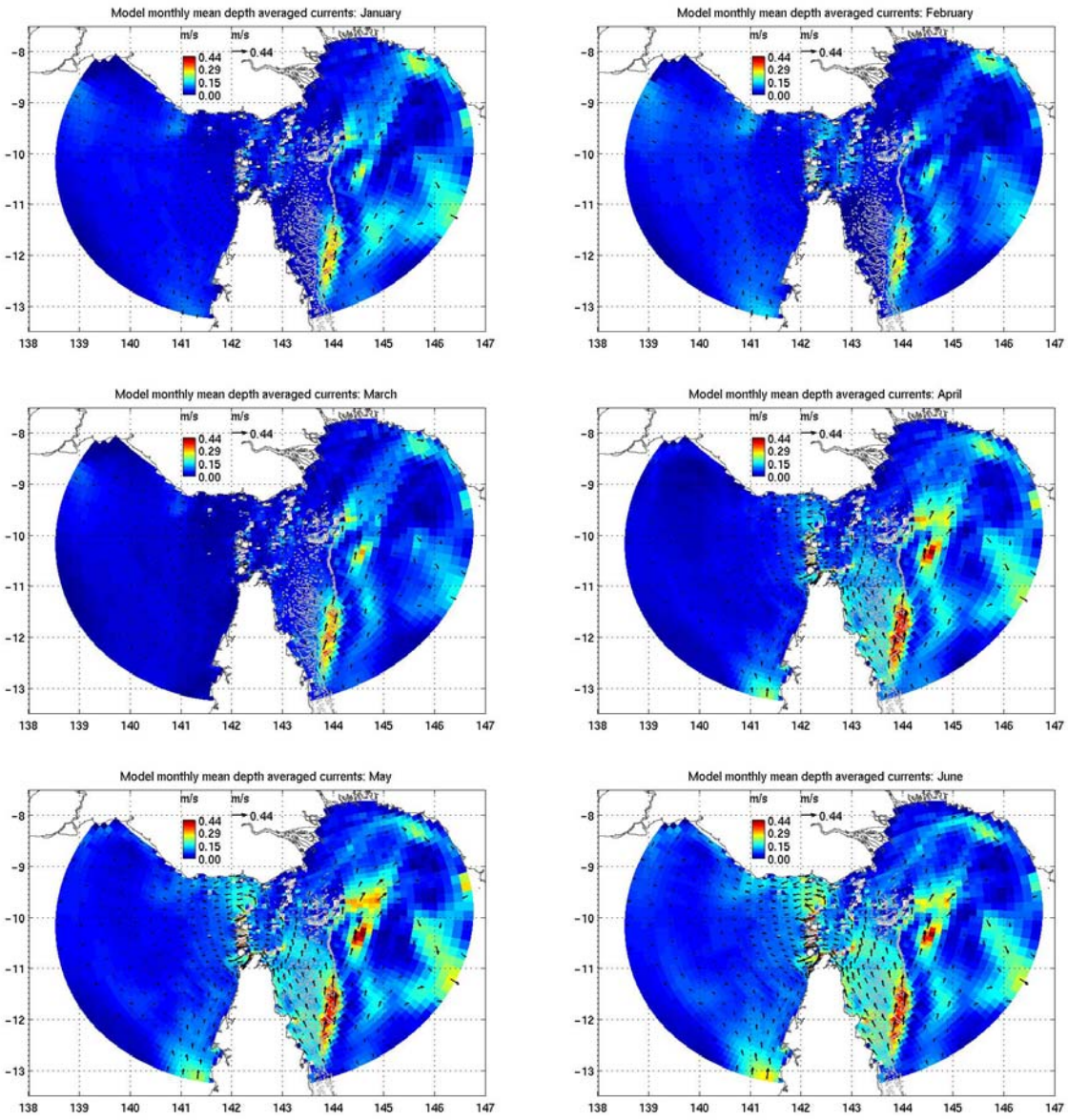

Figure 48: Monthly mean depth averaged currents based on eight years of model runs covering the period 1997-2004 (January to June).

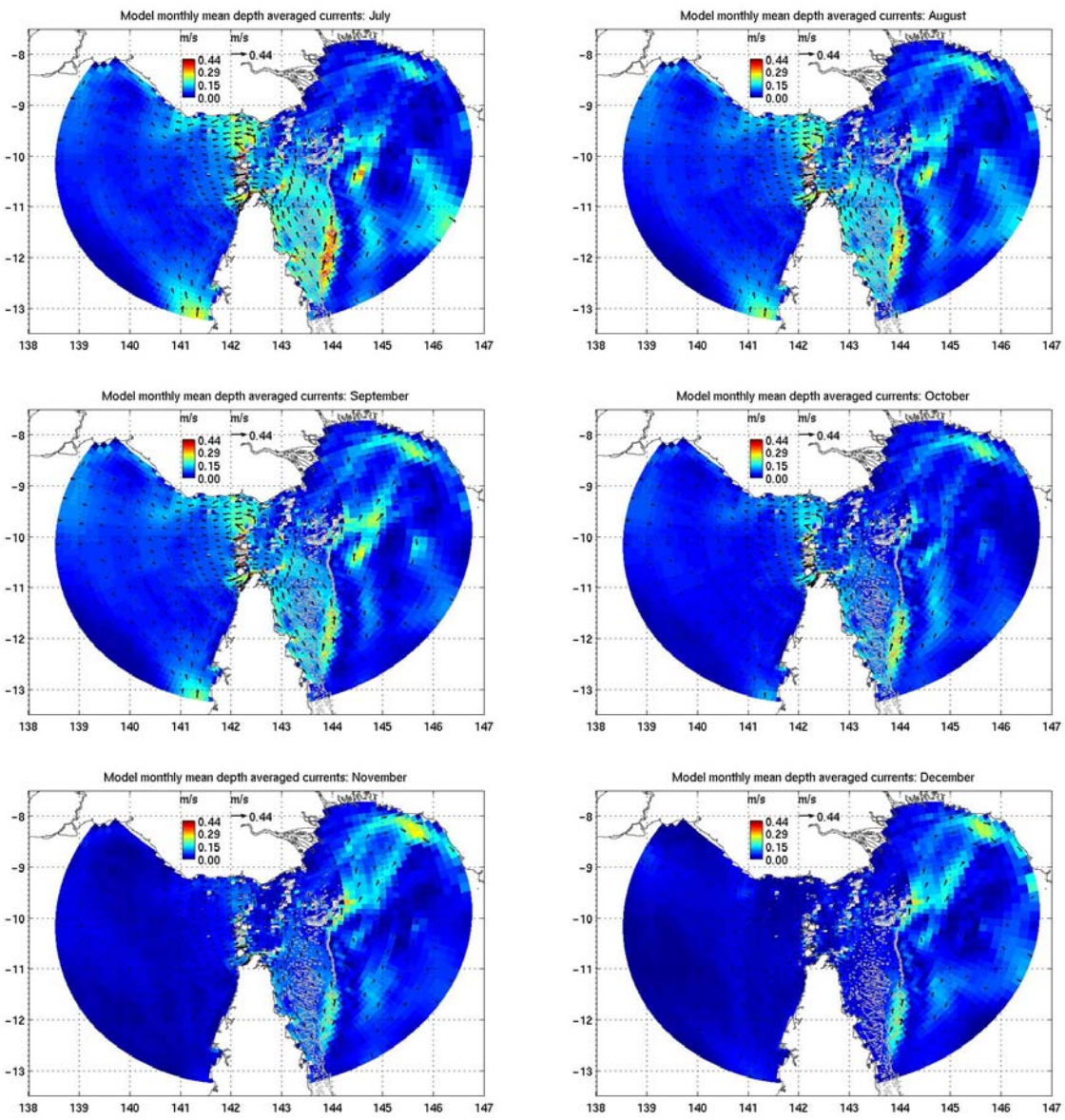

Figure 49: Monthly mean depth averaged currents based on eight years of model runs covering the period 1997-2004 (July to December).

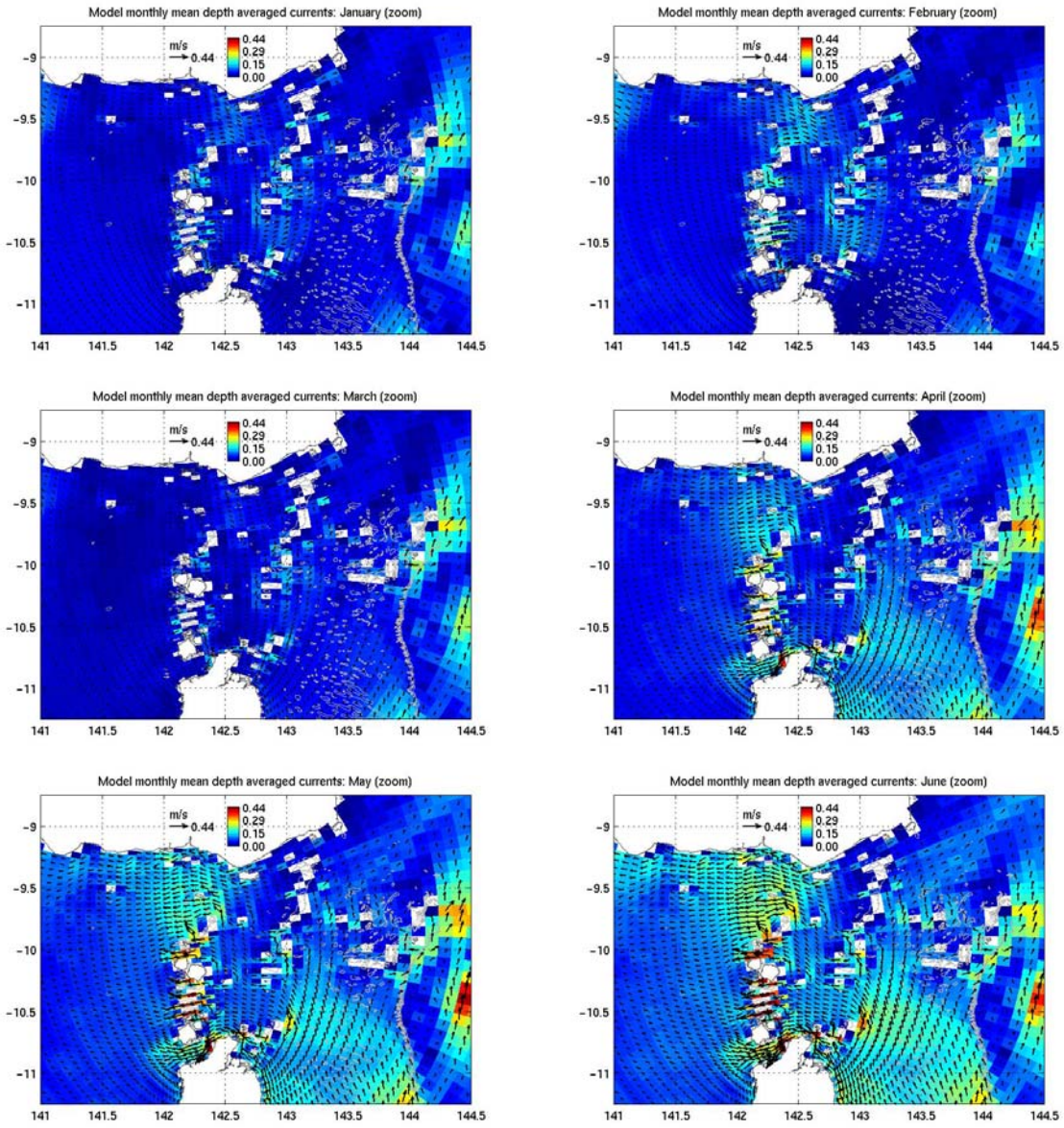

Figure 50: Monthly mean depth averaged currents based on eight years of model runs covering the period 1997-2004 (Torres Strait enlargement, January to June).

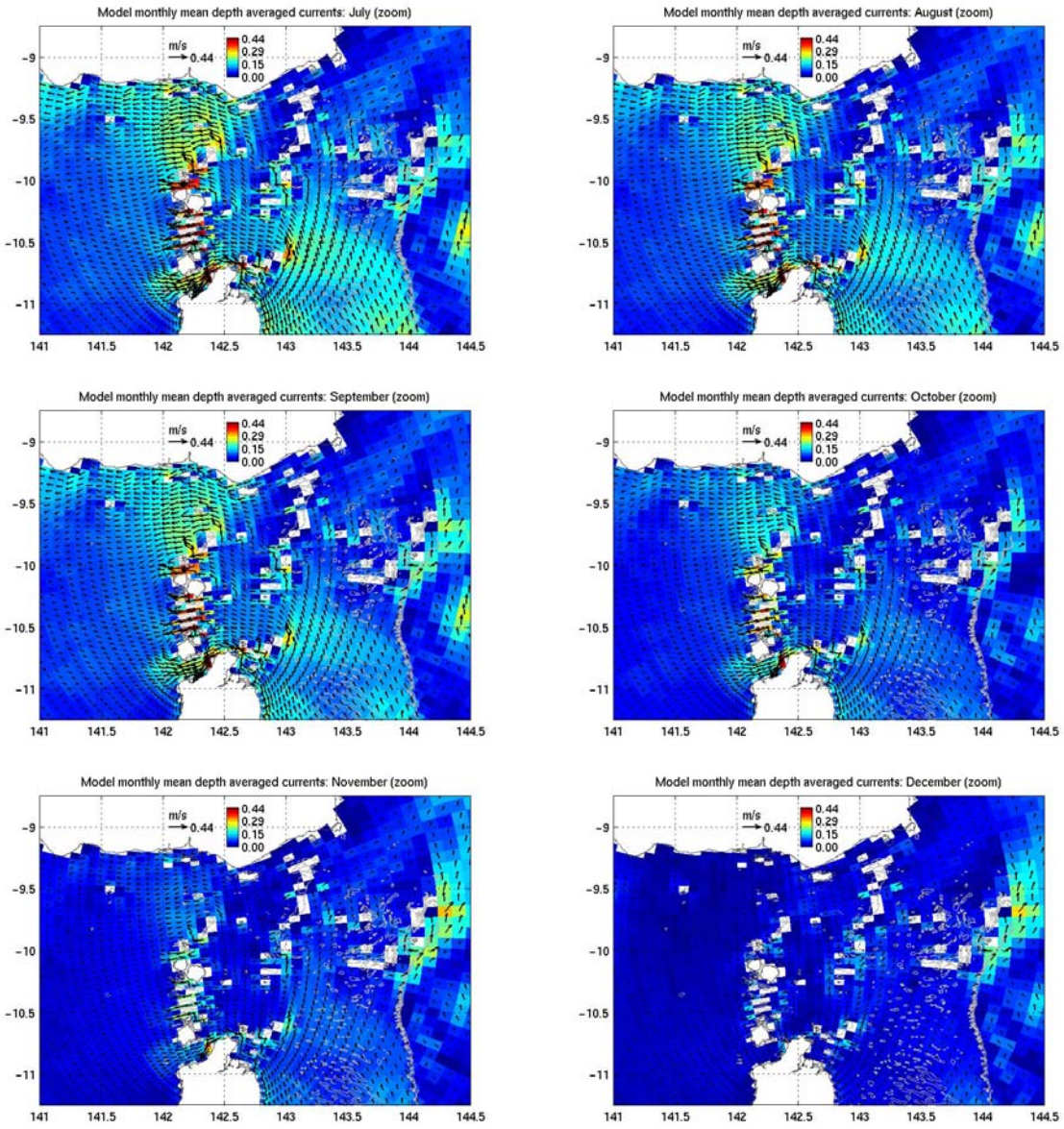

Figure 51: Monthly mean depth averaged currents based on eight years of model runs covering the period 1997-2004 (Torres Strait enlargement, July to December).

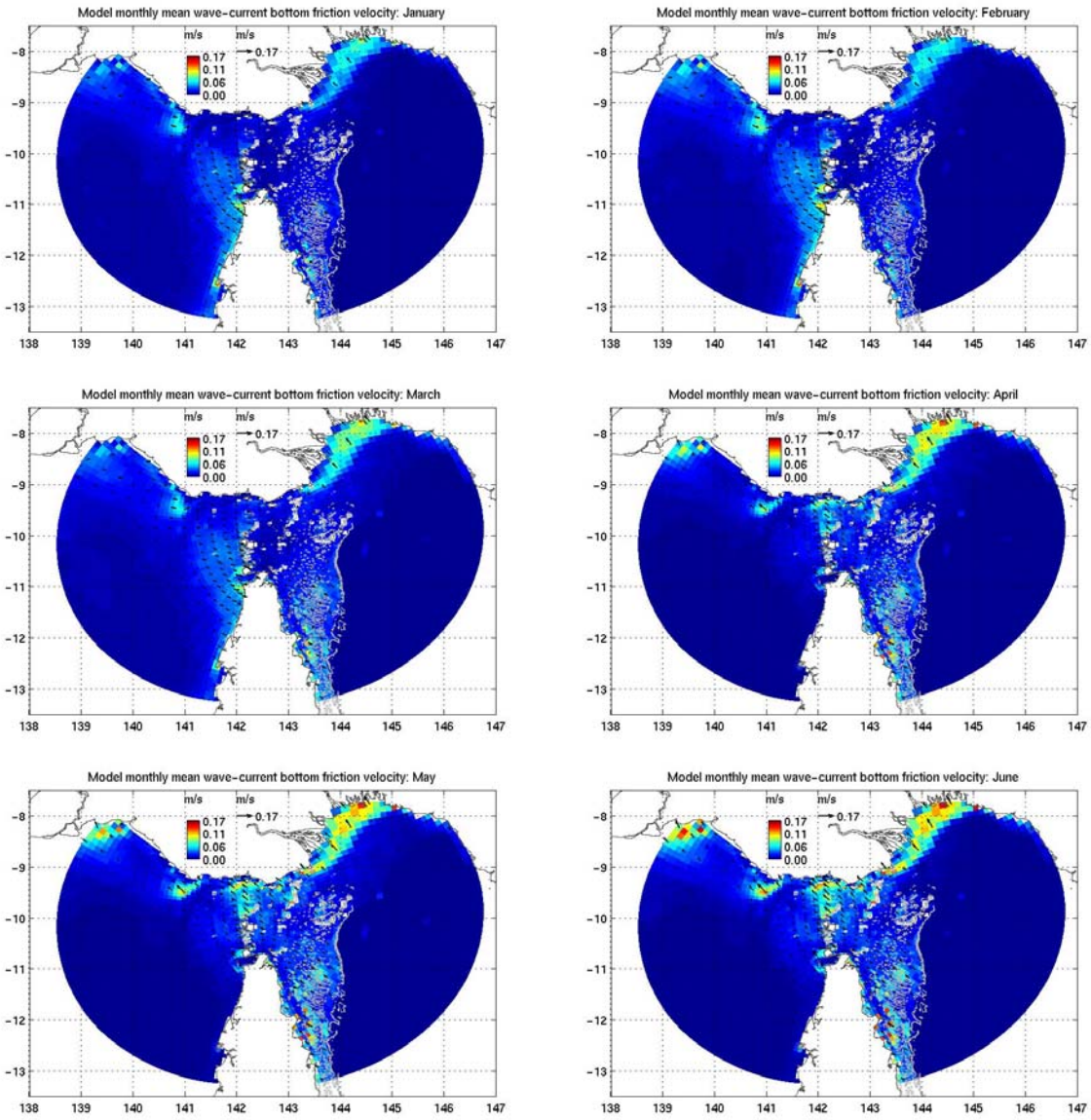

Figure 52: Monthly mean wave-current bottom friction velocity based on eight years of model runs covering the period 1997-2004 (January to June). The combined wave-current bottom friction velocity (i.e. square root of the ratio bottom stress to water density) was obtained according to van der Molen (2002) parameterization, in which the physical roughness height z_0 = 0.005 m was considered after the model currents calibration.

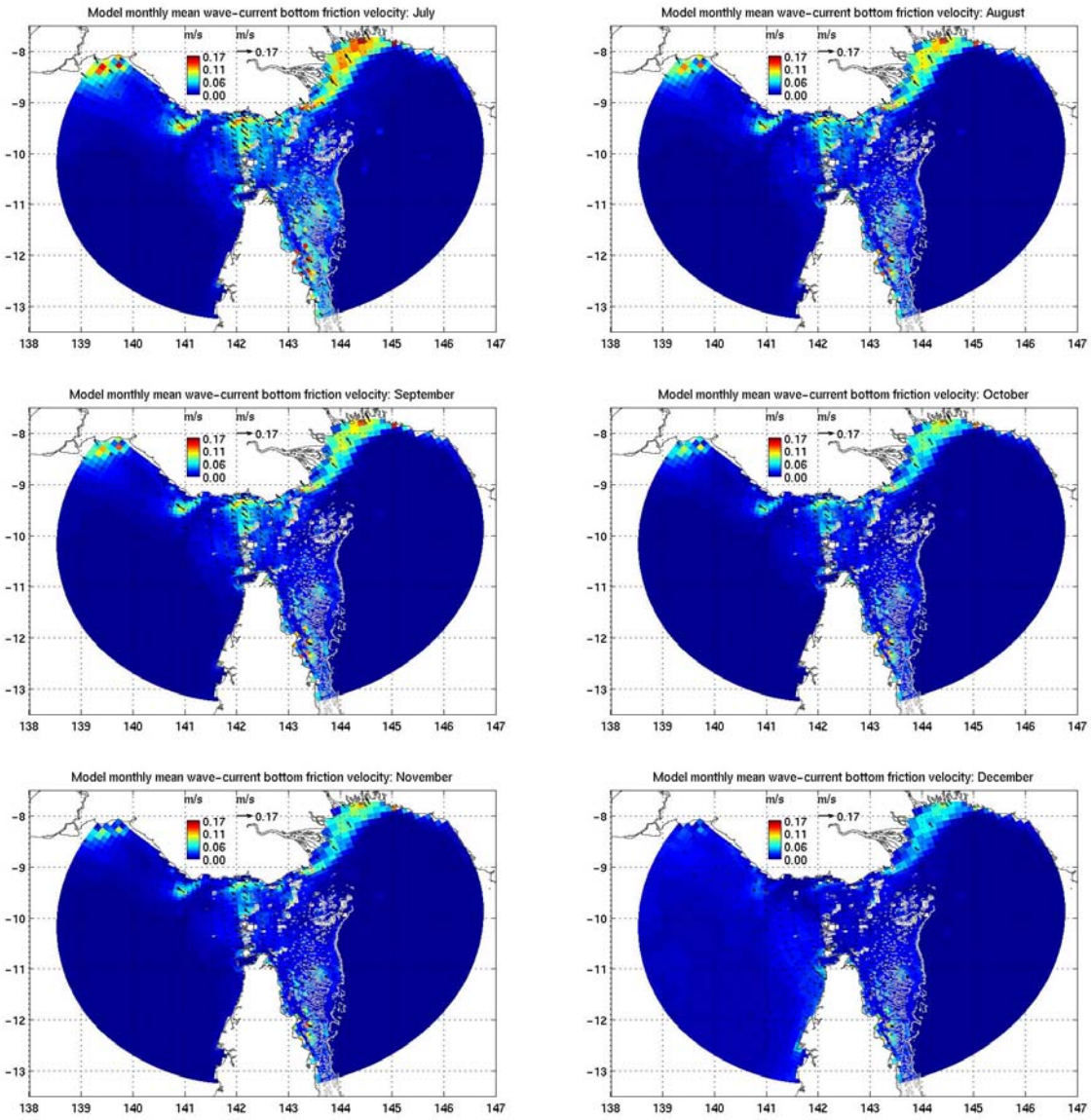

Figure 53: Monthly mean wave-current bottom friction velocity based on eight years of model runs covering the period 1997-2004 (July to December). The combined wave-current bottom friction velocity (i.e. square root of the ratio bottom stress to water density) was obtained according to van der Molen (2002) parameterization, in which the physical roughness height z_0 = 0.005 m was considered after the model currents calibration.

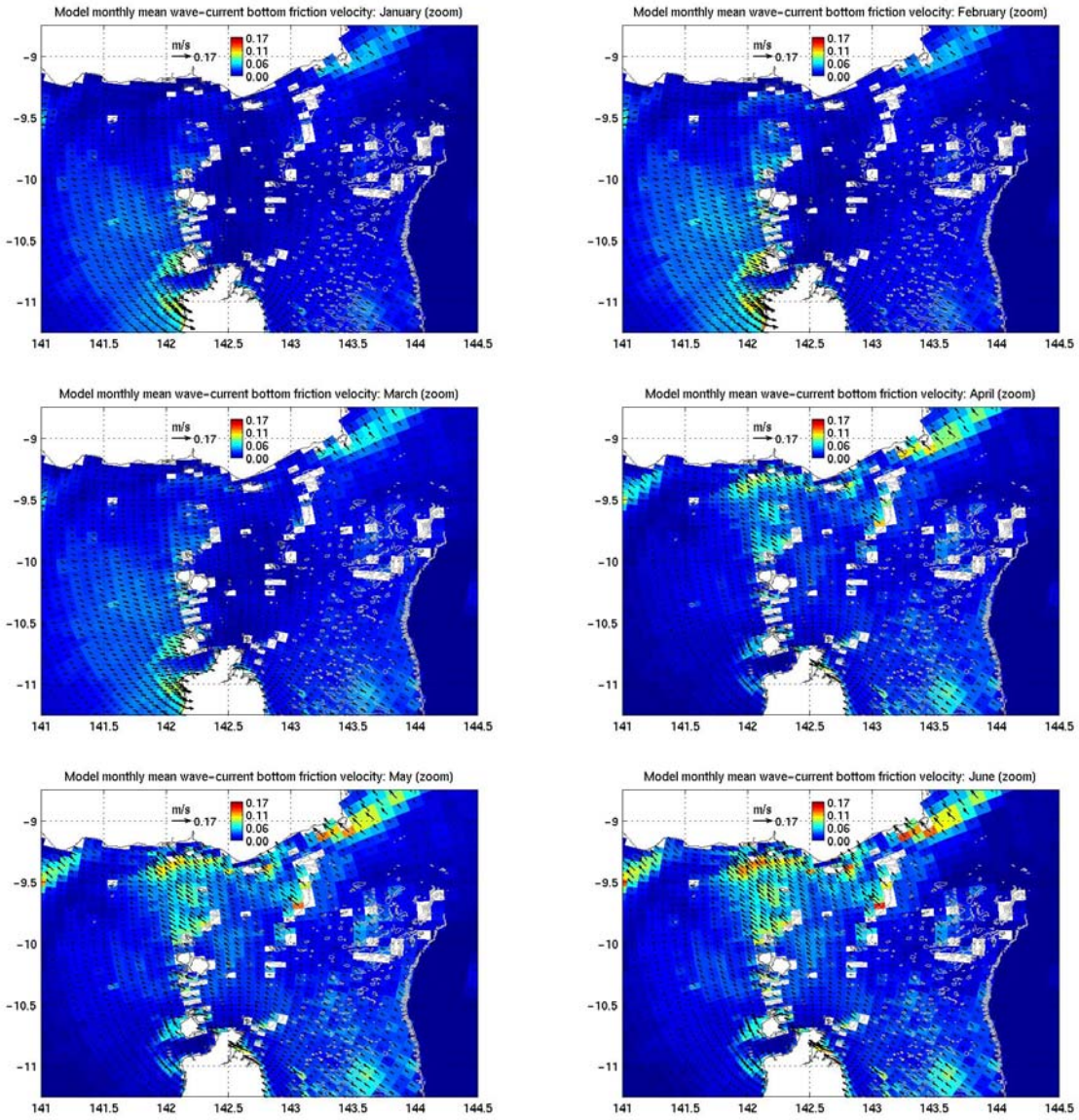

Figure 54: Monthly mean wave-current bottom friction velocity based on eight years of model runs covering the period 1997-2004 (Torres Strait enlargement, January to June).

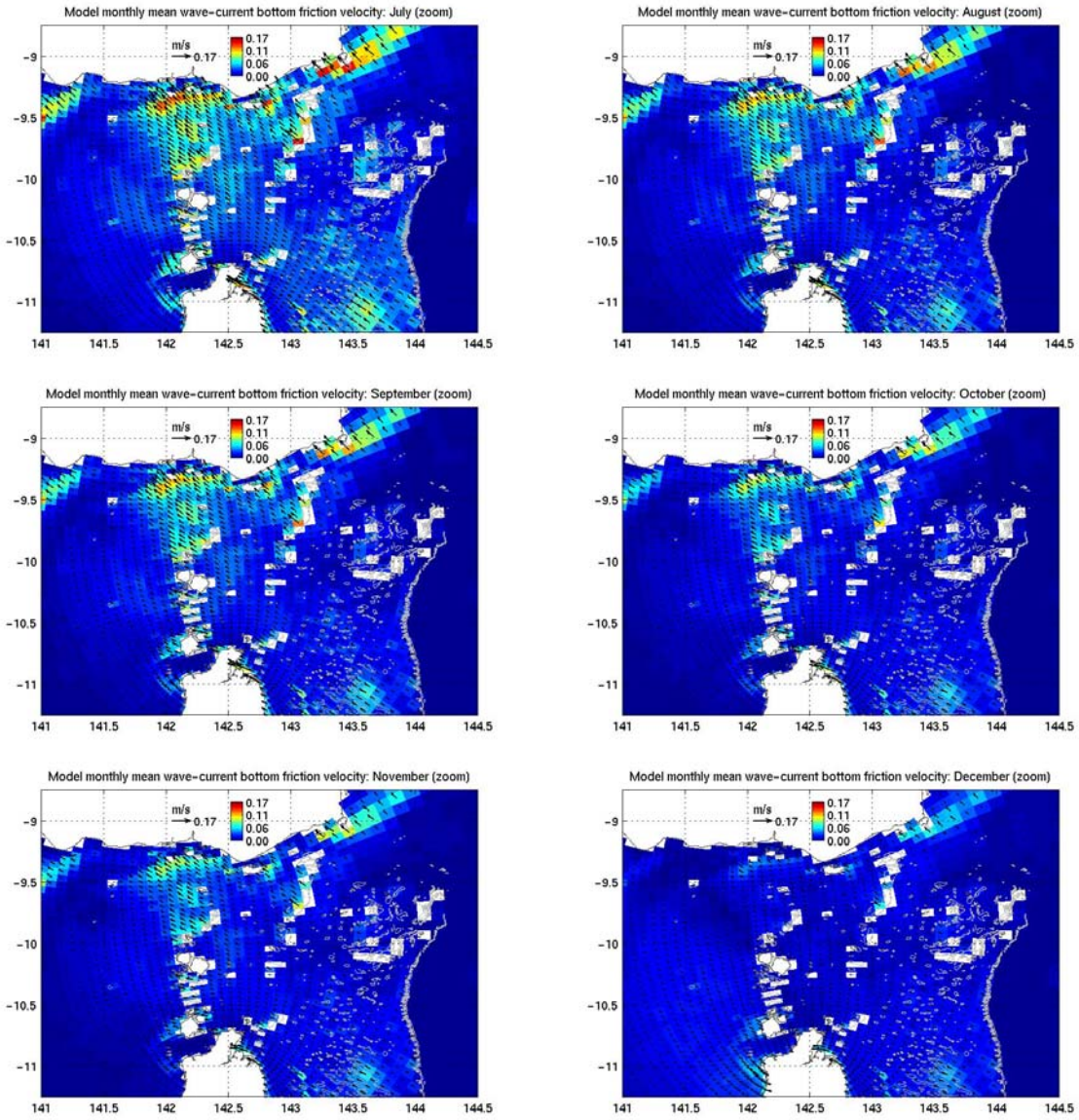

Figure 55: Monthly mean wave-current bottom friction velocity based on eight years of model runs covering the period 1997-2004 (Torres Strait enlargement, July to December).

5.3 Interannual variability

The temporal coverage of the Torres Strait model runs was eight years, which provided some basis for examining interannual variability in the circulation in the region. Anomaly fields relative to long-term (8-year) monthly averages were calculated for all months within the modeling period (1997-2004). This analysis was applied to model outputs of surface velocity, depth averaged velocity, and bottom friction velocity, which anomaly fields are shown on Appendices 9.3, 9.4 and 9.5 respectively. In addition, surface wind friction velocity and wave height anomaly fields are presented in Appendices 9.6 and 9.7 respectively.

In general terms, interannual variability in Torres Strait was highest over the monsoon period, reflecting year-to-year variability in wind forcing including the timing of the monsoon. During the trades, interannual variability was highest in the Coral Sea, reflecting

variability in the large-scale circulation patterns (OFAM) around the time when the Hiri Current and Gyre was near its peak strength.

5.3.1 Surface currents

Monthly mean surface current velocity anomalies were most significant in the Coral Sea, Gulf of Papua, and narrow channels within Torres Strait (Figure 56). These anomalies typically developed over several months and were highly variables between years, with particularly strong anomalies in 1997, 1999, 2000 and 2001. Fluctuations in the large-scale oceanic circulation (i.e. the Hiri Current and Gyre) were clearly a major contributor to anomalies in the Coral Sea. However, the Coral Sea anomalies were not strongly correlated with those in Torres Strait, which mostly occurred during the monsoon transitional months and was likely to be associated with variability in winds. While local winds were relatively consistent throughout the years (Appendix 9.6), small changes in the timing of the monsoon had the potential to produce large anomalies around the change in season.

The Torres Strait surface current anomalies (0.1 - 0.2 m s^{-1}) were large enough to significantly affect the net seasonal surface layer drift. For example, monsoon conditions and associated eastward surface flow persisted past March in 1997 and past April in 1999, while the westward surface flow persisted past November in 1998, 2000 and 2002 (Figure 56).

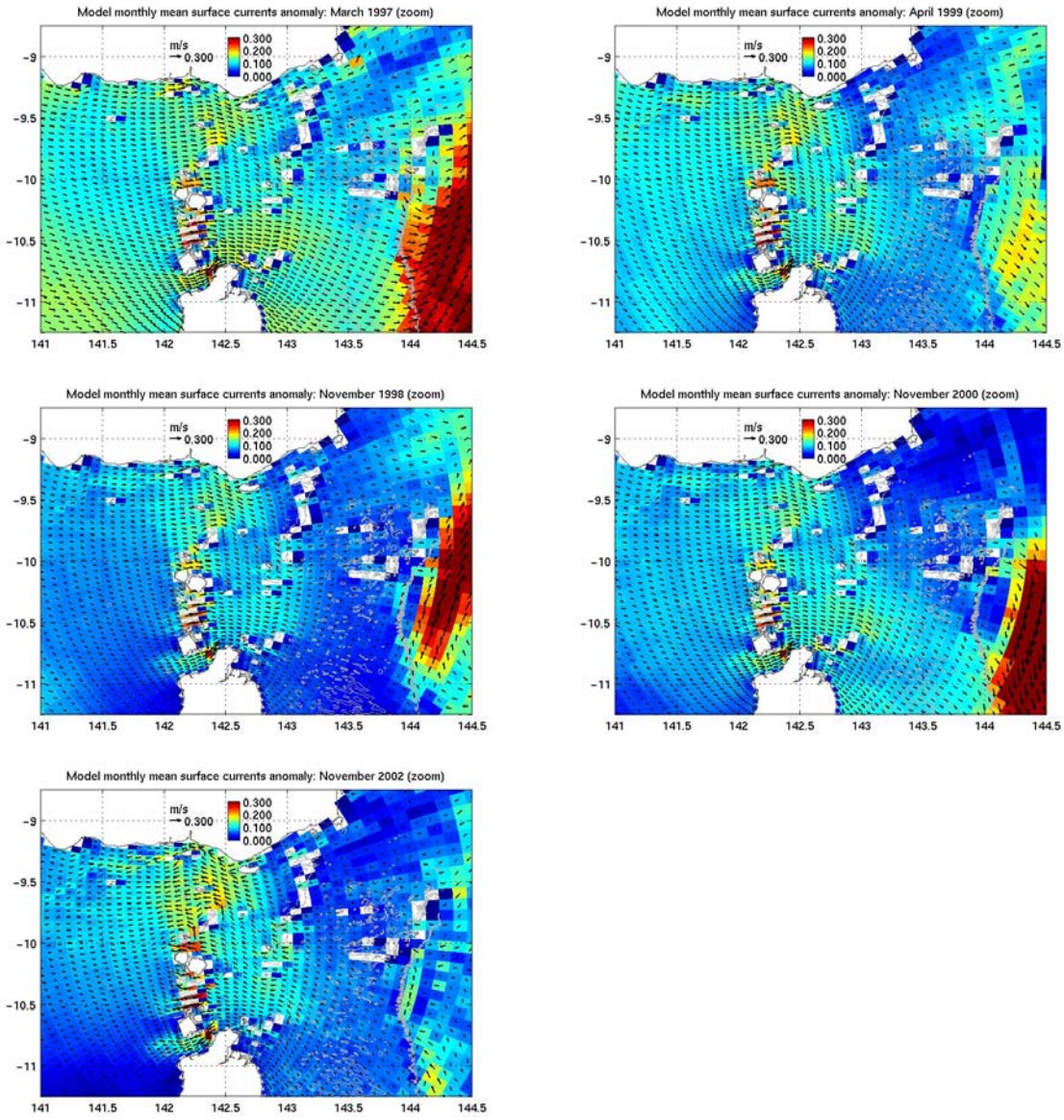

Figure 56: Examples of large surface current anomalies from March 1997 and April 1999 (top); and November 1998, 2000 and 2002 (middle and bottom). Detailed monthly mean anomalies are presented in Appendix 9.3.

5.3.2 Depth-averaged currents

The distributions of interannual anomalies in depth-averaged currents were generally similar to surface currents and again typically developed over two to three months. During the monsoon, the mean depth averaged circulation offshore of the Great Barrier Reef reversed between December 1999 and December 2000 from clockwise to anticlockwise of similar strength (0.15 m s^{-1}). While interannual variability was generally weaker during the trade season, depth averaged northwestward flow off the Great Barrier Reef virtually disappeared in August 2001 and then was almost double its averaged strength (0.6 m s^{-1}) in July 2003.

Significant monthly mean depth averaged current velocity anomalies in northwest Torres Strait were most significant during the monsoon season and were related to winds rather than Coral Sea anomalies. For example, the depth averaged eastward monsoon flow was

more than twice its average strength (0.25 m s^{-1}) in February 1999 and persisted through April 1999. This contrasts to 1998, when the flow had already started to reverse by February in that year. Similarly, weak westward depth-averaged currents of around 0.05 m s^{-1} increased by a factor of three over November 2002, but was already eastward in November 1998 and 2000.

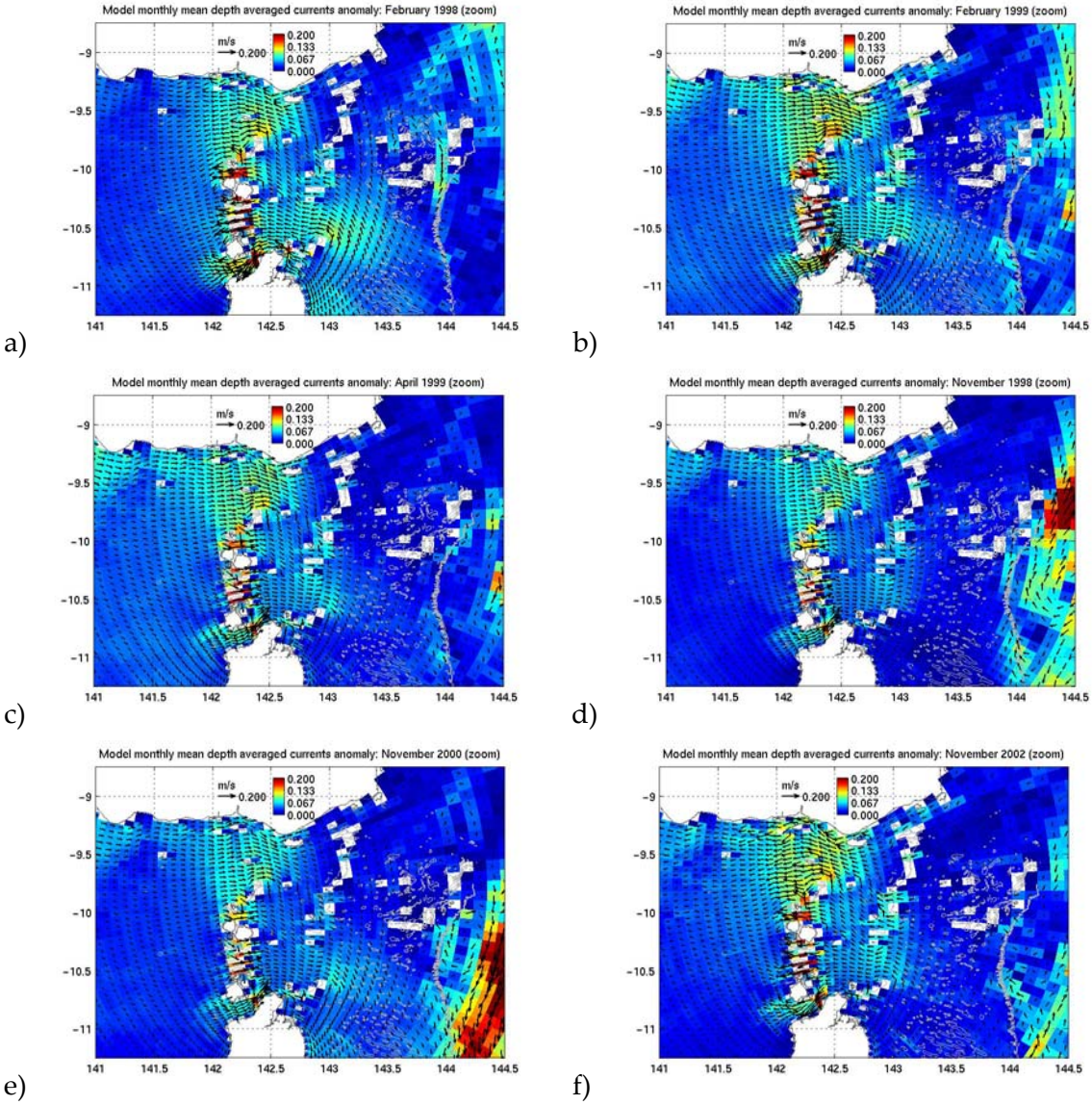

Figure 57: Examples of large depth-averaged current anomalies indicative of early westward flow in February 1998 and sustained eastward flow from February to April 1999 (a, b and c). Eastward flow began early in November 1998 and 2000, while westward flow persisted through November 2002 (d, e and f). Detailed monthly mean anomalies are presented in Appendix 9.4.

5.3.3 Bottom friction induced by waves and currents

Monthly mean bottom wave-current friction velocity anomalies were most significant (0.04 - 0.06 ms-1) in shallow waters on the western side of Torres Strait and the west coast of Cape York (Figure 58). They typically developed within one or two months, mostly over the

monsoon. However, the most significant anomalies that occurred in the Gulf of Papua were during the trades (0.02 - 0.06 m s-1 in May 1999, April - May 2002, and August 2004).

When Torres Strait current anomalies were eastward, Ekman boundary layer dynamics ensured that friction velocity anomalies were directed southeastward as in Figure 58. These results show persistence of the monsoon through March 1997 and April 1999 and an enhanced monsoon in January 1998 and December 2001. Conversely, November 1999 and 2000 show an early monsoon and southeastward trend (Figure 58). Early northwestward trends occurred in March 1999, 2000 and 2001 (consistent with westward current anomalies), while trades persisted over February and March 2000 (Figure 59). A sustained northwestward trend also occurred over November and December 2002 and November 2003 (Figure 60).

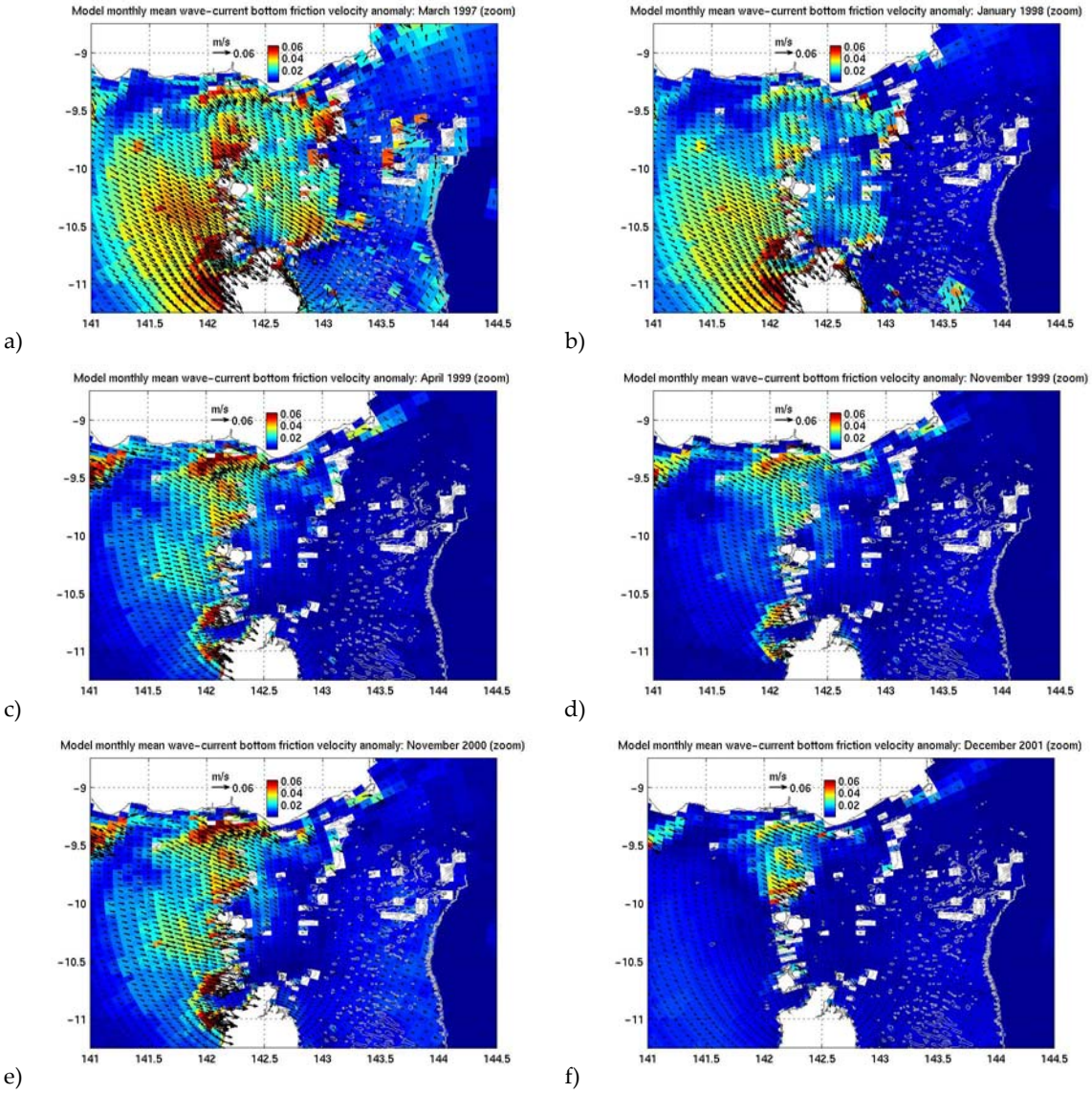

Figure 58: Wave-current bottom friction velocity anomaly indicating persistence of the monsoon through March 1997 and April 1999 and an enhanced monsoon in January 1998 (a, b and c). November 1999 and 2000 show an early monsoon and southeastward trend, while December 2001 shows another enhanced monsoon (d, e and f). Detailed monthly mean anomalies are presented in Appendix 9.5.

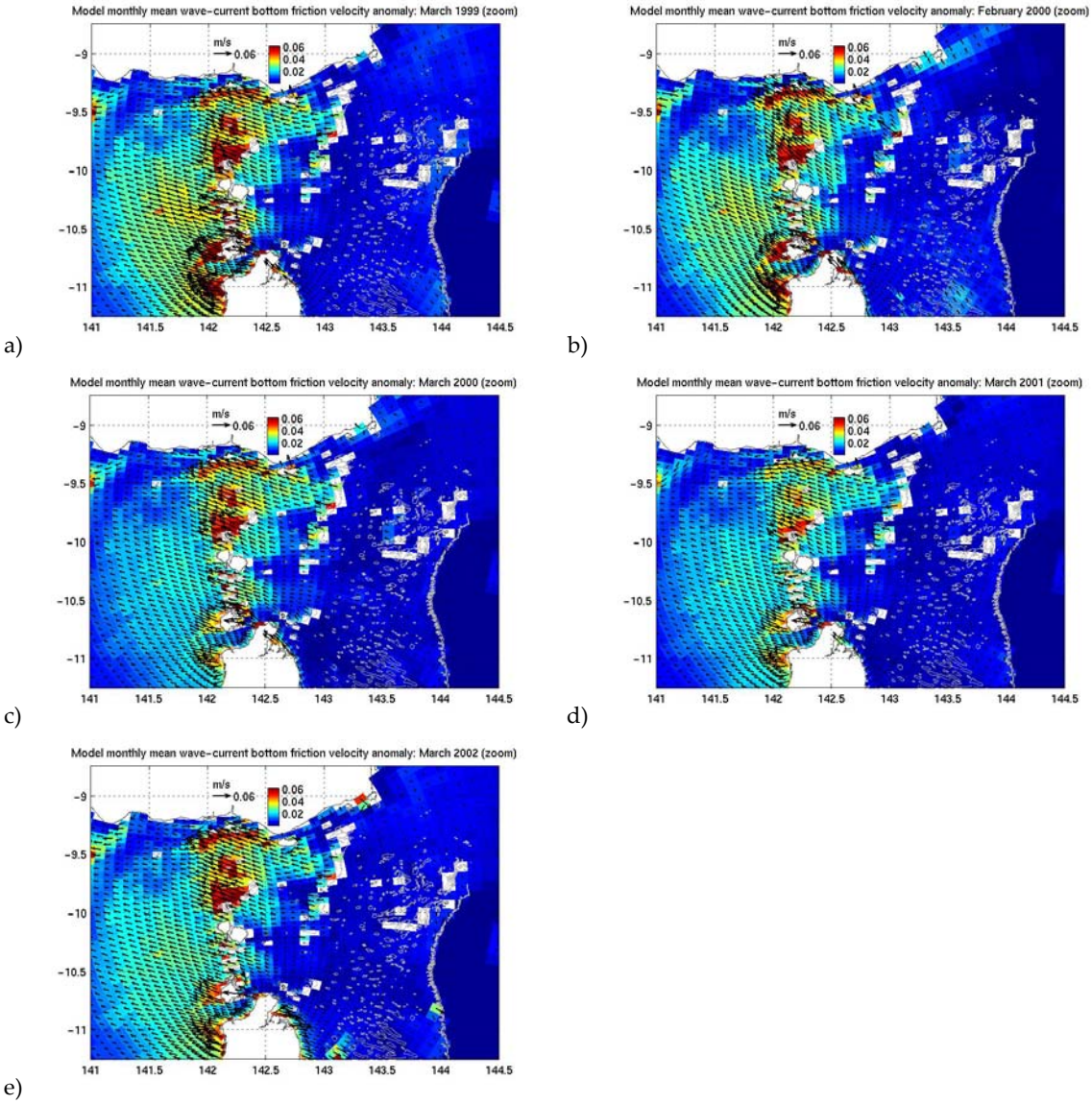

a) b)

c) d)

e)

Figure 59: Wave-current bottom friction velocity anomaly indicating early northwestward trends in March 1999, 2000 and 2001 (a, b and c), while trades persisted over February and March 2000 (d and e). Detailed monthly mean anomalies are presented in Appendix 9.5.

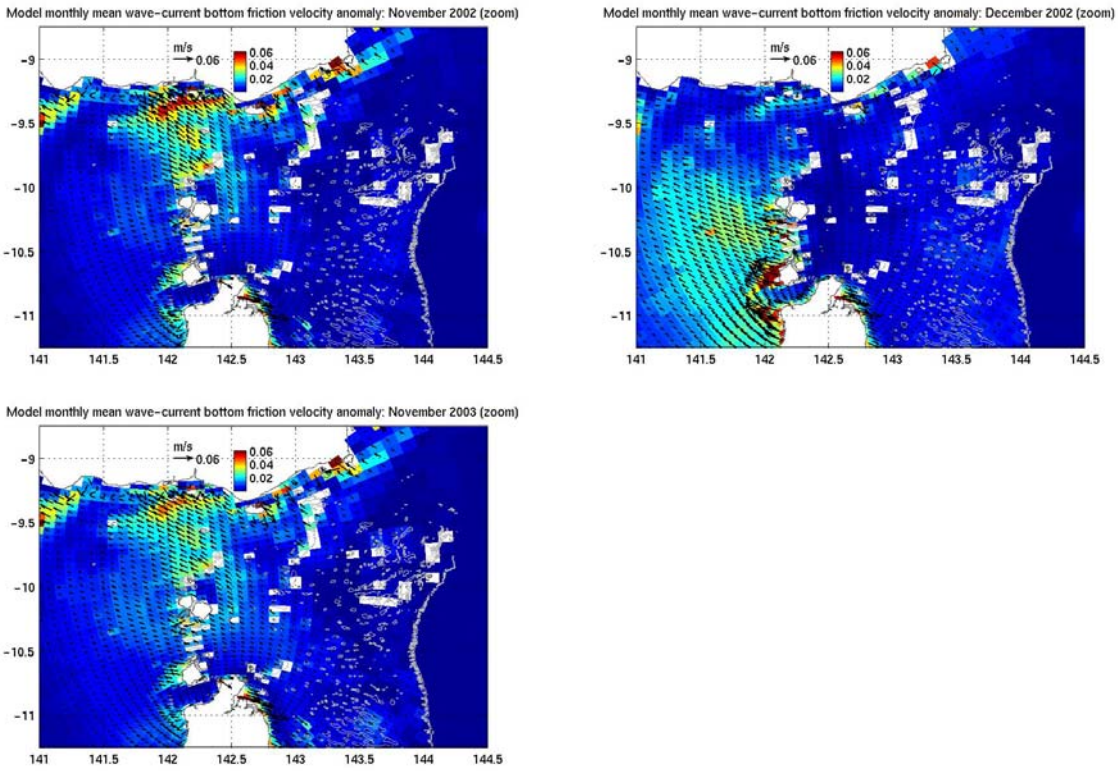

Figure 60: Wave-current bottom friction velocity anomaly indicating a sustained northwestward trend over November and December 2002 and November 2003. Detailed monthly mean anomalies are presented in Appendix 9.5.

5.4 Torres Strait through-flow

The mean annual flux of water through Torres Strait is of interest in terms of its contribution to both flushing of Gulf of Carpentaria (with implications for its heat, salt and nutrient budgets) and transport from the tropical Pacific to the tropical Indian Ocean. The subtidal component of this flux is mostly driven by the hydraulic gradient resulting from mean sea level differences between the Gulf of Carpentaria and the Coral Sea, which in turn are established and maintained through the broader-scale wind set-up and set-down (Appendix 9.8).

The net flux through a north-south transect at 142.436°E (Figure 61) has been estimated for the period 1997-2004 using low-pass filtered depth-averaged currents estimated by the model. Averaged over all years, the flow through Torres Strait consists of a mean westward flux of approximately 0.20 Sv (1 Sv= 10^6 m^3 s^{-1}) running over a mean 271-day trade season and a mean eastward flux of approximately 0.07 Sv running over a mean 96-day monsoon season. This corresponds to an annual mean westward flux of approximately 0.13 Sv.

The through-flow flux was relatively well distributed across Torres Strait, although the flux through the 'middle section' (Figure 61) only contributed around one quarter (Figure 62). Interannual variability in the wind fields also induced significant variability in the through-flow (Figure 62). For example, westward fluxes during the trade season were anomalously high in 1997, 2000 and 2001, while high eastward fluxes during the monsoon occurred in

1999 and 2004. During the 2000-2001 monsoon, the eastward flux actually reversed and became westward for a short period of time.

The total accumulated volume of water carried through the strait (i.e. time integrated flux) from the start of the season to any time within the season is referred to here as the 'seasonal accumulated volume' and provides a good indication of the relative strength of each season (Figure 63). The trade wind seasons show maxima in 1997 and 2001 and the time series suggest the possibility of a 4-5 year cycle, although this clearly can't be confirmed with outputs from only eight seasons. The monsoon seasons show no obvious interannual cycle or relationship to the following trade wind season, except perhaps that the strongest monsoon (1998-1999) was followed by the weakest trades season (Figure 63).

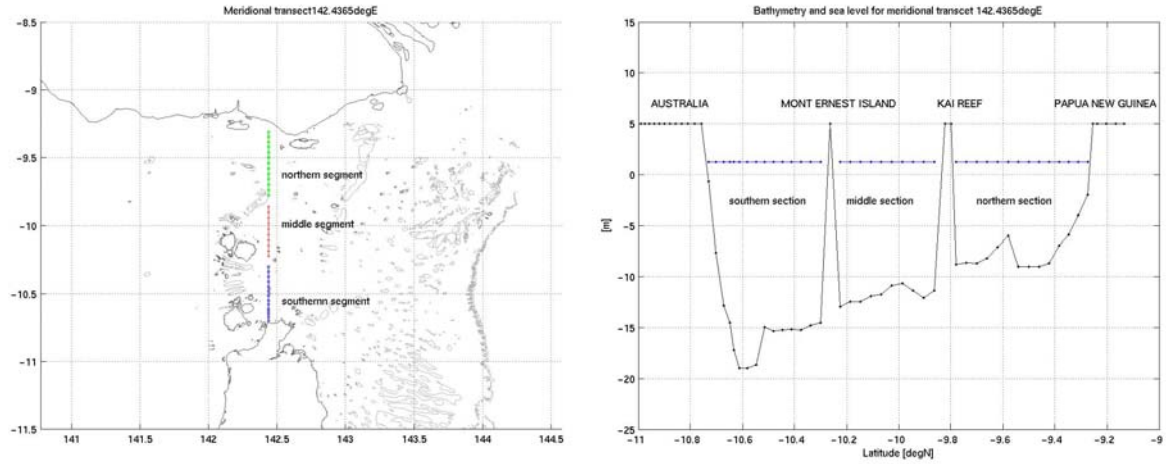

Figure 61: Definition of the meridional transect section at 142.436°E and corresponding bathymetric profile used to estimate low frequency currents across and through-strait.

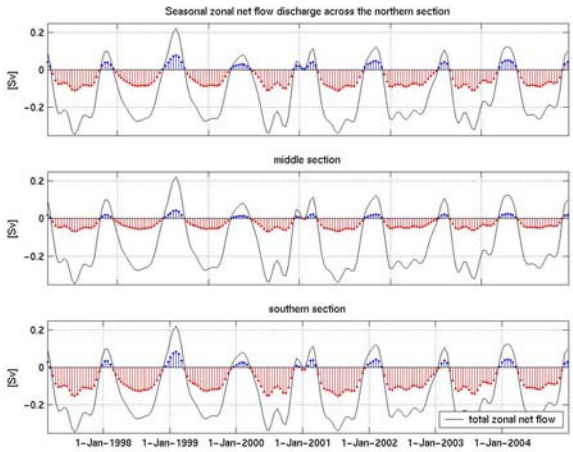

Figure 62: Time series of flux through northern, middle and southern sections of the transect at 142.436°E.

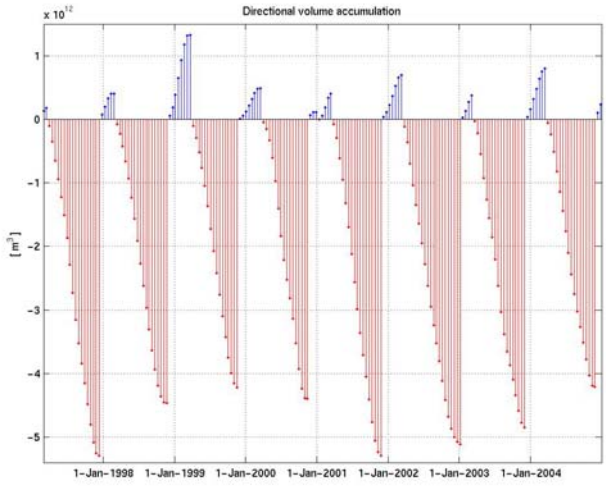

Figure 63: Seasonal volume accumulation through the transect at 142.436°E. (eastward is positive).

6 Conclusion

A circulation model has been developed for the Torres Strait region to investigate aspects of regional climatic forcing and circulation, shelf scale processes, and local coastal process. This represents the first attempt to model the circulation in Torres Strait region using realistic forcing by winds, tides, and the large-scale regional circulation.

Simulations covering a period of eight years have allowed the tidal, seasonal, and interannual characteristics to be investigated. Instantaneous current patterns were strongly dominated by the barotropic tide and its spring-neap cycle. However, longer-term transports through the strait were mainly controlled by the seasonal winds, which switched from the northwesterly summer monsoon to southeasterly trades in winter. The longer trade winds season and its stronger winds ensured a net westward flux of water from the Coral Sea to the Arafura Sea. Off the shelf in the Coral Sea, the large-scale regional circulation also had a major influence.

Model results were shown to be relatively insensitive to adjustable model parameters. However, model performance was strongly dependent on the quality of the forcing fields. For example, the prediction of low-frequency inner-shelf currents was improved substantially when the climatological temperature and salinity forcing (CARS) was replaced by global model forcing (OFAM). While the atmospheric and oceanographic forcing were generally realistic, the model could be further improved by imposing a more accurate tidal signal along the Gulf of Carpentaria boundary and incorporating higher resolution winds to capture the effect of sea breezes on the circulation. The model grid resolution may also be increased to provide a better description of small scale circulation patterns, such as island and reef wakes and narrow passages jets.

As part of Torres Strait CRC study, the circulation model has been coupled to a sediment transport model to examine resuspension, transport, and deposition processes in Torres Strait (Margvelashvili and Saint-Cast, 2006). For this purpose, bottom stress distribution (including wave enhancement) and low frequency current patterns were particularly critical. Finally, current fields from the model will be used in the integrated ecosystem modelling for evaluating Torres Strait multiple-use management strategies (Pantus et al. 2006), where they determined the transport of suspended material such as chemical contaminants and fish larvae.

7 Acknowledgements

The authors would like to thank Andrew Heap[1] for supervising aspects of the project; Mike Herzfeld[2], John Andrewartha[2] and Pavol Sakov[2] for technical advice on various aspects of the model development; Jim Mansbridge[2] and Mark Hemer[1,2] for model output and field data management; and Uwe Rosebrock[2] and Peter Campbell[2] for IT support.

[1.] *Geoscience Australia – Petroleum and Marine Division, GPO Box 378, Canberra, ACT 2601*
[2.] *CSIRO - Marine and Atmospheric Research, GPO Box 1538, Hobart, TAS 7001*

8 References

[1] Alongi, D. M., Christoffersen, P., Tirendi, F., and Robertson, A. I., 1992. The influence of freshwater and material export on sedimentary facies and benthic processes within the Fly River Delta and adjacent Gulf of Papua (Papua New Guinea). Continental Shelf Research 12:287-326.

[2] Bode, L. and L. Mason, 1994. Tidal modelling in Torres Strait and the Gulf of Papua. Recent Advances in Marine Science and Technology '94, James Cook University of North Queensland, Townsville, 55-65.

[3] Bowden , F. and Hamilton, P., 1975. Some experiments with a numerical model of circulation and mixing in a tidal estuary. Estuarine and coastal Marine Science 3, 281-301.

[4] Bruce, B. D., S. A. Condie, and C. A. Sutton, 2001. Larval distribution of blue grenadier (Macruronus novaezelandiae Hector) in south-eastern Australia: further evidence for a second spawning area. Mar. Freshwat. Res. 52: 603-610.

[5] Clarke, A.J., 1989. Application of a frictional channel flow theory to flow in the Prince of Wales Channel, Torres Strait.

[6] Condie, S. and Mansbridge, J., 2002. Surrogates I – Predictors, impacts, management and conservation of the benthic biodiversity of the Northern Prawn Fishery. FRDC Project 2000/160, chapter 3.2: hydrodynamic models.

[7] Condie, S.A., C. Fandry, D. McDonald, J. Parslow and K. Sainsbury, 2003. Linking ocean models to coastal management on Australia's North West Shelf. Eos. Transactions, American Geophysical Union, 84:49-53.

[8] Condie, S.A., N.R. Loneragan and D.J. Die, 1999. Modelling the recruitment of tiger prawns (Penaeus esculentus and P. semisulcatus) to nursery grounds in the Gulf of Carpentaria, northern Australia: implications for assessing stock-recruitment relationship. Mar Ecol. Prog. Ser., 178:55-68.

[9] Csanady, G.T., 1982. Circulation in the coastal ocean, D. Reidel Publishing Company.

[10] Daniell, J., 2004. Improvement of Torres Strait Bathymetry. Internal report, Geoscience Australia.

[11] Daniell, J., 2005. Improvement of Torres Strait Bathymetry. Internal report, Geoscience Australia.

[12] Daniell, J., A.D., Heap, , H. Hemer, E. Mathews, P.T. Harris, S. Kerville and L. O'Grady, 2006. Biophysical Processes in the Torres Strait Ecosystem, Post-cruise Report, Geoscience Australia Marine Survey S273. Geoscience Australia Record 2006 (In prep.).

[13] Dyer, K. R., 1986. Coastal and Estuarine Sediment Dynamics. John Wiley & Sons, 342 pp.

[14] Eanes R.J. and S.V. Bettadpur, 1999. CSR 4.0 global ocean tide model. Center for Space Research, Austin, Texas.

[15] Flater, D., 1999. Harmonic tide clock and tide calculator. WWW page: http://www.flaterco.com/xtide.

[16] Grant, W. D. and O. S. Madsen, 1979. Combined wave and current interaction with a rough bottom. J. Geophys. Res., 84, 1797-1808.

[17] Harris, P.T., 1993. Near-bed current measurements from Torres Strait obtained during Jan–Mar 1993 aboard RV Southern Surveyor. Technical Report 29. Ocean Sciences Institute, University of Sydney.

[18] Heap, A.D., H. Hemer, J. Daniell, E. Mathews, P.T. Harris, S. Kerville and L. O'Grady, 2005. Biophysical Processes in the Torres Strait Ecosystem, Post-cruise Report, Geoscience Australia Marine Survey S266. Geoscience Australia Record 2005/11.

[19] Hemer M.A., P.T. Harris, R. Coleman, J. Hunter, 2004. Sediment mobility due to currents and waves in the Torres Strait – Gulf of Papua region. Cont. Shelf Res. 24:2297-2316.
[20] Herzfeld, M., J. Waring, J. Parslow, N. Margvelashvili, P. Sakov and J. Andrewartha, 2004. SHOC, Sparse Hydrodynamic Ocean Code, V1.0, Scientific Manual, CSIRO Marine Research.
[21] Kallberg, P., A. Simmons, S. Uppala, and M. Fuentes, 2004. The ERA-40 archive, European Centre for Medium-range Weather Forecasts (ECMWF), ECMWF Re-Analysis Project (ERA) ERA-40 Project Report Series 17, 31 pp.
[22] Large, W.G. and S. Pond, 1981. Open ocean momentum flux measurements in moderate to strong winds, J. Phys. Oceanogr., 11, 324-336.
[23] Livingston R.J., S.E. McGlynn and X Niu (1998) Factors controlling seagrass growth in the gulf coastal system: water and sediment quality and light. Aquatic botany (60) 135-159.
[24] Longstaff, B.J. and W.C. Dennison (1999) Seagrass survival during pulsed turbidity events:the effects of light deprivation on the seagrasses Halodule pinifolia and Halophila ovalis. Aquatic Botany 65 105–121.
[25] Margvelashvili, N. and Saint-Cast, F., 2006. Sediment Modelling in Torres Strait. Technical Report. (In prep.)
[26] Mellor, G.L. and T. Yamada, 1982. Development of a turbulence closure model for geophysical fluid problems. Rev. Geophys., 20, 851 – 875.
[27] Meyers, G., R.J. Bailey and A.P. Worby, 1995. Geostrophic transport of Indonesian throughflow. Deep Sea Res. Part I, 42, 1163-1174.
[28] Pantus, F., 2006. Integrated ecosystem modeling for evaluating Torres Strait multiple-use management strategies. (In prep.)
[29] Qu, T. and E. Lindstrom, 2002. A climatological interpretation of the circulation in the western south Pacific, J. Phys. Oceanogr., 32, 2492-2508.
[30] Ridgeway, K. R., J. R. Dunn and J. L. Wilkin, 2002. Ocean interpolation by four-dimensional weighted least squares—Applications to the waters around Australiasia. J. Atmos. Oceanic Technol., 19, 1357–1375.
[31] Ridgeway, K. R., J. S. Godfrey, G. Mayers and R. Bailey, 1993. Sea level response to the 1986-1987 El Nino – Southern Oscillation event in the Western Pacific in the vininity of Papua New Guinea. Journal of Geophysical Research 98, C9, 16387-16395.
[32] Schiller, A., G. B. Brassington, R. Fiedler, D. Griffin, J. Mansbridge, P. R. Oke, K. Ridgeway, N. R. Smith, 2005. Eddy-resolving Ocean Circulation in the Asian-Australian region inferred from an ocean reanalysis effort, J. Geophys. Research (in prep.).
[33] Smagorinsky, J., 1963. General circulation experiments with the primitive equations, I. The basic experiment. Mon. Wea. Rev., 91, 99 – 164.
[34] Van der Molen, J., 2002. The influence of tides, wind and waves on the net sand transport in the North Sea. Continental Shelf Research, 22, 2739-2762.
[35] Van Leer, B., 1979. Towards the ultimate conservative difference scheme. V: a second order sequel to Godanov's method. J. Comput. Phys., 32, 101-136.
[36] Walker, S.J., 1999. Coupled hydrodynamic and transport models of Port Phillip Bay, a semi-enclosed bay in south-eastern Australia. Mar. Freshwat. Res. 50: 469-481.
[37] Wijffels, S., and G. A. Meyers, 2004. An Intersection of Oceanic Wave guides: Variability in the Indonesian Throughflow Region, J. Physical Oceanography, 34,1232-1253.
[38] Wolanski, E., 1993. Water circulation in the Gulf of Carpentaria. Journal of Marine Systems 4:401-420.

[39] Wolanski, E., G.L. Pickard and D.L.B. Jupp, 1984a. River plumes, coral reefs and mixing in the Gulf of Papua and northern Great Barrier Reef. Estuarine, Coastal Shelf Sci., 18:291-314.
[40] Wolanski, E., J. Imberger and M.L. Heron, 1984b. Island wakes in shallow coastal waters. J. Geophys. Res., 89:10553-10569.
[41] Wolanski, E., King, B. and Galloway, D., 1995. Dynamics of the turbidity maximum in the Fly River estuary, Papua New Guinea. Estuarine, Coastal and Shelf Science 40, 321-337.
[42] Wolanski, E., Ridd, P. and Inoue, M., 1988. Currents through Torres Strait. Journal of Physical Oceanography 18, 1535-1545.

9 Appendices

9.1 Statement addressing the task objectives of the Torres Strait CRC

- **In association with other projects, identify focus issues to guide model development, and the selection of run scenarios and model outputs**

Current patterns are of considerable interest to Torres Strait indigenous communities who rely on natural resources for commercial and traditional purpose, as well as to industries such as fisheries and shipping that operate in the region. Understanding the large-scale circulation, sediment pathways and climate variability in Torres Strait region has been the focus issue to guide the model development.

An insight into habitat distribution has also been gained by providing physical surrogates, so as to ascertain the role of sediment transport and associated turbidity and their potential effects on Torres Strait ecosystem. In particular, high suspended sediment concentration has been identified as a key driver of seagrass meadows productivity, with significant implications for seagrass dieback.

- **Identify and collate relevant existing biophysical data**

The model has been driven by the best available atmospheric and oceanographic forcing fields and has been calibrated against a comprehensive set of oceanographic data, including wind, wave, salinity, temperature, current and sea levels.

Seasonal fluctuation of bottom light in Torres Strait has been derived from remote sensing observations (Margvelashvili and Saint-Cast, 2006). Photosynthetically active radiation was recorded on the field during the survey S266 (Heap et al. 2004), showing evidence of a bottom light reduction below seagrass resilience threshold (Margvelashvili and Saint-Cast, 2006).

- **Develop a three-dimensional circulation model for the region**

A 3D hydrodynamic model has been developed for the Torres Strait region. The model domain has encompassed parts the Coral Sea, Gulf of Papua, Arafura Sea and Gulf of Carpentaria.

A representation of the regional circulation has been derived from the analysis of calibrated model outputs, including surface currents, depth averaged currents and wave-current bottom friction velocity, and the regional connectivity with major sediment sources, such as the Fly River, has been investigated

- **Develop a sediment transport model including a parameterization of sandwaves**

A 3D sediment transport model has been nested to the previously described hydrodynamic model. Turbidity level, water sampling and bottom grab sediment data have been used in the sediment transport model calibration.

A sandwave model has been adapted from river flow models and shown to produce realistic sandwaves distribution in Torres Strait. The presence of sandwaves has also been

incorporated in the circulation model to optimize the correlation between measured and modelled currents.

- **Run a range of model scenarios capturing the major environmental variability in the Torres Strait system**

The circulation over the last eight years has been hindcast and patterns developing over temporal scales in the range of minutes to years have been captured. The influence of wave climate, neap-spring tidal cycle, seasonal winds and interannual climate variability has been described.

- **Run model scenarios directed at focus issues, such as seagrass dieback events**

Seasonal circulation patterns have been characterized and fine sediment pathways have been deduced and further confirmed by Margvelashvili and Saint-Cast (2006), allowing the identification of the seasonal mechanism responsible for Torres Strait high turbidity levels, which contribute to seagrass productivity reduction.

- **Provide information on processes and relevant model outputs to other tasks and projects**

The circulation model provided a transport framework for an embedded sediment transport model (Margvelashvili and Saint-Cast, 2006). Current fields will also be further used in the integrated ecosystem modelling for evaluating Torres Strait multiple-use management strategies (Pantus et al. 2006), in particular to determine the transport of suspended material such as chemical contaminants and fish larvae.

9.2 Calculating bottom currents

Near bottom velocities taken directly from the hydrodynamic model are at mid-height of the grid cell, rather than a standard height above the seabed. However, the latter is required to compute fields such as bottom stress. Two approaches were used to estimate bottom currents. In waters much deeper than the height of the bottom cell, the current velocity at distance z above the bed can be expressed as:

$$u(z) = \frac{\ln(z/z_0)}{\ln(z_r/z_0)} u(z_r);$$

where z_0 is the bed roughness height, z_r is the reference level of current velocity $u(z_r)$. In shallower water the bottom current estimate may be close to a surface current estimate. Bottom currents were therefore estimated from the depth-averaged currents by assuming a log-profile velocity distribution over the depth. The current velocity at distance z above the bed can then be expressed as:

$$u(z) = \frac{\ln(z/z_0)}{z_0/h - 1 + \ln(h/z_o)} u_{av};$$

where z_0 is the bed roughness height, h is the water depth and u_{av} is the depth integrated current speed.

9.3 Interannual surface current variability

Monthly mean surface current velocity anomaly covering the period 1997-2004 are provided on the data CD.

9.4 Interannual depth averaged current variability

Monthly depth averaged current velocity anomaly covering the period 1997-2004 are provided on the data CD.

9.5 Interannual bottom friction variability

Monthly mean wave-current bottom friction velocity anomaly covering the period 1997-2004 are provided on the data CD.

9.6 Interannual wind variability

The monsoon and trade winds in the Torres Strait region were characterised over the modelling period (1997-2005) by averaging the monthly mean surface wind velocity over the model domain (Figure 64). Monthly mean surface wind friction velocity anomaly covering the period 1997-2004 are provided on the data CD. Interannual variability in the strength and length of the trade wind season was relatively low, while the monsoon exhibited significant variability. The strongest monsoons were in 1997, 1998, 1999, 2002 and 2004, whereas in 1999-2000 the monsoon was hardly present. Interannual variability in the surface wind speed was generally less than 10% of the mean throughout the years 1997-2005. However, the largest anomalies were found over the transition between seasons. i.e. March and December. In particular, the monsoon lasted longer in 1997 and 2004 with westerly winds blowing until March. The trade season started early in 1999 and 2000 with easterly winds blowing over March. The trade season was shorter in 2001, with westerly winds arriving in December.

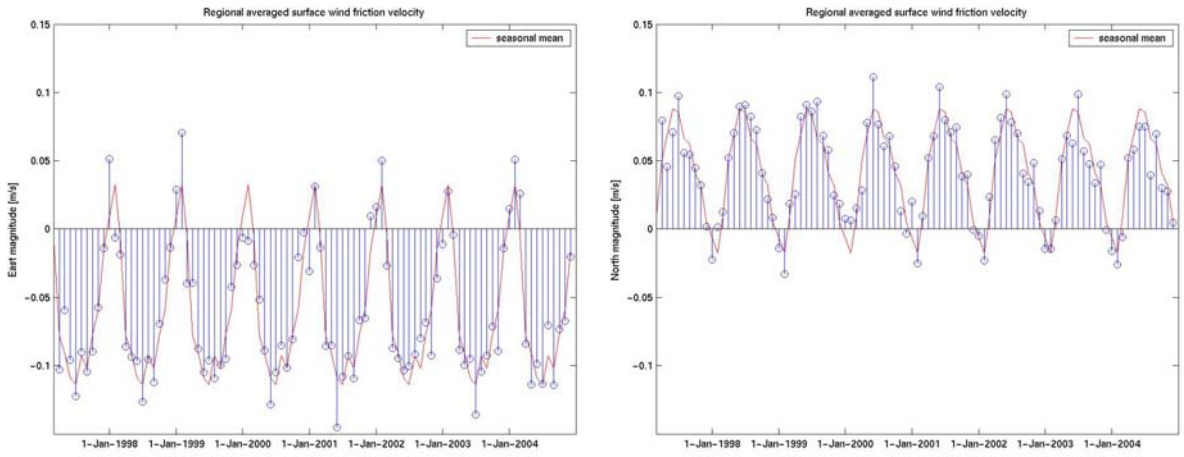

Figure 64: Regional averaged of monthly surface wind friction velocity.

9.7 Interannual wave variability

Monthly mean significant wave height anomaly covering the period 1997-2004 are provided on the data CD. Interannual variability in the Torres Strait regional wave fields followed the winds, with low variability between the trade seasons and much higher variability between monsoons. There was also a higher degree of variability in the Gulf of Carpentaria than in

the Coral Sea. The most significant wave anomalies (> 0.6 m) in the Gulf of Carpentaria occurred in March 1997, January 1998, April 1999, November 2000, and February 2002. The most significant wave anomalies (> 0.6 m) in the Coral Sea occurred in February 1998, February 2000, May 1999, and July 2002.

9.8 Seasonal sea level variability

Strong seasonal wind set-up and set down occurred to the west of Torres Strait in the Gulf of Carpentaria, while those to the east were smaller. The monthly mean sea level variation was around 0.5 m in the Gulf of Carpentaria, 0.15 m in the northern Great Barrier Reef, and much smaller offshore in the Coral Sea (Figure 65 and Figure 66). Sealevel on either side of Torres Strait did not vary in phase, often resulting in a large hydraulic gradient through the strait which controlled the through-flow.

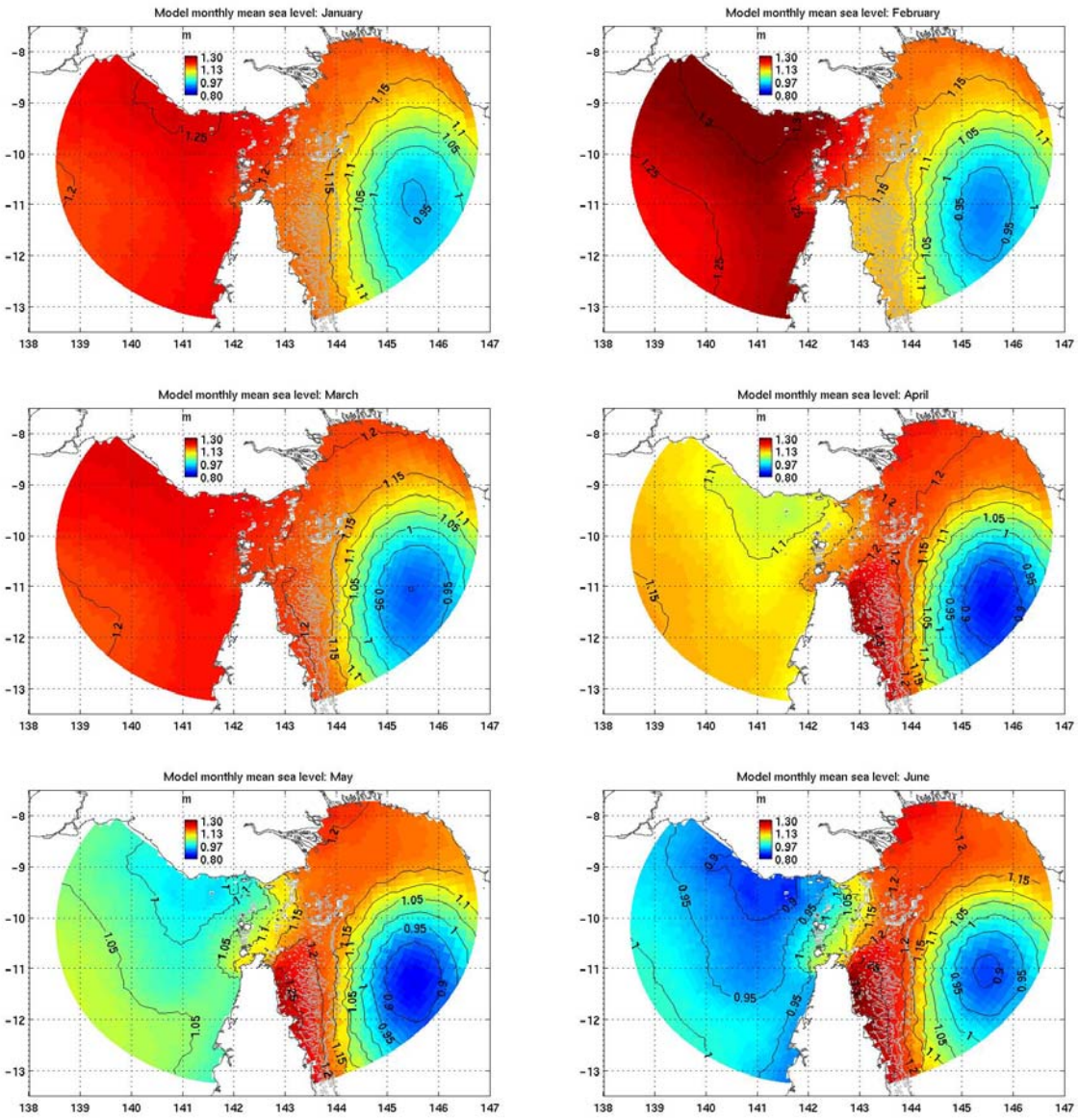

Figure 65: Monthly mean sealevel covering the period 1997-2004 (January to June). The global model (OFAM) indicates that the amplitude of mean sea level seasonal oscillation to the west of Torres Strait is around 0.5m, while it is much lower in to the east. This significant offset between the sea levels on each side of the strait generates a hydraulic gradient, which is responsible for driving the seasonal flow through Torres Strait. The greater the gradient the stronger the flow, i.e. a sustained westward flow occurs from May to October during the Trades, while a short window over February favours a eastward flow.

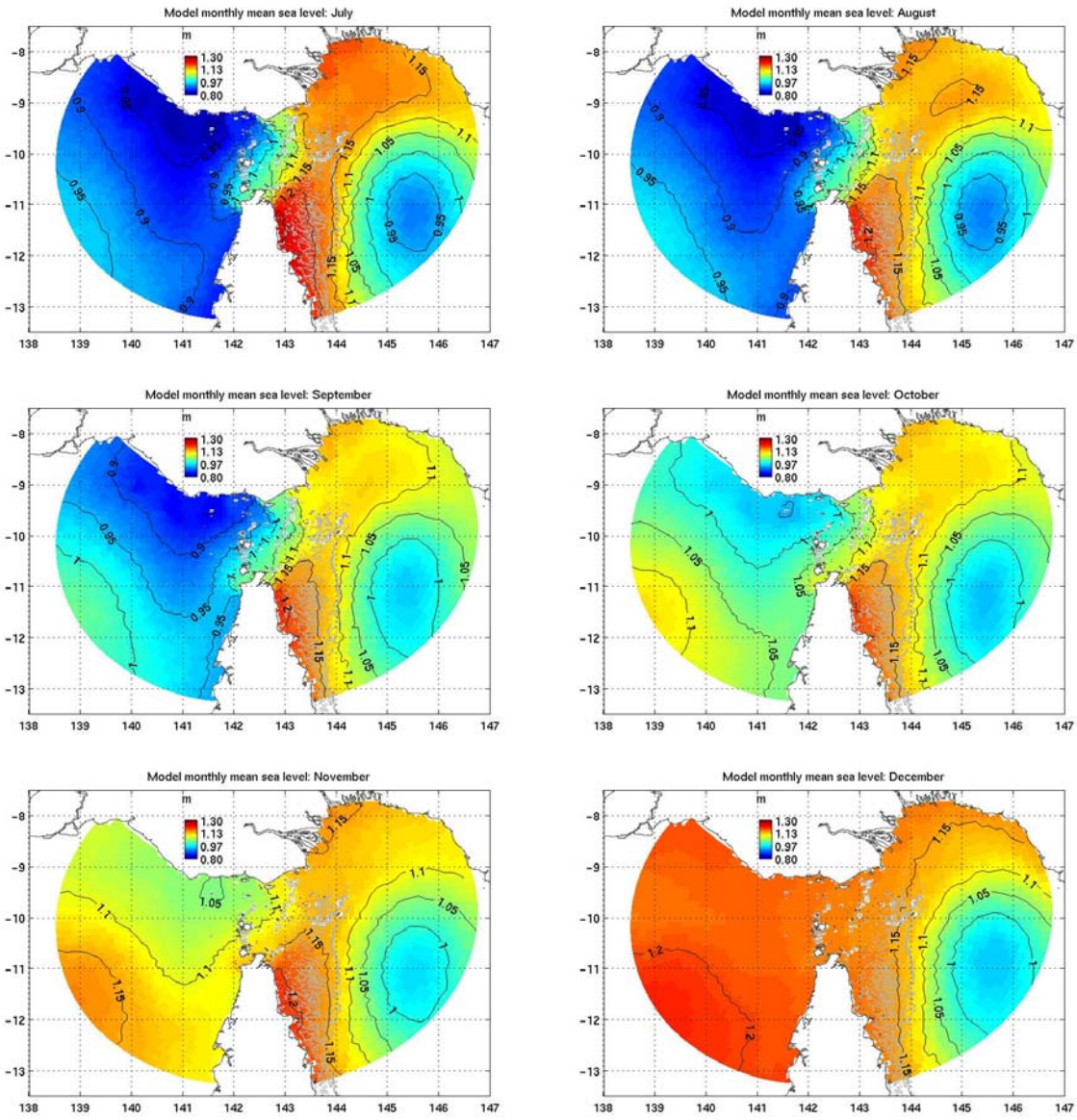

Figure 66: Monthly mean sealevel covering the period 1997-2004 (July to December). The global model (OFAM) indicates that the amplitude of mean sea level seasonal oscillation to the west of Torres Strait is around 0.5m, while it is much lower in to the east. This significant offset between the sea levels on each side of the strait generates a hydraulic gradient, which is responsible for driving the seasonal flow through Torres Strait. The greater the gradient the stronger the flow, i.e. a sustained westward flow occurs from May to October during the Trades, while a short window over February favours a eastward flow.